



High Temperature Thermoelectric Properties of ZnO Based Materials

Han, Li

Publication date:
2014

Document Version
Publisher's PDF, also known as Version of record

[Link back to DTU Orbit](#)

Citation (APA):
Han, L. (2014). *High Temperature Thermoelectric Properties of ZnO Based Materials*. Department of Energy Conversion and Storage, Technical University of Denmark.

General rights

Copyright and moral rights for the publications made accessible in the public portal are retained by the authors and/or other copyright owners and it is a condition of accessing publications that users recognise and abide by the legal requirements associated with these rights.

- Users may download and print one copy of any publication from the public portal for the purpose of private study or research.
- You may not further distribute the material or use it for any profit-making activity or commercial gain
- You may freely distribute the URL identifying the publication in the public portal

If you believe that this document breaches copyright please contact us providing details, and we will remove access to the work immediately and investigate your claim.

High Temperature Thermoelectric Properties of ZnO Based Materials

PhD Thesis

by

Li Han

Principle Supervisor: Prof. Søren Linderøth

Co-supervisors: Prof. Nini Pryds

Dr. Ngo Van Nong

Department of Energy Conversion and Storage

Technical University of Denmark

Roskilde, Denmark

June 2014

Abstract

This thesis investigated the high temperature thermoelectric properties of ZnO based materials. The investigation first focused on the doping mechanisms of Al-doped ZnO, and then the influence of spark plasma sintering conditions on the thermoelectric properties of Al, Ga-dually doped ZnO. Following that, the nanostructuring effect for Al-doped ZnO was systematically investigated using samples with different microstructure morphologies. At last, the newly developed ZnCdO materials with superior thermoelectric properties and thermal stability were introduced as promising substitutions for conventional ZnO materials.

For Al-doped ZnO, α - and γ -Al₂O₃ were selectively used as dopants in order to understand the doping mechanism of each phase and their effects on the thermoelectric properties. The samples were prepared by the spark plasma sintering technique from precursors calcined at various temperatures. Clear correlations between the initial crystallographic phase of the dopants and the thermoelectric properties of the resulting Al-doped ZnO were observed.

For Al, Ga-dually doped ZnO, the spark plasma sintering conditions together with the microstructural evolution and thermoelectric properties of the samples were investigated in detail. A proposed solid-state-reaction model suggested that a sintering temperature above 1223K would be preferable in order to achieve phase equilibrium in the samples. The sintering mechanism of the ZnO particles and microstructural evolutions at different sintering temperatures were investigated by the simulation of the self-Joule-heating effect of the individual particles.

The effects of nanostructuring in Al-doped ZnO were systematically investigated using samples with different microstructural morphologies. The samples with preferentially oriented grains exhibited anisotropic thermoelectric properties. The measured zT values along the preferred orientation directions were found to be higher than those along the other direction. The sample consolidated from nanoparticles exhibited fine grains and widely distributed nanoprecipitates, resulting in a zT value of 0.3 at 1223 K due to the lower thermal conductivity resulting from nanostructuring. Using the simple parabolic band model and the Debye-Callaway thermal transport model, the anisotropic properties of the nanostructured samples were elucidated and the influence of the grain size and nanoprecipitates on the electron and phonon transport was analyzed and discussed in detail.

In order to solve the problems of high thermal conductivity without the deterioration of electrical conductivity by nanostructuring for conventional ZnO materials, the doped ZnCdO material was proposed as a new n-type oxide thermoelectric material. The material is sintered in air in order to maintain the oxygen stoichiometry and avoid the stability issues. The successful alloying of CdO with ZnO at a molar ratio of 1:9 resulted in a significant reduction of thermal conductivity up to 7-fold at room temperature. By careful selection of the dopants and dopant concentrations, a large power factor was obtainable. The sample with the composition of Zn_{0.9}Cd_{0.1}Sc_{0.01}O obtained the highest zT ~0.3 @1173 K, ~0.24 @1073K, and a good average zT which is better than the state-of-the-art n-type thermoelectric oxide materials. Meanwhile, Sc-

doped ZnCdO is robust in air at high temperatures, while other n-type materials such as Al, Ga-doped ZnO will experience rapid degradation on thermoelectric performances. The thermoelectric properties of a series of samples with varied concentrations of Cd, Sc, and some other dopants are investigated and discussed in detail.

Referat

(Abstract in Danish)

Denne afhandling undersøger termoelektriske egenskaber af ZnO-baserede materialer ved høje temperaturer. Undersøgelsen er først fokuseret på doteringsmekanismen af Al-doteret ZnO og indflydelsen af betingelserne for *spark plasma sintering* på de termoelektriske egenskaber af ZnO doteret med både Al og Ga. Efterfølgende bliver effekten af at nanostrukturere Al-doteret ZnO systematisk undersøgt ved at udnytte prøver med forskellige mikroskopiske morfologier. Til sidst bliver det nyudviklede ZnCdO materiale med fremragende termoelektriske egenskaber og termisk stabilitet introduceret som en lovende substitut til konventionelle ZnO materialer. α - og γ -Al₂O₃ blev udvalgt som doteringsmateriale for Al-doteret ZnO for at forstå doping effekten og dens mekanisme. Prøverne er forberedt med teknikken spark plasma sintering fra precursorer calcineret ved forskellige temperaturer. En klar korrelation mellem doteringen og de termoelektriske egenskaber blev observeret.

For ZnO doteret med både Al og Ga er betingelserne for *spark plasma sintering* undersøgt sammen med mikrostrukturen og de termoelektriske egenskaber af prøverne. En model af faststofsreaktionen tyder på, at sintering ved temperaturer over 1223K vil være at foretrække mht. faselegvægt i prøverne. Sinteringsmekanismen for ZnO-partikler og udviklingen af mikrostrukturen ved forskellige sintering-temperaturer blev undersøgt ved at simulere effekten af selv-Joule-opvarmning af de individuelle partikler.

Effekten af nanostrukturering for Al-doteret ZnO var systematisk undersøgt med prøver med forskellige mikroskopiske morfologier. Prøver, hvor korn havde en fortrukket orientering, udviste anisotropi i de termoelektriske egenskaber. De målte zT -værdier langs den foretrukne retning for kornene viste sig at være højere end de andre retninger. Prøven, som var opbygget fra nanopartikler, udviste fine korn og fordelte nanobundfældninger, som resulterede i en zT -værdi på 0.3 ved 1223 K. Denne værdi er forårsaget af den lave termiske ledningsevne, som resulterede fra nanostrukturen. Brugen af den simple, paraboliske båndmodel og Debye-Callaway termiske transportmodel kastede lys over de anisotropiske egenskaber af de nanostrukturerede prøver. Desuden kunne effekten af kornstørrelsen og nanobundfældningerne på elektron- og fonon-transporten blive analyseret og diskuteret i detalje.

For at løse problemet ved nanostrukturering af konventionelle ZnO-materialer, hvor en høj termisk ledningsevne typisk også nedsænker den elektriske ledningsevne, blev det doterede ZnCdO-materiale forslået som en ny n-type termoelektrisk oxidmateriale. Materialet er sintret i luft for at bibeholde oxygen-stoichiometrien og undgå problemer med stabiliteten. Den succesfulde legering af CdO med ZnO med et molært forhold på 1:9 resulterede i en betydelig reduktion af den termiske ledningsevne med en faktor 7 ved stuetemperatur. Ved nøje udvælgelse af doterings-materiale og -koncentrationer kunne en høj *power factor* opnås. Prøven med kompositionen Zn_{0.9}Cd_{0.1}Sc_{0.01}O opnåede den højeste $zT \sim 0.3$ ved 1173 K & ~ 0.24 ved 1073K, samt en god gennemsnitlig zT , som er bedre end de hidtil bedste n-type termoelektriske

oxid-materialer. Sc-doteret ZnCdO er desuden stabil i luft ved høje temperature hvorimod de termoelektriske egenskaber for andre n-type materialer så som Al, Ga-doteret ZnO hurtigt vil degradere. De termoelektriske egenskaber af en række prøver med varierende koncentrationer af Cd, Sc og andre doteringsmaterialer er undersøgt og diskuteret i detalje.

Contents

| | |
|--|-------------|
| Abstract | II |
| Referat | IV |
| Contents | VI |
| Acknowledgements | IX |
| List of Publications | XI |
| List of Figures | XIII |
| List of Tables | XIII |
| Chapter 1 Introduction | 1 |
| 1.1 Fundamentals for Thermoelectrics | 1 |
| 1.11 Seebeck effect | 1 |
| 1.12 Figure of Merit, zT | 4 |
| 1.13 Nanostructuring for thermoelectrics..... | 7 |
| 1.2 Oxide Thermoelectrics and ZnO based Thermoelectric Materials..... | 9 |
| 1.2.1 Background for oxide thermoelectrics | 9 |
| 1.2.2 Background for ZnO based thermoelectrics | 10 |
| 1.2.3 Nanostructuring of ZnO thermoelectrics and the issues..... | 12 |
| 1.2.4 Unstable thermoelectric properties of ZnO | 13 |
| 1.3 Thesis Outline..... | 16 |
| Chapter 2 Experimental | 18 |
| 2.1 Material Processing..... | 18 |
| 2.11 Power processing | 18 |
| 2.12 Ceramic Sintering..... | 19 |
| 2.2 Material Characterization..... | 20 |
| 2.21 Structural characterization | 20 |
| 2.22 Electrical transport properties characterization | 21 |
| 2.23 Thermal properties characterization..... | 22 |
| 2.3 Issues for ZnO thermoelectric properties measurement | 22 |
| Chapter 3 The Influence of α- and γ-Al₂O₃ Phases on the Thermoelectric Properties of Al-doped ZnO | 26 |

| | |
|---|-----------|
| 3.1 Introduction | 27 |
| 3.2 Experimental Procedure | 27 |
| 3.3 Results and Discussion | 28 |
| 3.3.1 Structural properties | 28 |
| 3.3.2 Thermoelectric properties | 29 |
| 3.3.3 Theoretical analysis and discussions | 34 |
| 3.3.4 Doping mechanisms of Al ₂ O ₃ into ZnO | 35 |
| 3.4 Conclusions | 37 |
| Chapter 4 The Influence of Spark Plasma Sintering Temperature on the Microstructure and the Thermoelectric Properties of Al, Ga dually-doped ZnO | 38 |
| 4.1 Introduction | 39 |
| 4.2 Experimental Procedure | 39 |
| 4.3 Results and Discussion | 40 |
| 4.3.1 Structural properties | 40 |
| 4.3.2 Thermoelectric properties | 42 |
| 4.3.3 Theoretical Analysis and Discussion | 44 |
| 4.4 Conclusion..... | 49 |
| Chapter 5 Effects of morphology on the thermoelectric properties of Al-doped ZnO | 50 |
| 5.1 Introduction | 51 |
| 5.2 Experimental Procedure | 52 |
| 5.2.1 Preparation of samples | 52 |
| 5.2.2 Measurements | 53 |
| 5.3 Results and discussions | 54 |
| 5.3.1 Structural properties | 54 |
| 5.3.2 Thermoelectric properties | 58 |
| 5.3.3 Theoretical Analysis and Discussion | 63 |
| 5.4 Conclusions | 65 |
| Chapter 6 Doped ZnCdO as stable n-type material for thermoelectric application | 66 |
| 6.1 Introduction | 67 |
| 6.2 Experimental Procedure | 68 |
| 6.2.1 Preparation of samples | 68 |

| | |
|---|-----------|
| 6.2.2 Measurements | 68 |
| 6.3 Results and discussions | 68 |
| 6.3.1 Structural properties | 68 |
| 6.3.2 Thermoelectric properties | 73 |
| 6.3.3 Thermoelectric stability in air | 87 |
| 6.4 Conclusions | 89 |
| Chapter 7 Conclusions and Outlooks | 90 |
| 7.1 The doping mechanisms and thermoelectric properties of Al-doped ZnO | 90 |
| 7.2 SPS densification mechanisms and thermoelectric properties of Al, Ga-dually doped ZnO | 90 |
| 7.3 Achieving Low Thermal Conductivity by Nanostructuring for Al-doped ZnO | 91 |
| 7.4 Doped ZnCdO material as a promising substitution for conventional ZnO materials. | 91 |
| 7.5 Outlook of the future work..... | 92 |
| Appendix A..... | 93 |
| Appendix B..... | 94 |
| References | 98 |

Acknowledgements

Three years have passed so quickly, like the bracing wind swept over the beautiful Roskilde Fjord. I still remember the first day I came to Risø, I could hardly believe such a beautiful place was where I would stay for my PhD study. So I embraced it as cherishing my destiny. The longer I stay here, the more I like this place, as well as the people around me. Three years of studying not only enriched my knowledge to material science, but also taught me a rational way of thinking and systematical way of working. I couldn't be more grateful for the top-levelled education received here. I always feel that I am lucky.

My first and foremost gratitude goes to my supervisors: Dr. Ngo Van Nong, Prof. Nini Pryds, and Prof. Søren Linderøth. Dr. Ngo Van Nong is a strong minded and intelligent material scientist, who mentored me from the basic lab skills and article writing with patience. I am deeply grateful for his considerations about me and the generous help he provided. Prof. Nini Pryds is a truly admired material scientist and physicist. He is certainly an inspiration to me for his hard working, responsible, and rational attitude. Nevertheless, he is also kind and full of wisdom. He taught me how to stand for my own results and dare to speak with a determined heart and confidence. I am deeply thankful to his guidance and supports. Prof. Søren Linderøth has the most charming personality I ever seen. He is a department leader with busy schedules, but he is willing to spend hours with his students for scientific discussions and paper revisions. He taught me how to plan and establish work systematically and to think rationally as a real scientist. I feel grateful and honored to be his student. I also want to thank our international collaborator Prof. Michitaka Ohtaki, who is truly an excellent chemist and material scientist. He offered me a perfect external stay in Kyushu University, and we had lots of fruitful experiments and discussions together.

I want to express my thanks to our group members, both past and present, Tim Holgate, Thanh Hung Le, NingYu Wu, and Hoang Ngan Pham. We spent a lot of time together, both for work and for fun. They never hesitated to offer me help as I needed it, like true friends did. Three years are short, but they made it wonderful and memorable. I am also thankful to the people outside our group but also offered me great help. Dennis Valbjørn Christensen, he helped me a lot with the hall measurement and the translation of the thesis abstract. Dr. Wei Zhang, an expert on electron microscopy, he helped me with TEM characterizations as well as perform the post-analysis. Dr. Yunzhong Chen, a talented physicist, he helped me with the hall measurement. The legendary Dr. Finn Wiley, an expert on XRD and defect chemistry, he taught me how to properly conduct XRD characterizations and inspired me with his work on defect chemistry. Dr. Nikolaos Bonanos, a truly admired expert on electrochemistry, he taught me impedance spectroscopy, and I was very much benefited from our discussions on oxide materials. Dr. Yue Zhao, an experienced chemist, he taught me how to conduct spin coating.

I would also like to thank my PhD thesis assessment committee members: Prof. Anke Weidenkaff, Prof. Anders Plamqvist, and Dr. Andeas Kaiser for reading and assessing my thesis. Thanks to our secretary Anita Voss and Heidi Pedersen for helping me with the paper works

before graduation, and I also want to thank Lene Thorsted, together with Anita Voss and Heidi Pedersen for helping me with my academic affairs during the three years. Thanks to our lab technicians and engineers, Pernille Hedemark Nielsen, Annelise Mikkelsen, Jørgen Geyti, Steen Bang, Agnes Kjølner, Linda Bohn, Carsten Gynther Sørensen, John Johnson and Sidsel Bjerre Andersen for their numerous help on practical laboratory work and safety issues.

I am also thankful to all the people both inside and outside of our department who offered me generous help. In particular, I am grateful to Espen Drath Bøjesen, Martin Søndergaard, Mouritz Svenson, Regina Bulatova, Andrea Carlo Cazzaniga, WeiWei Zhang, Angela Zhang, Dewei Ni, Jin Shao, and Youkun Tao, for their kind help on various aspects of my study, research, and living here.

My deepest gratitude goes to my family and my wife. My beautiful wife, Dan Song, she gave up her job, left behind her parents, and followed me to Denmark. She supported me with her love and caring. Without her, I couldn't have gone so far. My parents and brother in China, they never stopped caring about me and encouraging me to fly even further. I love them and miss them every day.

Last but not least, I want to thank our department, DTU Energy Conversion, for generously supporting my education here. And thanks to the Programme Commission on Energy and Environment (EnMi) which is part of the Danish Council for Strategic Research (Contract No. 10-093971), for financially supporting my research work which is part of the OTE-POWER project.

List of Publications

(During PhD study only)

Peer-reviewed Papers:

- [1] Li Han, Ngo Van Nong, Wei Zhang, Thanh Hung Le, Tim Holgate, Kazunari Tashiro, Michitaka Ohtaki, Nini Pryds, and Søren Linderøth, “*Effects of morphology on the thermoelectric properties of Al-doped ZnO*,” RSC Adv. **4**, 12353 (2014).
- [2] Li Han, Ngo Van Nong, Thanh Hung Le, Tim Holgate, Nini Pryds, Michitaka Ohtaki, and Søren Linderøth, “*The Influence of α - and γ -Al₂O₃ Phases on the Thermoelectric Properties of Al-doped ZnO*,” J. Alloys Compd. **555**, 291 (2013).
- [3] Li Han, Thanh Hung Le, Ngo Van Nong, Nini Pryds, and Søren Linderøth, “*The Influence of Spark Plasma Sintering Temperature on the Microstructure and Thermoelectric Properties of Al,Ga Dual-Doped ZnO*,” J. Electron. Mater. **42**, 1573 (2013).
- [4] Tim Holgate, Li Han, NingYu Wu, Espen Drath Bøjesen, Mogens Christensen, Bo B. Iversen, Ngo Van Nong, Nini Pryds, “*Characterization of the interface between an Fe–Cr alloy and the p-type thermoelectric oxide Ca₃Co₄O₉*,” J. Alloys Compd. **582**, 827 (2014).
- [5] Tim Holgate, Li Han, NingYu Wu, Ngo Van Nong, Nini Pryds, “*Effects of conducting oxide barrier layers on the stability of Crofer®22 APU/ Ca₃Co₄O₉ interfaces*,” J. Mater. Res., submitted, (2014).
- [6] Le Thanh Hung, Ngo Van Nong, Li Han, Rasmus Bjørk, Pham Hoang Ngan, Tim C. Holgate, Søren Linderøth, and Nini Pryds, “*Segmented thermoelectric oxide-based module*,” Appl. Energ., submitted, (2014).
- [7] Thanh Hung Le, Ngo Van Nong, Li Han, Dang Le Minh, Kasper A Borup, Bo B. Iversen, Nini Pryds, Søren Linderøth, “*High-temperature Thermoelectric Properties of Ca_{0.9}Y_{0.1}Mn_{1-x}Fe_xO₃ (0 ≤ x ≤ 0.25)*,” J. Mater. Sci. **48**, 2817 (2013).
- [8] Abdullah Khan, Mohsin Saleemi, Mats Johnsson, Li Han, Ngo V. Nong, Mamoun Muhammed, and Muhammet Toprak, “*Fabrication, spark plasma consolidation, and thermoelectric evaluation of nanostructured CoSb₃*,” J. Alloys Compd., under review, (2014).

Manuscript in preparation:

- [1] Li Han, Ngo Van Nong, Thanh Hung Le, Yunzhong Chen, Tim Holgate, Nini Pryds, Søren Linderøth, “*Scandium-doped zinc cadmium oxide as a stable n-type material for thermoelectric application*,” Manuscript in preparation, (2014).
- [2] Li Han, Dennis V. Christensen, Andrea C. Cazzaniga, Nini Pryds, Thanh Hung Le, Ngo Van Nong, Søren Linderøth, “*Gallium doped zinc cadmium oxide as a transparent conductive oxide for optoelectronic devices*,” Manuscript in preparation, (2014).

Conference Presentations

- [1] Li Han, Ngo Van Nong, Wei Zhang, Thanh Hung Le, Tim Holgate, Kazunari Tashiro, Michitaka Ohtaki, Nini Pryds, and Søren Linderorth, “*Effects of morphology on the thermoelectric properties of Al-doped ZnO*,”
Part of: Proceedings of the MRS 2013 Fall Meeting, 2013,
Presented at: Materials Research Society 2013 Fall, Boston (Oral)
- [2] Li Han, Ngo Van Nong, Wei Zhang, Thanh Hung Le, Tim Holgate, Kazunari Tashiro, Michitaka Ohtaki, Nini Pryds, and Søren Linderorth, “*Thermoelectric Properties of Nano-structured Al-doped ZnO by using Precursors with Different Morphologies*,”
Part of: Proceedings of the 32nd International Conference on Thermoelectrics, 2013,
Presented at: 32nd International Conference on Thermoelectrics, 2013, Kobe (Poster)
- [3] Li Han, Ngo Van Nong, Thanh Hung Le, Tim Holgate, Nini Pryds, Michitaka Ohtaki, and Søren Linderorth, “*The Influence of α - and γ -Al₂O₃ Phases on the Thermoelectric Properties of Al-doped ZnO*,”
Part of: Proceedings of the E-MRS 2012 Spring Meeting, 2012,
Presented at: European Materials Research Society 2012, Strasbourg (Oral)
- [4] Li Han, Thanh Hung Le, Ngo Van Nong, Nini Pryds, and Søren Linderorth, “*The Influence of Spark Plasma Sintering Temperature on the Microstructure and Thermoelectric Properties of Al,Ga Dual-Doped ZnO*,”
Part of: Proceedings of the 31st International and 10th European Conference on Thermoelectrics, 2012,
Presented at: 31st International & 10th European Conference on Thermoelectrics, Aalborg (Oral)

Submitted Patents

- [1] Li Han, Ngo Van Nong, Nini Pryds, and Søren Linderorth: Scandium-doped Zinc Cadmium Oxide as a Stable n-type Material for Thermoelectric Application. 2014.
- [2] Nini Pryds, Li Han, Dennis V. Christensen, and Søren Linderorth: Gallium doped Zinc Cadmium Oxide as a Transparent Conductive Oxide for Optoelectronic Devices. 2014.

List of Figures

| | Page |
|---|------|
| Fig. 1.1 Schematics illustrations of Seebeck effect, (a) when a temperature gradient is given to n-type and p-type materials, the charge carriers gain an electromotive force towards the cold side; (b) an internal electrical field is built and equilibrium is reached, an electrical voltage difference is obtained across the material as long as the temperature gradient exists. | 2 |
| Fig. 1.2 A schematic illustration of a thermoelectric generator module. | 4 |
| Fig. 1.3 Calculated plot of maximum energy conversion efficiency as a function of the figure of merit ZT . Calculations were made according to Eq. 1.8 with $T_{\text{cold}} = 300$ K. | 5 |
| Fig. 1.4 The trade-off relationship among Seebeck coefficient S , electrical conductivity σ , and thermal conductivity κ . Optimizing zT involves a compromise of these values. Figure taken from Snyder and Toberer's work[5]. | 6 |
| Fig. 1.5 The improvement of zT by reducing the lattice thermal conductivity κ_L . The carrier concentration n will be re-optimized as κ_L reduces. Figure taken from Snyder and Toberer's work[5]. | 7 |
| Fig. 1.6. Illustrations of electronic density of states (DOS) for low-dimensional semiconductors. Figure taken from Dresselhaus's work[16]. | 8 |
| Fig. 1.7 Effects of interfacial scatterings on the reduction of thermal conductivity by adding Si nanoparticles and nanowires into SiGe host material. Figure taken from Dresselhaus's work[16]. | 8 |
| Fig. 1.8 Literature values of zT for state the art thermoelectric materials. The dashed lines are the maximum zT values for bulk materials, and the solid lines are from nanostructured materials. (BiSbTe, and nano BiSbTe, Ref. [22]; n-SiGe, nano n-SiGe, Ref. [23]; p-SiGe, nano p-SiGe, Ref.[24] ; PbNaTe, and PbNaTe/SrTe, Ref.[9]; PbTe, and $\text{Na}_{0.95}\text{Pb}_{20}\text{SbTe}_{22}$, Ref.[25]). | 9 |
| Fig. 1.9 Re-plotting zT of oxide thermoelectric materials from literatures[11,30,32,34–36]. | 10 |
| Fig. 1.10 (a) A schematic of wurtzite ZnO crystal structure. (b) A powder diffraction pattern for ZnO. | 11 |
| Fig. 1.11 (a) Carrier mobility of a ZnO single crystal as function of temperature. Figure is taken from Lin's work [48]. (b) DOS effective mass m^* for ZnO as a function of carrier concentration n . m_e is the free electron mass. Figure is taken | 11 |

from Kim's work [49].

Fig. 1.12 Re-plotting zT of ZnO based thermoelectric materials from literatures[35, 51–56]. 12

Fig. 1.13 The comparison of Figure of Merit zT between ZnO nanocomposites and bulk samples without nanostucturing. Data extracted from literatures by Ohtaki et al[35], Jood et al[10], and Nam et al[53]. 13

Fig. 1.14 Electrical resistivity and Seebeck coefficient of the ZnO:Al thin films as a function of temperature (first cycle in air and second cycle in Ar/H₂). Figure taken from the work of Schäuble et al [59]. The red star '1' represents the as deposited oxygen deficient status; and the blue star '2' represents the air annealed oxygen rich status. 14

Fig. 1.15 Ball and stick model of the (a) +1 charge state oxygen vacancy, (b) +2 charge state oxygen vacancy, (c) zinc interstitial, (d) zinc antisite. Figure taken from Janotti and Van de walle's work [60]. 15

Fig. 2.1 Stainless steel hydrothermal reactor and the Teflon liner. 19

Fig.2.2 The real picture of a SPS units of Dr Sinter 515S (Syntex Inc., Japan) during sintering. 20

Fig.2.3 (a) the real picture of a sample measured in ULVAC-RIKO ZEM-3; (b) an illustrative scheme of the wire configuration with the sample for ULVAC-RIKO ZEM-3. 21

Fig.2.4 (a) the real picture of a sample measured in RZ-2001i (Figure taken from <http://www.empa.ch>); (b) an illustrative scheme of the wire configuration with the sample for RZ-2001i. 21

Fig. 2.5 An illustration of a pellet sample losing its homogeneity due to post-annealing under different atmospheres. (a) The real picture of a cut specimen; (b) An schematic of the specimen for (a); (c) An schematic of a reverse case, sample first sintered in air and then post annealed without oxygen partial pressure. 23

Fig.2.6. Three cases for the measurements in air using RZ-2001i (OZAWA, Japan) system: (a) measurement of an oxygen sufficient sample, the results are reliable; (b) measurement of an oxygen deficient sample at high temperature, the surface restores oxygen, the power factor is overestimated; (c) measurement of an inhomogeneous sample, the power factor is seriously overestimated. 24

Fig.2.7. Three cases for the measurements in vacuum using ULVAC-RIKO ZEM-3 system: (a) measurement of an oxygen deficient sample, the results are reliable; (b) measurement of an oxygen sufficient sample at high temperature, the surface loses oxygen, but the power factor is close to the oxygen sufficient value; (c) measurement of an inhomogeneous sample, the power factor is close to the 24

oxygen deficient value.

Fig.2.8. Illustrations for the measurements of inhomogeneous samples; (a) measurement of S using a two-probe method; (b) measurement of σ using a four-probe method, the σ is close to the oxygen deficient value. Using the as-measured σ will result in an overestimation of power factor; (c) measurement of σ using a four-probe method, the σ is close to the oxygen sufficient value. Using the as-measured σ will result in an underestimation of power factor. 25

Fig. 3.1 (a) XRD patterns of α/γ - Al_2O_3 -doped ZnO with different calcination temperatures (from 973 to 1273 K). The dotted box magnified as the inset shows the position of the strongest peak from ZnAl_2O_4 . (b) The unit cell volume obtained from the lattice parameter refinement as a function of the calcination temperature. 28

Fig. 3.2 SEM photographs of the fracture surfaces of α/γ - Al_2O_3 -doped ZnO. (a) γ -973, (b) γ -1073, (c) α -1073, (d) α -1273, (e) a representative high-magnification SEM image of the ZnAl_2O_4 nanoprecipitates. EDX line scans of Zn, O, and Al $K\alpha_1$ X-ray peaks obtained along the yellow arrow are shown in (f). 29

Fig. 3.3 Temperature dependence of the electrical conductivity of α/γ - Al_2O_3 -doped ZnO samples. The inset shows the electrical conductivity at 1173 K as a function of the calcination temperature. 30

Fig. 3.4 Temperature dependence of the Seebeck coefficient of α/γ - Al_2O_3 -doped ZnO samples. The inset shows the Seebeck coefficient at 1173 K as a function of the calcination temperature. 31

Fig. 3.5 Temperature dependence of the thermal conductivity of α/γ - Al_2O_3 -doped ZnO samples. The inset shows the thermal conductivity at 1173 K as a function of the calcination temperature. 32

Fig. 3.6 Temperature dependence of the power factor of α/γ - Al_2O_3 -doped ZnO samples. The inset shows the power factor at 1173 K as a function of the calcination temperature. 33

Fig. 3.7 Temperature dependence of zT of α/γ - Al_2O_3 -doped ZnO samples. The inset shows the zT values at 1173 K as a function of the calcination temperature. 33

Fig. 3.8 (a) The calculated reaction time course as a weight fraction of reacted Al_2O_3 for the ZnAl_2O_4 formation. (b) The percentage of reaction completed after 1 hour as a function of the calcination temperature. 34

Fig. 3.9 A modified schematic diagram for the solid-state reaction process of ZnO and Al_2O_3 based on Branson's investigation. 36

Fig. 4.1 (a) XRD patterns of $\text{Zn}_{0.96}\text{Al}_{0.02}\text{Ga}_{0.02}\text{O}$ with different sintering temperatures (from 1073 to 1273 K). The left and right dotted box magnified as 40

the inset shows the position of the strongest peaks from ZnGa_2O_4 and ZnAl_2O_4 , respectively. (b) The lattice parameters and unit cell volume of $\text{Zn}_{0.96}\text{Al}_{0.02}\text{Ga}_{0.02}\text{O}$ samples with different sintering temperatures.

Fig. 4.2. SEM photographs of the fracture surfaces of $\text{Zn}_{0.96}\text{Al}_{0.02}\text{Ga}_{0.02}\text{O}$ with different sintering temperatures of (a) 1073K, (b) 1173K, (c) 1223K, and (d) 1273K . 41

Fig. 4.3 Temperature dependence of (a) the electrical conductivity, and (b) the Seebeck coefficient of $\text{Zn}_{0.96}\text{Al}_{0.02}\text{Ga}_{0.02}\text{O}$ samples with different sintering temperatures. 42

Fig. 4.4 Temperature dependence of (a) the power factor, and (b) the thermal conductivity of $\text{Zn}_{0.96}\text{Al}_{0.02}\text{Ga}_{0.02}\text{O}$ samples with different sintering temperatures. 43

Fig. 4.5 Temperature dependence of zT of $\text{Zn}_{0.96}\text{Al}_{0.02}\text{Ga}_{0.02}\text{O}$ samples with different sintering temperatures. 44

Fig.4.6 (a) The calculated reaction time course as a weight fraction of Al_2O_3 reacted with ZnO . (b) The calculated weight fraction of Al_2O_3 reacted with ZnO as a function of sintering temperature. 45

Fig. 4.7 A schematic of the sintering setups and the assumed ZnO sphere stacks. 46

Fig. 4.8 (a, b, c) the calculated distributions of temperature-increase (ΔT) in ZnO particle (a) at the early stage of sintering, (b) half-sintered, and (c) fully sintered, T_0 is the background temperature, I_T is the total current intensity, and D_p is the displacement percentage of the sample. (d), (e), and (f) are the corresponding plotted diagrams of (a), (b), and (c). 47

Fig. 4.9 (a) the fracture surface of the sample sintered at 1073 K with the arrow pointing at a typical contacting surface of two ZnO particles. (b) The simulated distribution of temperature increase near the contacting surface in (a) pointed by the arrow. 48

Fig. 5.1 Schematic representation of ZnO rods and platelets formation by hydrothermal synthesis. 52

Fig. 5.2 Schematics of the consolidation process for (a) rods, (b) platelets and (c) nanoparticles, respectively. The consolidated samples of the rods and platelets were cut and characterized along both perpendicular ($\perp p$) and parallel ($\parallel p$) directions to the pressure axis. The anisotropy of the consolidated sample of the nanoparticles was negligible. 53

Fig. 5.3 (a) SEM images of hydrothermally grown Al-doped ZnO rods. (b) TEM image of a single rod and (c) its electron diffraction pattern along the $\langle 210 \rangle$ direction, indicating the wurtzite structure. SEM images of the fracture surfaces of the Rod sample (d) perpendicular ($\perp p$) and (e) parallel ($\parallel p$) to the pressure 55

axis.

Fig. 5.4 (a) SEM images of hydrothermally grown Al doped ZnO platelets. (b) A TEM image of a single platelet and (c) its electron diffraction pattern along the $\langle 001 \rangle$ direction, indicating the wurtzite structure. SEM images of the fracture surfaces of the Platelet sample (d) perpendicular ($\perp p$) and (e) parallel ($\parallel p$) to the pressure axis. 56

Fig. 5.5 (a) An HRTEM image of Al-doped ZnO nanoparticles. (b) A TEM image of the nanoparticles and (c) its selected-area electron diffraction pattern. (d) An SEM image of a bulk consolidated fracture surface of the Nanoparticle sample consolidated from nanoparticles. (e) A high magnification SEM image of the Nanoparticle sample showing highly dispersed nanoprecipitates within the ZnO nanograins. 57

Fig. 5.6 X-ray diffraction patterns of the samples. The inset shows the degrees of orientation and the unit cell volume. The red and blue columns indicate the degrees of (100) orientation and (001) orientation, respectively. 58

Fig. 5.7 Temperature dependence of the electrical conductivity of the samples, a clear anisotropy of the Rod and Platelet samples being observed. 59

Fig. 5.8 The carrier concentration and carrier mobility of the samples at room temperature. The inset shows the monotonic increase of the power factor with increasing carrier mobility. 60

Fig. 5.9 (a) Temperature dependence of the Seebeck coefficient of the samples. The inset shows the plot of the room temperature Seebeck coefficient vs. (carrier concentration) $^{-2/3}$. The colored diagonal lines correspond to the theoretical relationship when $m^*/m_e = 0.43$ and 0.35 according to the Pisarenko relation. (b) The Seebeck coefficient plotted as a function of the carrier concentration. The solid colored lines are the calculated values for $\lambda = 0, 1,$ and 2 , denoting electron scattering by acoustic phonons, optical phonons, and ionized impurities respectively. 61

Fig. 5.10 (a) Temperature dependence of the thermal conductivity of the samples. The inset shows the calculated Lorenz number of the samples as a function of temperature. The lower limit of the lattice thermal conductivity, κ_{\min} , for $\text{Zn}_{0.98}\text{Al}_{0.02}\text{O}$ was calculated using Cahill's equation (dashed line). (b) Temperature dependence of lattice thermal conductivity of the samples. The solid color lines are the calculated values using the Debye-Callaway model. 62

Fig. 5.11 Calculated lattice thermal conductivity plotted as a function of (a) grain size, and (b) nanoprecipitate particle concentration at different temperatures. The calculated mean free path (MFP) of the phonons was plotted as a function of normalized phonon frequency at (c) 273K and (d) 1223K. The dots in (a) are 64

experimental values of Rod ($\perp p$), Rod ($\parallel p$), Plate ($\perp p$), and Plate ($\parallel p$), with grain sizes of 10 μm , 2 μm , 600 nm and 150 nm, respectively; the dashed lines in (c) and (d) are the reference MFP values without phonon scattering by neither grain boundaries nor nanoprecipitates, and the solid lines are predicted values when phonon scattering by either nanoprecipitates or grain boundaries dominates.

- Fig. 5.12 Temperature dependence of figure-of-merit, zT , of the samples. 65
- Fig. 6.1 (a) The XRD patterns for $\text{Zn}_{1-x}\text{Cd}_x\text{Sc}_{0.02}\text{O}$ ($x = 0$ to 0.15) samples. (b) Refined unit cell volume of the primary phase plotted as a function of Cd composition. 69
- Fig. 6.2 (a) The XRD patterns for $\text{Zn}_{0.9}\text{Cd}_{0.1}\text{Sc}_y\text{O}$ ($y = 0$ to 0.04) samples. (b) Refined unit cell volume of the primary phase plotted as a function of Sc composition. 70
- Fig. 6.3 SEM images for $\text{Zn}_{1-x}\text{Cd}_x\text{Sc}_{0.02}\text{O}$ ($x = 0$ to 0.15) samples. (a) $x = 0.05$, (b) $x = 0.1$, (c) $x = 0.125$, and (d) $x = 0.15$. 71
- Fig. 6.4 SEM images for $\text{Zn}_{0.9}\text{Cd}_{0.1}\text{Sc}_y\text{O}$ ($y = 0.01$ to 0.04) samples. (a) $x = 0.01$, (b) $x = 0.02$, (c) $x = 0.03$, and (d) $x = 0.04$. 72
- Fig. 6.5 SEM-EDS elementary mapping for $\text{Zn}_{0.9}\text{Cd}_{0.1}\text{Sc}_{0.02}\text{O}$ sample. 73
- Fig. 6.6 Temperature dependence of electrical resistivity for $\text{Zn}_{1-x}\text{Cd}_x\text{Sc}_{0.02}\text{O}$ ($x = 0$ to 0.15) samples. 74
- Fig. 6.7 Temperature dependence of electrical resistivity for $\text{Zn}_{0.9}\text{Cd}_{0.1}\text{Sc}_y\text{O}$ ($y = 0.006$ to 0.04) samples. 74
- Fig. 6.8 Temperature dependence of electrical resistivity for $\text{Zn}_{0.9}\text{Cd}_{0.1}\text{A}_{0.02}\text{O}$ ($\text{A} = \text{Sc, Ga, Sn, Ce}$) and $\text{Zn}_{0.9}\text{Cd}_{0.1}\text{Sc}_{0.01}\text{B}_{0.02}\text{O}$ ($\text{B} = \text{Mg, Sn, Ce}$) samples. 75
- Fig. 6.9 The carrier concentration and carrier mobility of the samples at room temperature. 76
- Fig. 6.10 Temperature dependence of Seebeck coefficient for $\text{Zn}_{1-x}\text{Cd}_x\text{Sc}_{0.02}\text{O}$ ($x = 0$ to 0.15) samples. The inset shows the plot of the room temperature Seebeck coefficient vs. x in $\text{Zn}_{1-x}\text{Cd}_x\text{Sc}_{0.02}\text{O}$. 77
- Fig. 6.11 Temperature dependence of Seebeck coefficient for $\text{Zn}_{0.9}\text{Cd}_{0.1}\text{Sc}_y\text{O}$ ($y = 0.006$ to 0.04) samples. The inset shows the plot of the room temperature Seebeck coefficient vs. y in $\text{Zn}_{0.9}\text{Cd}_{0.1}\text{Sc}_y\text{O}$. 77
- Fig. 6.12 Temperature dependence of Seebeck coefficient for $\text{Zn}_{0.9}\text{Cd}_{0.1}\text{A}_{0.02}\text{O}$ ($\text{A} = \text{Sc, Ga, Sn, Ce}$) and $\text{Zn}_{0.9}\text{Cd}_{0.1}\text{Sc}_{0.01}\text{B}_{0.02}\text{O}$ ($\text{B} = \text{Mg, Sn, Ce}$) samples. 78

- Fig. 6.13 Seebeck coefficient plotted as a function of the carrier concentration for (a) the $\text{Zn}_{0.9}\text{Cd}_{0.1}\text{Sc}_y\text{O}$ ($y = 0.01$ to 0.04) samples whose $m^* \sim 0.585 m_e$, (b) the $\text{Zn}_{0.95}\text{Cd}_{0.05}\text{Sc}_{0.02}\text{O}$ sample whose $m^* \sim 0.329 m_e$, and (c) the $\text{Zn}_{0.9}\text{Cd}_{0.1}\text{Ga}_{0.02}\text{O}$ sample whose $m^* \sim 0.485 m_e$. The solid colored lines are the calculated S values for $\lambda = 0, 1,$ and 2 , denoting electron scattering by acoustic phonons, optical phonons, and ionized impurities respectively. 79
- Fig. 6.14 Temperature dependence of power factor for $\text{Zn}_{1-x}\text{Cd}_x\text{Sc}_{0.02}\text{O}$ ($x = 0$ to 0.15) samples. 80
- Fig. 6.15 Temperature dependence of power factor for $\text{Zn}_{0.9}\text{Cd}_{0.1}\text{Sc}_y\text{O}$ ($y = 0.006$ to 0.04) samples 80
- Fig. 6.16 Temperature dependence of power factor for $\text{Zn}_{0.9}\text{Cd}_{0.1}\text{A}_{0.02}\text{O}$ ($A = \text{Sc}, \text{Ga}, \text{Sn}, \text{Ce}$) and $\text{Zn}_{0.9}\text{Cd}_{0.1}\text{Sc}_{0.01}\text{B}_{0.02}\text{O}$ ($B = \text{Mg}, \text{Sn}, \text{Ce}$) samples. 81
- Fig. 6.17 (a) Temperature dependence of total thermal conductivity for $\text{Zn}_{1-x}\text{Cd}_x\text{Sc}_{0.02}\text{O}$ ($x = 0$ to 0.15) samples. (b) Temperature dependence of lattice thermal conductivity of the samples. The solid color lines are the calculated values using the Debye-Callaway model. 81
- Fig. 6.18 Temperature dependence of the lattice thermal conductivity for $\text{Zn}_{0.9}\text{Cd}_{0.1}\text{Sc}_y\text{O}$ ($y = 0.006$ to 0.04) samples. (b) Temperature dependence of lattice thermal conductivity of the samples. The solid color lines are the calculated values using the Debye-Callaway model. 83
- Fig. 6.19 (a) Temperature dependence of total thermal conductivity for $\text{Zn}_{0.9}\text{Cd}_{0.1}\text{A}_{0.02}\text{O}$ ($A = \text{Sc}, \text{Ga}, \text{Sn}, \text{Ce}$) and $\text{Zn}_{0.9}\text{Cd}_{0.1}\text{Sc}_{0.01}\text{B}_{0.02}\text{O}$ ($B = \text{Mg}, \text{Sn}, \text{Ce}$) samples. (b) Temperature dependence of lattice thermal conductivity of the samples. 84
- Fig. 6.20 Temperature dependence of figure-of-merit, zT , for $\text{Zn}_{1-x}\text{Cd}_x\text{Sc}_{0.02}\text{O}$ ($x = 0$ to 0.15) samples. 84
- Fig. 6.21 Temperature dependence of figure-of-merit, zT , for $\text{Zn}_{0.9}\text{Cd}_{0.1}\text{Sc}_y\text{O}$ ($y = 0.006$ to 0.04) samples. 85
- Fig. 6.22 Temperature dependence of figure-of-merit, zT , for $\text{Zn}_{0.9}\text{Cd}_{0.1}\text{A}_{0.02}\text{O}$ ($A = \text{Sc}, \text{Ga}, \text{Sn}, \text{Ce}$) and $\text{Zn}_{0.9}\text{Cd}_{0.1}\text{Sc}_{0.01}\text{B}_{0.02}\text{O}$ ($B = \text{Mg}, \text{Sn}, \text{Ce}$) samples. 86
- Fig. 6.23 Comparing the zT of $\text{Zn}_{0.9}\text{Cd}_{0.1}\text{Sc}_{0.01}\text{O}$ to (a) our previous results on Al doped ZnO [7,55]. (b) Al doped ZnO from literature results[10,35,52,53]. 86
- Fig. 6.24 Photographs of (a) a bulk pellet of $\text{Zn}_{0.9}\text{Cd}_{0.1}\text{Ga}_{0.02}\text{O}$ sintered in air, (b) a bulk pellet of $\text{Zn}_{0.9}\text{Cd}_{0.1}\text{Sc}_{0.02}\text{O}$ sintered in air, (c) a hexagonal segment cut from the pellet of $\text{Zn}_{0.9}\text{Cd}_{0.1}\text{Sc}_{0.02}\text{O}$, (d) a bulk pellet of $\text{Zn}_{0.98}\text{Al}_{0.02}\text{O}$ sintered by Spark Plasma Sintering in vacuum, (e) a hexagonal segment of $\text{ZnAl}_{0.02}\text{O}$ after 87

annealing in air at 1073K for 72h, (f) a hexagonal segment of $\text{Zn}_{0.9}\text{Cd}_{0.1}\text{Sc}_{0.02}\text{O}$ after annealing in air at 1073K for 72h.

Fig. 6.25 Resistivity of $\text{Zn}_{0.9}\text{Cd}_{0.1}\text{Sc}_{0.02}\text{O}$ and $\text{ZnAl}_{0.02}\text{O}$ measured in air. 88

Fig. 6.26 Time dependence of zT values, resistivity and Seebeck coefficient at 1173 K for $\text{Zn}_{0.9}\text{Cd}_{0.1}\text{Sc}_{0.02}\text{O}$ sample after annealing in air at 1073 K. 88

List of Tables

| | Page |
|--|------|
| Table 6.1 Parameters from Rietveld refinement for $\text{Zn}_{1-x}\text{Cd}_x\text{Sc}_{0.02}\text{O}$ ($x = 0$ to 0.15) samples. | 70 |
| Table 6.2 Parameters from Rietveld refinement for $\text{Zn}_{0.9}\text{Cd}_{0.1}\text{Sc}_y\text{O}$ ($y = 0$ to 0.04) samples. | 70 |
| Table 6.3 Electrical transport properties at room temperature | 76 |
| Table 6.4 Parameters used in Callaway calculations for $\text{Zn}_{1-x}\text{Cd}_x\text{Sc}_{0.02}\text{O}$ ($x = 0$ to 0.15). | 83 |
| Table 6.5 Parameters used in Callaway calculations for $\text{Zn}_{0.9}\text{Cd}_{0.1}\text{Sc}_y\text{O}$ ($y = 0.006$ to 0.04) samples. | 83 |

Chapter 1 Introduction

This chapter gives an introduction to the field of thermoelectric materials and ZnO based thermoelectric materials. It first introduces the fundamentals and background for thermoelectrics, in which the Seebeck effect, figure of merit zT and the low-dimensional thermoelectrics will be introduced. Then the ZnO based thermoelectric materials and their current research status will be discussed. The issues and challenges for ZnO based thermoelectrics, mostly concerning nanostructuring and long-term stability will also be discussed. Lastly, the thesis outline will be presented.

1.1 Fundamentals for Thermoelectrics

1.11 Seebeck effect

The thermoelectric effect describes what is happening to a conductor/semiconductor when it is subjected to a temperature difference or alternatively when a current is passed through it. Actually, the term "thermoelectric effect" includes three different effects: the Seebeck effect, Peltier effect, and Thomson effect. In this thesis, I only focus on the Seebeck effect.

The Seebeck effect was first discovered by Thomas Johann Seebeck in 1821.[1] He found that a magnetic compass would be deflected when brought near a closed loop formed by two different metals joined together with the two junctions at different temperatures. Even though he mistakenly interpreted this effect as magnetism, and it was the Danish physicist Hans Christian Ørsted who rectified the mistake and coined the term "thermoelectricity", the discovery was still name after the discoverer, Thomas Johann Seebeck.

The Seebeck effect can be used for electric power generation. Unlike the conventional generator that converts mechanical energy into electrical energy, the thermoelectric generator does not need any moving parts. It converts heat directly into electricity. The process can be illustrated by the schematics shown in Fig.1.1. When a temperature gradient is applied across a material, the charge carriers at the hot side become more energetic and they tend to diffuse from the hot side to the cold side. As the carriers accumulate at the cold side, the charge neutrality is broken and an internal electrical field is built to avoid further migration of the carriers. Finally a balance is achieved and an electrical voltage difference is obtained across the material as long as the temperature gradient exists, this is known as an open circuit voltage (OCV). In the case of electrons as the dominant carriers, which is called n-type thermoelectric materials, the hot side becomes positively charged as the electrons diffuse away from the hot side; in the case of holes, being p-type thermoelectric materials, the polarity is the opposite (see Fig. 1.1(a)).

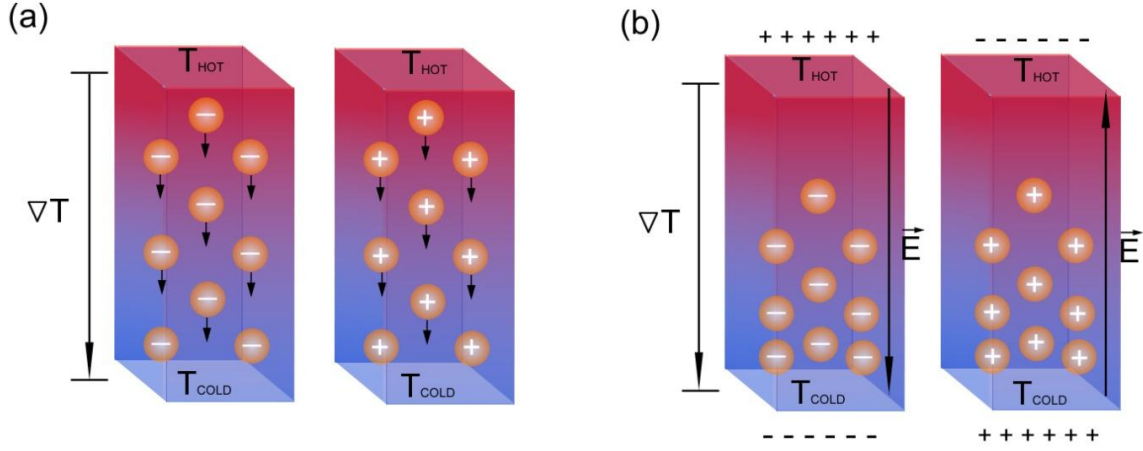


Fig. 1.1 Schematics illustrations of the Seebeck effect: (a) when a temperature gradient is given to n-type and p-type materials, the charge carriers diffuse towards the cold side; (b) an internal electrical field is built up, and equilibrium is reached, and an electrical voltage difference is obtained across the material as long as the temperature gradient exists.

For a homogenous material, the electrical voltage difference (ΔV) obtained across the material is proportional to the temperature difference (ΔT). The proportionality constant of the voltage difference over the temperature difference ($\Delta V / \Delta T$) is defined as the Seebeck coefficient, S , with the unit of V/K. This is also known as the thermopower.

The physical meaning of the Seebeck coefficient is the entropy transported per charge carrier[2], which can be written as

$$S = \frac{1}{e} \frac{\partial S_n}{\partial n} \quad (1.1)$$

where n is the carrier density and S_n the entropy density of the charge carriers. It can be also expressed as the electronic heat capacity per charge carrier, which can be written as

$$S = \frac{1}{e} \frac{C_{el}}{N} = \frac{1}{e} \frac{\partial U_{el}}{N \partial T} \quad (1.2)$$

where C_{el} is the total electronic heat capacity for the system, e is the electronic charge, N is the number of electrons in the system, and U_{el} is the total thermal kinetic energy carried by the electrons. Not all of the electrons in a material can contribute to the Seebeck coefficient. Only those who participate in the conduction process contribute to the Seebeck coefficient. For non-degenerate semiconductors, charged carriers need to be excited across the bandgap, E_g , to contribute to the Seebeck coefficient. At a temperature T , the number of carriers for conduction is $\sim (N \cdot E_g) / (k_B \cdot T)$, in which k_B is the Boltzmann constant. So the total electronic thermal kinetic energy can be written as,

$$U_{el} \approx \left(\frac{N E_g}{k_B T} \right) k_B T = N E_g \quad (1.3)$$

Combining it with the previous equation, one can have,

$$S = \frac{k_B}{e} \left(\frac{E_g}{k_B T} \right) = \frac{1}{e} \frac{E_g}{T} \quad (1.4)$$

where k_B/e is the Seebeck coefficient for a classical electron gas.

As for metals or degenerated semiconductors, it is also only the portion of the electrons in the system that are thermally excited that can contribute to the Seebeck coefficient. At a temperature of T , the number of electrons that participate in the conduction process is approximately $N(T/T_F)$ where T_F is the Fermi temperature[3]. The Fermi temperature is related to Fermi energy by $T_F = E_F/k_B$. Accordingly, the Seebeck coefficient for metals or degenerated semiconductors can be expressed as[4],

$$S \approx \frac{2}{e} \frac{k_B^2 T}{E_F} = \frac{2k_B}{e} \left(\frac{k_B T}{E_F} \right) \quad (1.5)$$

Additionally, the Fermi energy for a parabolic band approximation can be expressed as a function of the effective mass, m^* , and carrier concentration, n , as,

$$E_F = \frac{\hbar^2}{2 m^*} (3\pi^2 n)^{\frac{2}{3}} \quad (1.6)$$

where \hbar is the Planck constant. Inserting eq. 1.6 into 1.5 gives the commonly used expression for the Seebeck coefficient of degenerate semiconductors [5],

$$S \approx \frac{8\pi^2 k_B^2}{3e \hbar^2} m^* T \left(\frac{\pi}{3n} \right)^{\frac{2}{3}} \quad (1.7)$$

The above expression implies that a large Seebeck coefficient requires either a large effective mass or a small carrier concentration.

As the Seebeck effect can be used for electrical power generation, thermoelectric generators thus emerged based on this effect. The most common set-up for a thermoelectric generator is a configuration where the p-n unicouples are electrically connected in series and thermally connected in parallel, as shown in Fig. 1.2. The uncouple arrays are stack between two ceramic plates. These plates are usually made of insulator ceramics with relatively good heat conductivity, for example, alumina. When contacting this module to a heat source, one side absorbs the heat, while the other side releases the heat with the help of a heat sink. A heat flux penetrates through the module and a temperature difference along the heat transfer direction is created, which results in a potential difference across each the leg. The total electrical voltage of the module is the sum-up of the absolute voltage values from every p- and n-type leg.

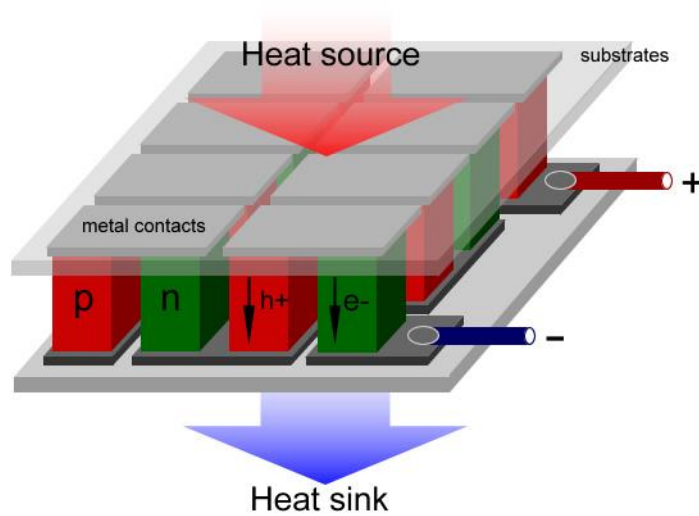


Fig. 1.2 A schematic illustration of a thermoelectric generator module.

1.12 Figure of Merit, zT

The maximum conversion efficiency for a thermoelectric generator is calculated according to the equation[6],

$$\eta_{max} = \frac{\Delta T}{T_h} \frac{\sqrt{1+ZT}-1}{\sqrt{1+ZT}+T_c/T_h} \quad (1.8)$$

where T_h , T_c , and ΔT corresponds to the hot side temperature, cold side temperature, and the temperature difference, respectively. $\Delta T/T_h$ corresponds to the Carnot efficiency—the maximum efficiency of a heat engine operating between two temperatures. The term ZT is the device dimensionless figure of merit, which is independent of the engineering design of the modules. The maximum possible conversion efficiency, η_{max} , is directly related to ZT . An example is given in Fig.1.3. Given different values for T_h and T_c , η_{max} can be plotted as a function of ZT . As clearly shown in the picture, η_{max} monotonically increases with the increasing ZT , indicating that maximizing ZT is the key to the best energy conversion efficiency and should be the main focus for the thermoelectric research from the material science perspective.

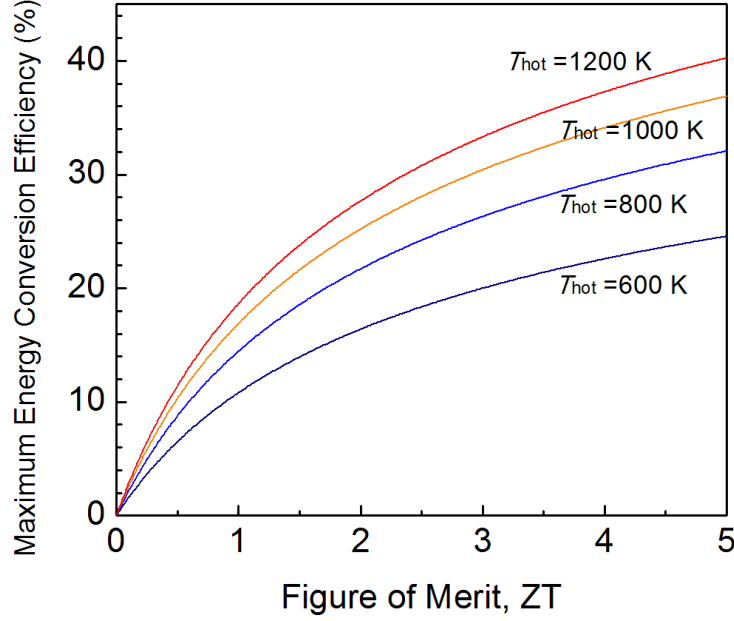


Fig. 1.3 Calculated plot of maximum energy conversion efficiency as a function of the figure of merit ZT . Calculations were made according to Eq. 1.8 with $T_{\text{cold}} = 300$ K.

Another indication from Fig.1.3 is that there is an improvement for η_{max} if the module is operating at a higher temperature with a larger ΔT . It shows the advantage of developing high temperature thermoelectric materials, especially oxide thermoelectric materials that can normally survive over 1000 °C.

Different from the effective device ZT , the material's figure of merit zT is a pure material property related to both electrical transport properties and thermal transport properties. It is given by the expression,

$$zT = \frac{S^2 \sigma}{\kappa} T \quad (1.9)$$

where S is the Seebeck coefficient, σ is the electrical conductivity, and κ is the thermal conductivity. A high zT requires a large Seebeck coefficient, a high electrical conductivity and a low thermal conductivity. Some describe this as 'electron crystal and phonon glass' [5]. The electrical conductivity σ is a function of carrier mobility μ and carrier concentration n , which can be expressed as,

$$\sigma = en\mu \quad (1.10)$$

where e is the electronic charge. μ is an intrinsic property of a material related to its electronic band structure as well as the scattering mechanisms at work in the material. The thermal conductivity κ is the sum of two portions— the lattice part, κ_L , and the electrical part, κ_{el} . For the lattice part, it is determined by the heat capacity and the mean free path of phonons [6]. For the electrical part, it is a function of carrier concentration n , which is given by,

$$\kappa_{el} = \sigma LT = ne\mu LT \quad (1.11)$$

where L is known as the Lorentz number. The upper limit of the Lorentz number derived for a free electron gas is $2.45 \times 10^{-8} \text{ W}\Omega\text{K}^{-2}$, note that this value is valid only for highly degenerate semiconductors regardless of the carrier scattering mechanisms[7]. So the total thermal conductivity can be written as,

$$\kappa = \kappa_L + \kappa_{el} = \kappa_L + ne\mu LT \quad (1.12)$$

One can see that once the carrier concentration as well as the electrical conductivity increases, the thermal conductivity will also increase accordingly.

The Seebeck coefficient S is also related to the carrier concentration, n , as shown by Eq. 1.7. The increase of n will result in a decrease of S . So for the zT value, the carrier concentration plays an important role for S , σ , and κ_{el} . Plotting the thermoelectric parameters of σ , S , κ , and zT as a function of n , there exists a trade-off relationship among them[5]. However, the optimized zT can be realized by tuning the carrier concentration to a proper value, as shown in Fig.1.4. Good thermoelectric materials are typically heavily doped semiconductors with a carrier concentration between 10^{18} and 10^{21} cm^{-3} .

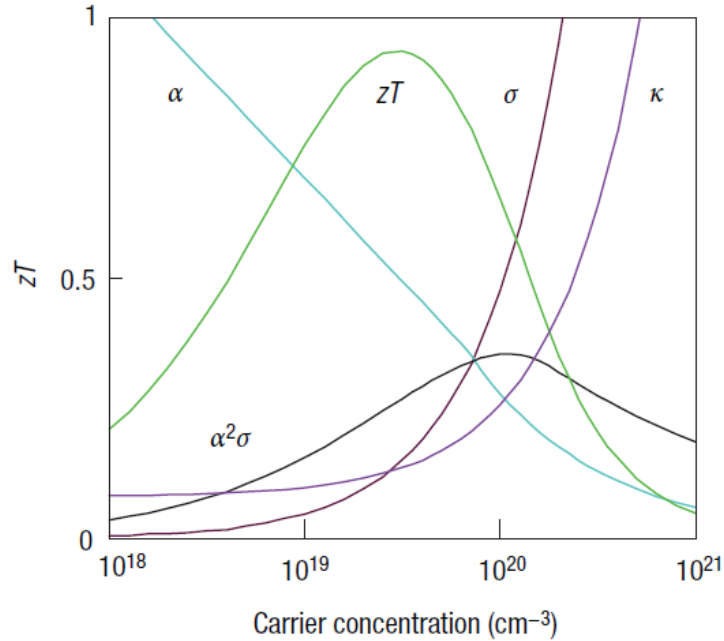


Fig. 1.4 The trade-off relationship among the Seebeck coefficient, S , electrical conductivity, σ , and thermal conductivity, κ . Optimizing zT involves a compromise of these values. Figure taken from Snyder and Toberer's work[5].

Independent from the carrier concentration, the lattice thermal conductivity, κ_L , also plays a key role in improving zT . Throughout the few last decades, a large amount of research works has been focused on reducing materials' lattice thermal conductivity[8–12]. Another example from Snyder and Toberer [5] illustrated the significant effect of reducing the lattice thermal conductivity on increasing the zT , as shown in Fig. 1.5.

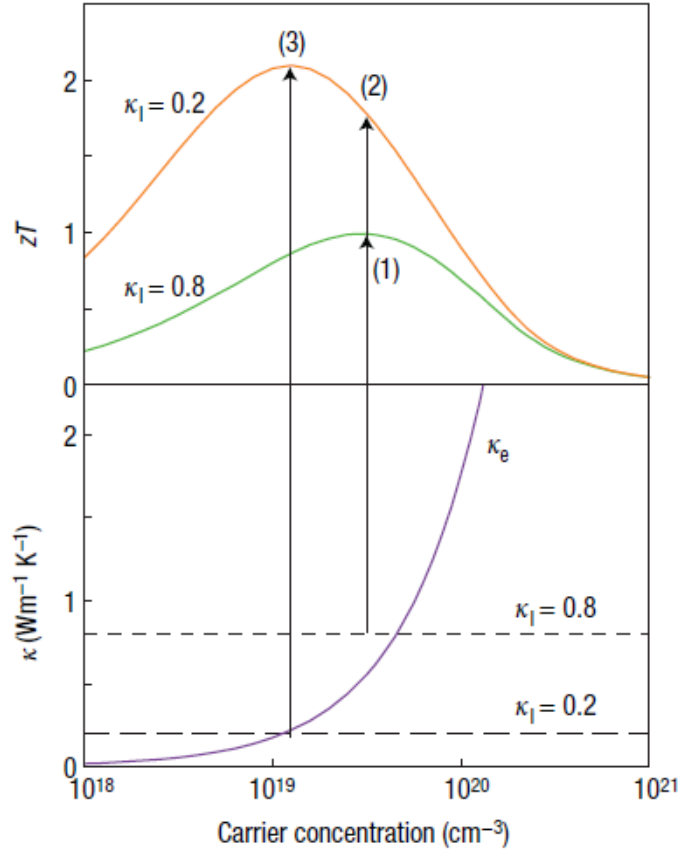


Fig. 1.5 The improvement of zT by reducing the lattice thermal conductivity, κ_L . The carrier concentration will be re-optimized as κ_L reduces. Figure taken from Snyder and Toberer's work[5].

1.13 Nanostructuring in thermoelectrics

Phonon transport is different from that of electrons, the electrons always 'choose' the way to go which this is not the case for phonons. The mean free path for electrons is only on the order of a few angstroms to a few nano-meters, while the mean free path for phonons has a wide distribution from nano-meters to several hundred micron-meters depending on the crystal structure and microstructure of the material. As a result, the scattering sites with a length scale larger than a few nanometers do not affect the electrons very much but can effectively scatter the phonons that have comparable mean free paths. This phenomenon provided a promising strategy to suppress the lattice thermal conductivity of a material while giving minor influences to the electronic transport. This strategy is called 'nanostructuring' or 'low dimensional thermoelectrics'[13–16]. Since the 90s, Dresselhaus et al has theoretically predicted and experimentally proved that the 1D quantum wires and 2D quantum wells could obtain enhanced zT over the bulk materials[17–19]. Nowadays, the highest zT values over 2 have been achieved through nanostructuring [9] and from materials with natural 2D super lattice structures[20]. A typical example showing how nanostructuring works is shown in Fig. 1.6, which is taken from Dresselhaus's work[16]. As the system size decreases to nanometer scales, it is possible to cause dramatic change in the density of electronic states (DOS), allowing new opportunities to vary S ,

σ , and κ quasi-independently when the length scale is small enough to give rise to quantum-confinement effects.

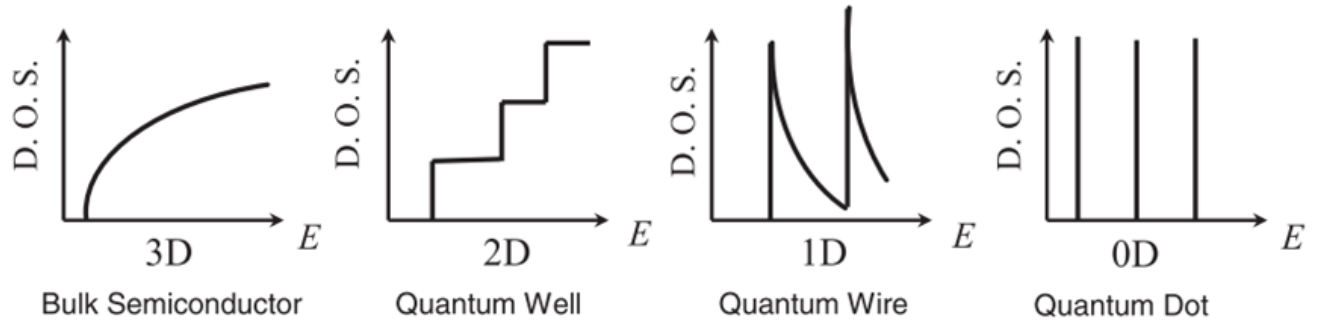


Fig. 1.6. Illustrations of the electronic density of states (DOS) of low-dimensional semiconductors. Figure taken from Dresselhaus’s work[16].

Another example illustrates the use of nanostructuring as the nano scaled scattering sites and numerous interfaces preferentially scattered phonons, thus dramatically reducing the thermal conductivity to a very low level, as shown in Fig. 1.7. Si nanoparticles and nanowires in a SiGe host material can result in very low thermal conductivity values, much lower than the minimum thermal conductivity value of a SiGe alloy[21].

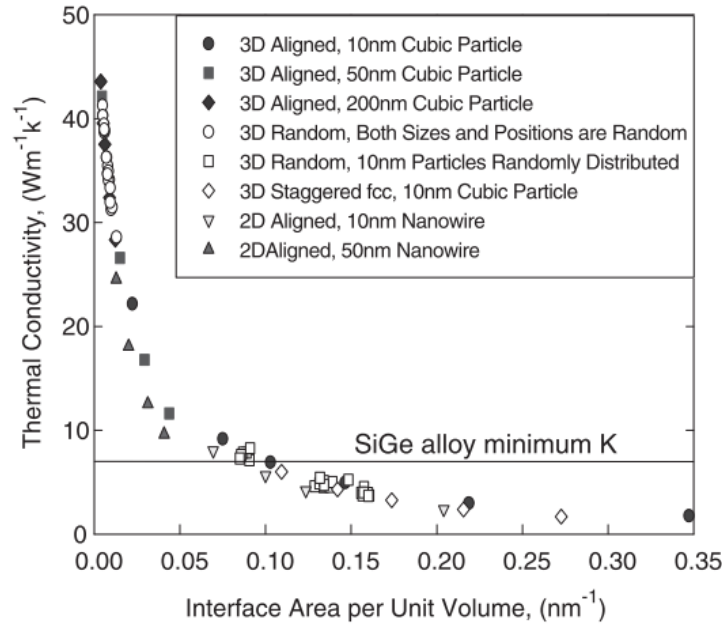


Fig. 1.7 Effects of interfacial scattering on the reduction of the thermal conductivity by adding Si nanoparticles and nanowires into SiGe host material. Figure taken from Dresselhaus’s work[16].

The zT values have been improved over the years for conventional thermoelectric materials owing to the nanostructuring strategy which was been employed. As shown in Fig.1.8, for example, the nanostructured BiSbTe reached a peak zT of 1.4 which is 40% higher than the bulk BiSbTe without nanostructuring[22]. n-SiGe [23] and p-SiGe [24] also obtained similarly large

improvement of zT by nanostructuring. Other than that, PbTe gained the most significant improvement by nanostructuring, which resulted in the peak zT values higher than 1.5[25] or even 2.2[9].

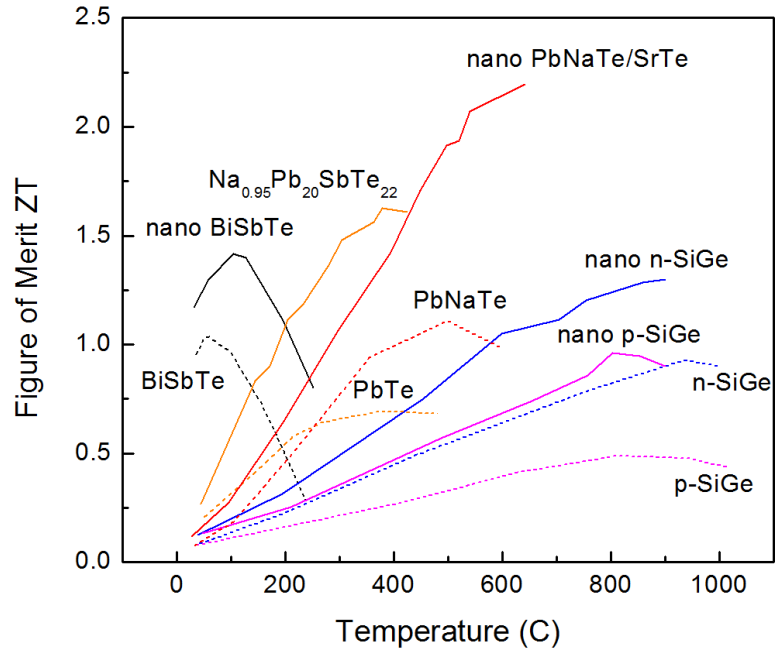


Fig. 1.8 Literature values of zT for state the art thermoelectric materials. The dashed lines are the maximum zT values for bulk materials, and the solid lines are from nanostructured materials. (BiSbTe, and nano BiSbTe, Ref. [22]; n-SiGe, nano n-SiGe, Ref. [23]; p-SiGe, nano p-SiGe, Ref.[24] ; PbNaTe, and PbNaTe/SrTe, Ref.[9] ; PbTe, and Na_{0.95}Pb₂₀SbTe₂₂, Ref.[25]).

1.2 Oxide Thermoelectrics and ZnO based Thermoelectric Materials

1.2.1 Background for oxide thermoelectrics

Over the years other types of materials than the one described above were also developed as thermoelectric materials, these are for example organic conductive polymers[26] and oxide materials[27]. The emergence of thermoelectric oxide materials takes the thermoelectricity into the cost-effective, low-toxicity and high temperature air stable regime.

The state-of-the-art p-type oxide thermoelectric materials are the layered cobaltates, such as Ca₃Co₄O_{9-δ}, which has been reported to show zT values of 0.45 at 1000 K [28] and 0.65 at 1247 K[11]. Recently, Nan's group reported the p-type BiCuSeO ceramics with natural 2D super lattices. Its highest zT was reported to be over 1 at 800 K[29,30]. For n-type oxide thermoelectric materials, the popular materials include perovskite-type strontium titanate (SrTiO₃, or STO)[33], and calcium manganate (CaMnO₃, or CMO)[32]. Appropriate doping at A-site or B-site in those compounds can induce excess electrons and causing them to exhibit n-type conductivity. The doping can be easily achieved in a reducing atmosphere so that excess oxygen can be emitted to the gas phase and the doping process is promoted. However, for STO the Ti³⁺ ions are not stable and can be easily oxidized to Ti⁴⁺ above 650K in air, so the crystal becomes insulator. For CMO

the Mn^{3+} ions are more stable than Ti^{3+} ions, so the doped CMO can be stably conductive in air at high temperatures. Thus STO can be used only for medium-temperature (300-600K) applications, while CMO can be used up to high-temperature (above 1000K) applications, the highest zT for both materials are around 0.3[33][34]. A collection of zT values from typical oxide thermoelectric materials (both n and p-type) is shown in Fig. 1.9. The zT values are all taken from literature[11,30,32,34–36].

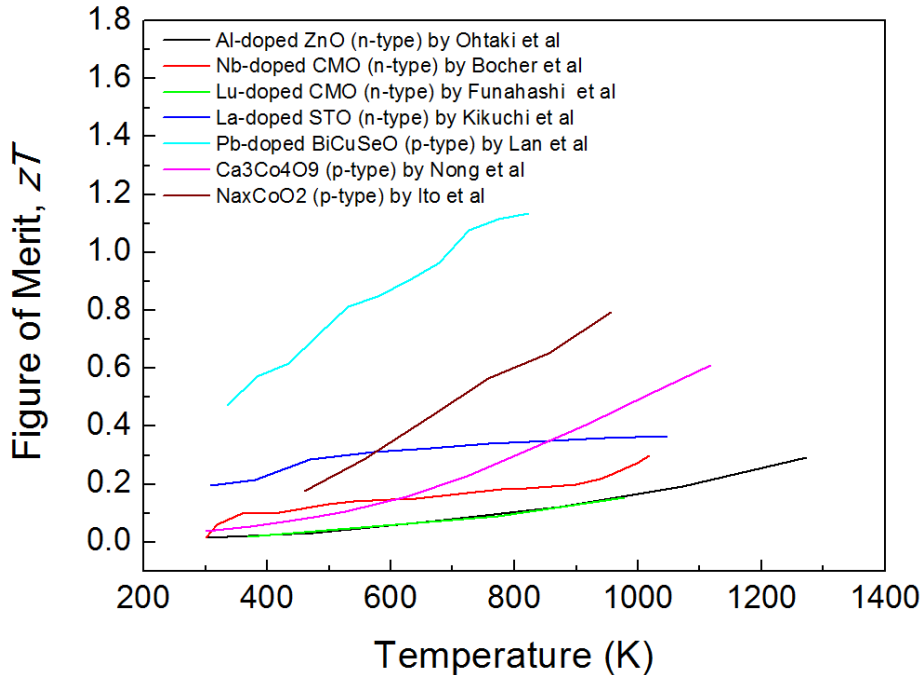


Fig. 1.9 Re-plotting zT values of oxide thermoelectric materials from literature[11,30,32,34–36].

1.2.2 Background for ZnO based thermoelectrics

ZnO is a well known wide direct band gap semiconductor. Research on ZnO has continued for many decades with interest for its potential applications in many fields. Owing to its direct wide band gap ($E_g \sim 3.37$ eV at 300 K), ZnO is most famous in its prospects for optoelectronics applications [37–40]. Other applications such as fabrication of transparent thin-film transistors, and spintronics applications are also intensively investigated and reported [41–43]. ZnO can also be doped with donor impurities and changed from an insulator to an n-type semiconductor and then to a material with metal-like conductivity while maintaining optical transparency. That makes it useful for transparent electrodes in flat-panel displays and solar cells[44–47]. The doping induced n-type electrical conductivity and carrier mobility also give rise to its potential as an n-type oxide thermoelectric.

The most common crystal structure of ZnO is the hexagonal wurtzite structure. It is most stable at ambient conditions. The zincblende structure is a rare form of ZnO which only exists at relatively high pressures of about 10 GPa. However it can be stabilized by growing a ZnO thin film on a substrate with a cubic lattice structure. In both cases, the zinc and oxygen centers are tetrahedral, the most characteristic geometry for Zn(II). A schematic of ZnO crystal structure is

shown in Fig.1.10a. The powder X-ray diffraction pattern of a standard ZnO gives the characteristic peaks for a ZnO poly crystal, and the cell parameters can be obtained by refinement. As shown in Fig. 1.10b, the lattice parameters a and c are 3.24Å and, 5.20Å, respectively. The calculated unit cell volume is 47.62 Å³.

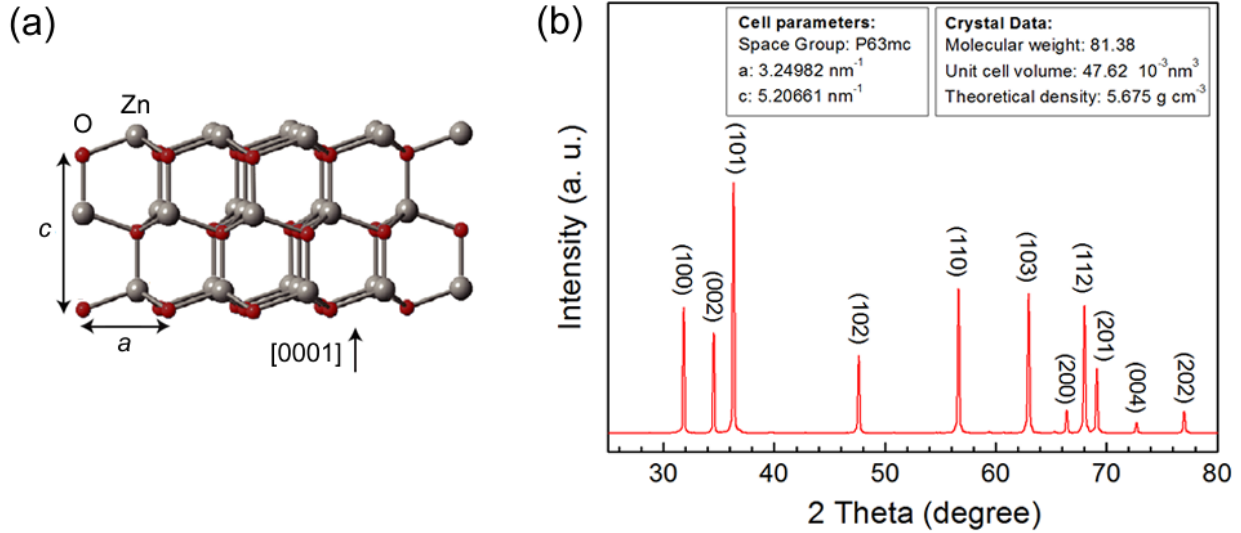


Fig. 1.10 (a) A schematic of the wurtzite ZnO crystal structure. (b) A powder diffraction pattern for ZnO.

Because of the simple crystal structure and light element composition as shown above, ZnO would suffer from the high thermal conductivity, e.g. 49 Wm⁻¹K⁻¹ at 300K and 10 Wm⁻¹K⁻¹ at 1000K[35], which is very unfavorable for thermoelectrics. However the electrical transport properties of ZnO are high with a carrier mobility over 200 cm²V⁻¹S⁻¹ at 300K which reaches as high as 1350 cm²V⁻¹S⁻¹ at 80K, as shown in Fig. 1.11a, according to Lin's work[48]. The effective mass of the ZnO was measured by Kim et al.[49], and reported to be about 0.3 to 0.45 m_e depending on the carrier densities as shown in Fig. 1.11b. The value for m^* is in fact moderate, which offers a decent Seebeck coefficient for ZnO while giving minor harm to its carrier mobility.

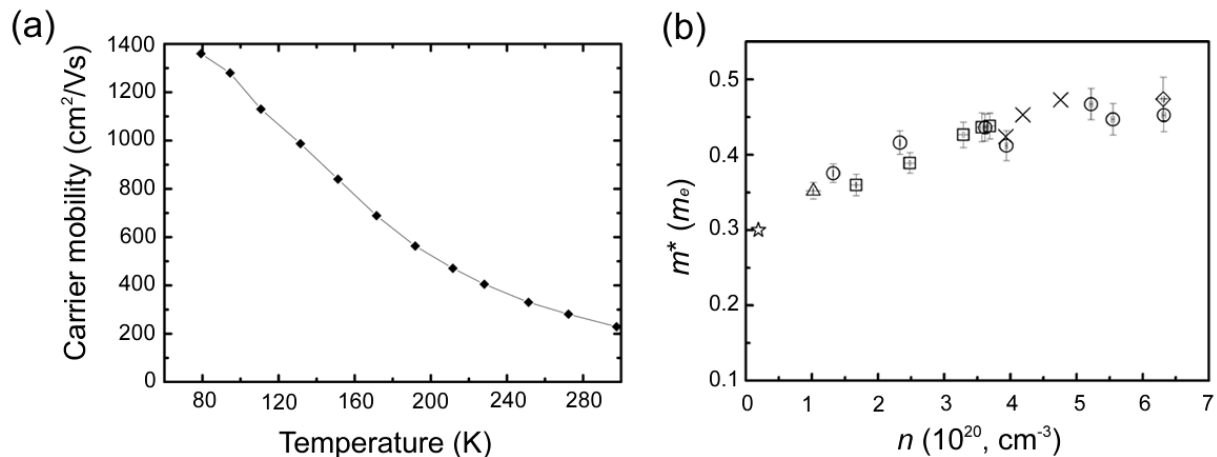


Fig. 1.11 (a) Carrier mobility of a ZnO single crystal as function of temperature. Figure is taken from

Lin's work [48]. (b) DOS effective mass, m^* , for ZnO as a function of the carrier concentration n . m_e is the free electron mass. Figure is taken from Kim's work [49].

Given the good electronic transport properties of ZnO, the thermoelectric properties of ZnO were not discovered until Ohtaki doped ZnO with Al and the zT was significantly increased[35,50]. Doping ZnO with Al introduced excess electron charge carriers. The carrier concentration was increased from $5.2 \times 10^{17} \text{ cm}^{-3}$ of pure ZnO to $7.2 \times 10^{19} \text{ cm}^{-3}$ of 2 at%-Al-doped ZnO. Despite the high thermal conductivity of $\sim 7 \text{ W m}^{-1} \text{ K}^{-1}$ at $1000 \text{ }^\circ\text{C}$, the 2at%-Al-doped ZnO achieved a $zT \sim 0.3$ at $1000 \text{ }^\circ\text{C}$ owing to the high power factor, $S^2\sigma$, of $1.4 \times 10^{-3} \text{ W m}^{-1} \text{ K}^{-2}$ at $1000 \text{ }^\circ\text{C}$ [35]. An even higher zT of 0.65 at $1000 \text{ }^\circ\text{C}$ was later obtained by the Al, Ga-dually doped ZnO from Ohtaki's work [51]. Compared with the Al-doped sample, the thermal conductivity was reduced to $\sim 5 \text{ W m}^{-1} \text{ K}^{-1}$ at $1000 \text{ }^\circ\text{C}$, and at the same time, the power factor, $S^2\sigma$, was measured to be as high as $2.4 \times 10^{-3} \text{ W m}^{-1} \text{ K}^{-2}$ at $1000 \text{ }^\circ\text{C}$. Yet, there have not been any other groups who can repeat the same results. A collection of zT of ZnO based thermoelectric materials is shown in Fig. 1.12. The zT values are all taken from literature[35,51–56].

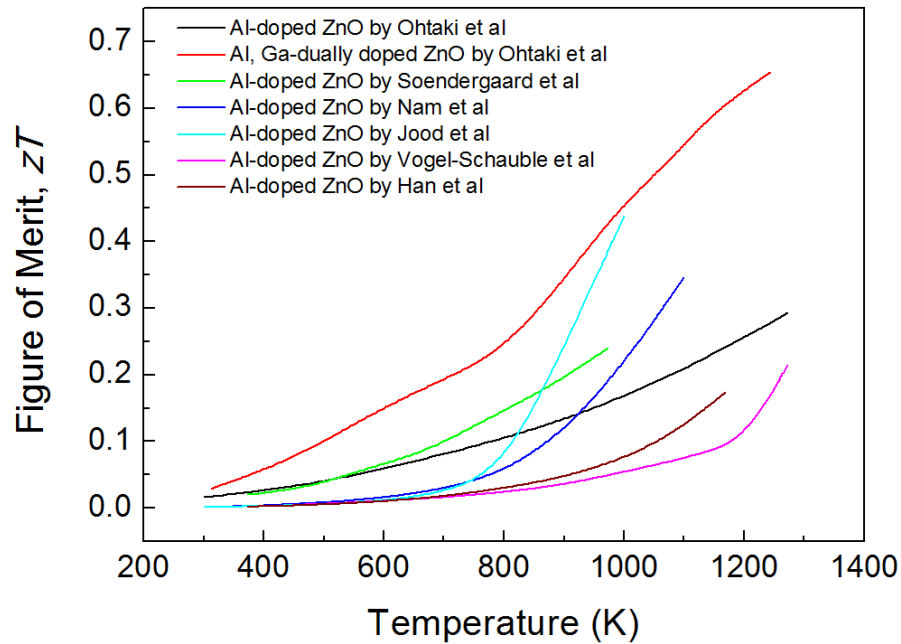


Fig. 1.12 Re-plotting zT of ZnO based thermoelectric materials from literatures[35,51–56]

1.2.3 Nanostructuring of ZnO thermoelectrics and the issues

Since 2010, the integration of nanostructuring to the ZnO based thermoelectrics has become a popular topic. Kinemuchi et al [57] synthesized nanograined ZnO using a pressure-induced deformation method. Bulk samples with grain sizes down to 30 nm were obtained. Though the thermal conductivity was successfully reduced down to $4 \text{ W m}^{-1} \text{ K}^{-1}$ at $800 \text{ }^\circ\text{C}$, the electrical conductivity was also greatly influenced by the strong interface scattering which led to a 10 times larger electrical resistivity while the Seebeck coefficient remained almost the same. The overall zT was not improved at all when comparing the nanograined samples to the normal bulk samples. In 2011, Jood et al [10] reported on the Al-doped ZnO nanocomposites sintered using

nano precursors made by a microwave-aided hydrothermal method. The thermal conductivity measured at room temperature was reduced down to $2.8 \text{ Wm}^{-1}\text{K}^{-1}$ compared to $49 \text{ Wm}^{-1}\text{K}^{-1}$ for bulk ZnO. Though the electrical conductivity was also reduced 10 times as compare to other bulk samples[35], the Seebeck coefficient was enhanced very much due to the boundary scattering. Extrapolating the thermal conductivity up to 1000 K, the authors reported a peak zT of 0.44. Nam et al[53] later investigated the charge transport properties of Al-doped ZnO nanocomposites. The hopping conduction mechanism was observed in those samples due to the boundary scattering. The hall carrier mobility kept increasing with the rising temperature as the grain boundaries acted as potential barriers to the electrons, while the carrier concentration remained the same.[53] As a result, the nanostructuring turned out to be very beneficial to high temperature zT of Al-doped ZnO, but the near room temperature zT is usually lower than the zT from bulk samples due to lower electrical conductivity. Generally, for ZnO nanocomposites, the high temperature thermoelectric properties are far better than those at room temperature, because the reduction of the thermal conductivity by boundary and interface scattering may be passivated by the loss of electrical conductivity (See Fig.1.13). This remains an issue for ZnO nanocomposites for its doubtable overall improvement of average zT values.

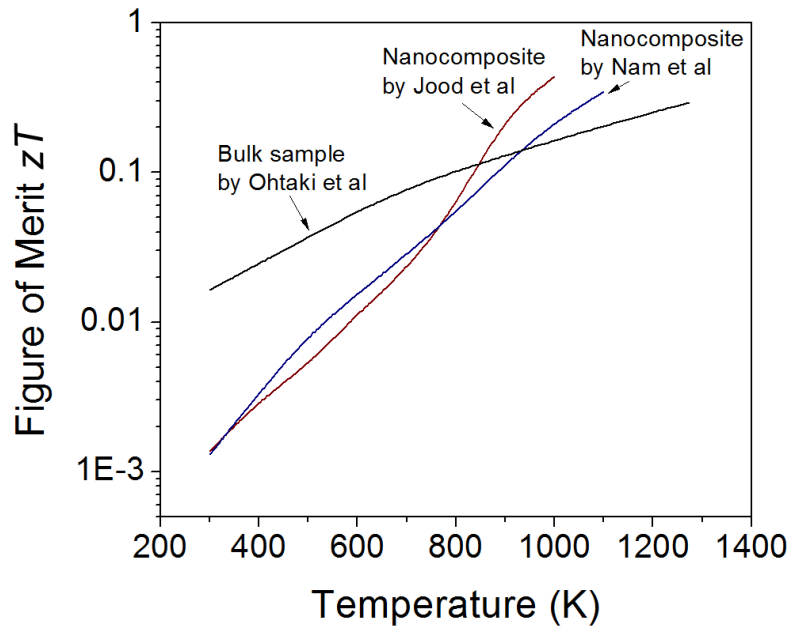


Fig. 1.13 The comparison of the figure of merit zT , between ZnO nanocomposites and bulk samples without nanostructuring. Data extracted from literature works by Ohtaki et al[35], Jood et al[10], and Nam et al[53].

1.2.4 Unstable thermoelectric properties of ZnO

Like many other oxide materials, the physical properties of the ZnO are sensitive to oxygen content, especially for Seebeck coefficient, S , and electrical conductivity, σ . There were previous investigations on the influence of preparation conditions for Al-doped ZnO by Berardan et al[58]. The samples were sintered in different atmosphere, either N_2 or air. The subsequent Seebeck coefficient and electrical resistivity measurements evidenced a large difference between air-

prepared and N₂-prepared samples. The power factor of the sample prepared in N₂ was more than twice as large as that of the air-prepared sample. Another example was given by Schäuble et al [59], who first deposited ZnO:Al nano-polycrystalline thin films on glass substrates using radio-frequency magnetron sputtering, then the S and σ of the films were measured under either air or Ar/H₂. The results showed that the reducing atmosphere Ar/H₂ decreased the $|S|$ but increased σ , while in air the effect is reversed, as shown in Fig. 1.14. The star-shaped marks in Fig. 1.14a and b represent two different statuses of the ZnO:Al thin films: the red star ‘1’ represents the as deposited oxygen deficient status; and the blue star ‘2’ represents the air-annealed oxygen rich status. It is easy to see that for the Seebeck coefficients, status ‘2’ has 10 times larger absolute values than status ‘1’; for electrical resistivity, status ‘2’ is 4 orders larger than status ‘1’.

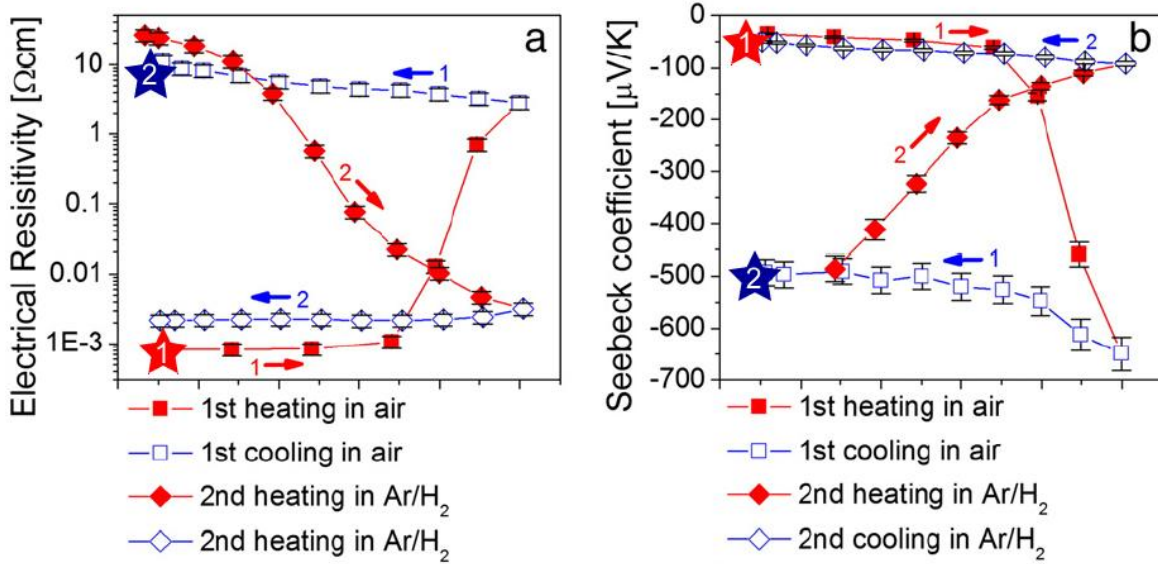


Fig. 1.14 Electrical resistivity and Seebeck coefficient of the ZnO:Al thin films as a function of temperature (first cycle in air and second cycle in Ar/H₂). Figure taken from the work of Schäuble et al [59]. The red star ‘1’ represents the as-deposited oxygen deficient status; and the blue star ‘2’ represents the air annealed oxygen rich status.

The fluctuation of S and σ observed in different atmospheres can be explained by the existence of native point defects in ZnO. ZnO is known as an intrinsic n-type oxide material. Its intrinsic n-type conduction originates from point defects like oxygen vacancies V_{O}^{2+} , zinc interstitials Zn_i^{2+} , and zinc antisite defects Zn_{O}^{2+} [60]. They are also the sources compensating the p-type doping for ZnO, which make it very difficult to make or maintain the p-type conduction for ZnO based materials. These defect sites are illustrated in Fig. 1.15. According to Janotti and Van de walle’s work [61], oxygen vacancies are deep donors and they can compensate p-type doping. Zinc interstitials have high diffusivity and they are shallow donors with high formation energies under n-type conditions. Zinc antisite defects are also shallow donors with high formation energies in n-type samples. Moreover, zinc antisite defects have large off-site displacements and induce large local lattice relaxations, as shown in Fig. 1.15c.

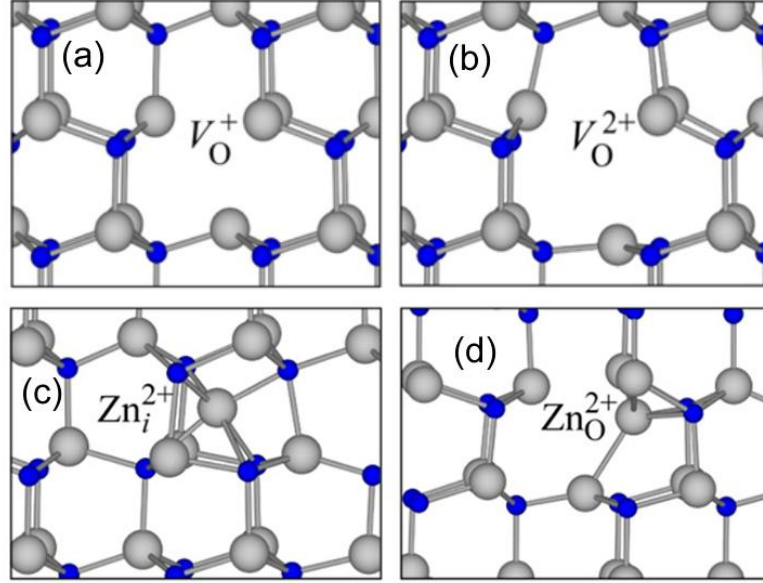
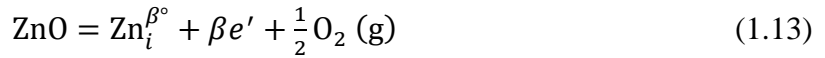


Fig. 1.15 Ball and stick model of the (a) +1 charge state oxygen vacancy, (b) +2 charge state oxygen vacancy, (c) zinc interstitial, (d) zinc antisite. Figure taken from Janotti and Van de walle's work [60].

The formations of these point defects follow these general reaction equations:



where $\delta, \beta, \lambda = 1$ or 2 , and the equilibrium constants of reactions (1.12)–(1.14) can be obtained using the mass action law, as expressed by the following equations:

$$K_{(V_O^{\delta^\circ})}^f = [V_O^{\delta^\circ}] [e']^\delta P_{O_2}^{1/2} \quad (1.15)$$

$$K_{(Zn_i^{\beta^\circ})}^f = [Zn_i^{\beta^\circ}] [e']^\beta P_{O_2}^{1/2} \quad (1.16)$$

$$K_{(Zn_O^{\lambda^\circ})}^f = [Zn_O^{\lambda^\circ}] [e']^\lambda P_{O_2}^{1/2} \quad (1.17)$$

where P_{O_2} represents the partial pressure of oxygen in the system. From these equations we can see that the probabilities of forming oxygen vacancies, zinc interstitials, and zinc antisite defects are all related to the partial pressure of oxygen in the system. The charge carrier concentrations are also directly related to these reactions. As discussed in section 1.12, as the carrier concentration increases, the electrical conductivity will increase but the absolute value of the Seebeck coefficient will decrease. The previously discussed observations by Schäuble et al [59]

clearly illustrate these reactions and their consequent influences on thermoelectric properties clearly.

The unstable thermoelectric properties of ZnO raises issues for the application of ZnO based materials as thermoelectrics, especially for those that are prepared in nitrogen but used in air. However, there are still possible solutions for this issue since the concentrations of native defect points are in equilibrium with the oxygen partial pressure. If the oxygen partial pressure can be maintained, the carrier concentration fluctuations could be minimized. Thus it is very important that the materials are prepared and used in the same atmosphere, as well as the measuring atmosphere. If this is not done properly, it is very likely that the results will cause discrepancies during the measurement since the samples would continuously change and the recorded data would be distorted. The issues for ZnO thermoelectric properties measurements will be discussed in chapter 2.3.

1.3 Thesis Outline

This thesis contains eight chapters. Chapter three through seven contain the main scientific presentation of this thesis. Chapters three and four discuss the preparation conditions and thermoelectric properties of Al-doped and Al,Ga-dually-doped ZnO. Chapter five discusses the nanostructuring of Al-doped ZnO. Chapters six and seven discuss the new ZnCdO based thermoelectric oxide materials.

Chapter 2 describes the detailed experimental methods and includes the synthesis methods and characterization techniques. This chapter highlights the ZnO thermoelectric properties measurement issues, and the discrepancies caused in Seebeck coefficient and electrical conductivity measurements using different techniques and in different atmospheres.

Presented in chapter 3, the microstructure and thermoelectric properties of Al-doped ZnO using α - and γ -Al₂O₃ as dopants are systematically investigated in order to understand their different mechanisms and effects on the thermoelectric properties. The samples were prepared by the spark plasma sintering (SPS) technique from precursors calcined at various temperatures. Clear differences in microstructure and thermoelectric properties were observed between the samples doped with α - and γ -Al₂O₃. This work is a preliminary investigation on the doping mechanisms for Al-doped ZnO.

As discussed in chapter 4, Al, Ga dually-doped ZnO was prepared by SPS with different sintering temperatures. The microstructural evolution and thermoelectric properties of the samples were investigated in detail. The sintering mechanism of ZnO particles and microstructure evolutions at different sintering temperatures were investigated by the simulation of the self-Joule-heating effect of the individual particles. This work investigates the SPS sintering conditions and mechanism for Al, Ga dually-doped ZnO.

In chapter 5, nanostructuring of Al-doped ZnO was established. Using different morphologies of precursors by soft chemical routes, Al-doped ZnO nanocomposites were successfully synthesized by spark plasma sintering (SPS). The as-prepared samples exhibited different nanostructures and certain degrees of preferential orientations. Using the simple parabolic band

model and the Debye-Callaway thermal transport model, the anisotropic properties of the nanostructured samples were elucidated and the influence of the grain size and nanoprecipitates on the electron and phonon transport was analyzed and discussed in detail.

In chapter 6, the new ZnCdO based n-type thermoelectric material is introduced and its thermoelectric properties are investigated after doping with Sc, Ga, Sn, Ce etc. The electrical and thermal transport properties were both analyzed using the simple parabolic band model and Debye-Callaway thermal transport model, respectively. The Sc-doped ZnCdO showed promising thermoelectric properties with zT values surpassing those of the conventional Al-doped ZnO materials, as well as the high temperature air stability that the conventional ZnO based materials lack.

Finally, the conclusions and outlooks are presented in chapter 7.

Chapter 2 Experimental

The experimental details of the thesis are described in this chapter. The material processing methods like hydrothermal synthesis, solid-state-reaction, and spark plasma sintering are described first. The characterization methods for materials structural properties and thermoelectric properties are described in the followings. The issues for thermoelectric properties measurements for ZnO materials are discussed at last.

2.1 Material Processing

2.1.1 Power processing

Power processing includes the powder mixing and pressing procedures before sintering. This applies to all of our commercial purchased oxide powders.

Roll-mixing is an effective method for homogenizing the starting powder. The starting powder often consists of two or more than two component powders, for example ZnO, Al₂O₃, and Ga₂O₃. First, the powders were weighed to the right amount and added together into a polyethylene bottle. Zirconia cylinders or balls were also added into the bottle as a mixing aid. Then the absolute ethanol with the same weight amount to the powders was added. After that, the bottles were sealed and attached with the right safety labels. The mixing speed is 40 rpm and the time is for 24 hours. When the mixing procedure is finished, the powder is dried at room temperature in a fume hood for 48 hours.

For making nanostructured ZnO ceramics, the commercial powders couldn't meet the special requirements like particles sizes, particle morphologies, and the homogeneity of the dopants. Thus, the soft-chemical synthesis was carried out to produce nanoparticles.

One type of chemical synthesis in this work is forced-hydrolysis method. Very fine Al-doped ZnO nanoparticles could be synthesized using this method. Zinc acetylacetonate and aluminum nitrate at a molar ratio of 98:2 were dissolved in ethanol, and the solution was then refluxed. Another ethanol solution containing sodium hydroxide was added dropwise into the zinc acetylacetonate solution and the mixture was then refluxed for 1 h. After the reaction was completed, white precipitates were centrifugally washed several times with de-ionized water and ethanol. The resultant nanoparticles were then used as seeds for the synthesis of Al-doped ZnO rods and platelets, as well as starting particles for sintering.

Another type of chemical synthesis is hydrothermal method. The Al-doped ZnO particles with certain morphologies e.g. rods or platelets, could be synthesized using this method. The Al-doped ZnO rods were synthesized following this procedure: 100 mg Al-doped ZnO nanoparticle seeds were added in a 160 ml solution of 0.49 M ZnCl₂, 0.01 mM AlCl₃, (Zn/Al = 98:2) and 0.1 mM PEG20000 after adjusting the pH value to 7–8 using aqueous ammonia. The mixture was first stirred at room temperature for 1 hour and then transferred into a 200 ml Teflon liner which is a part of the hydrothermal reactor, as shown in Fig. 2.1. The Teflon liner was then sealed inside the stainless steel shell and put inside an oven at 160 °C for 20 hours. After the reaction

was complete, the formed precipitates were taken out of the liner and centrifugally washed several times with de-ionized water and ethanol, and then dried in vacuum. The Al-doped ZnO platelets were also synthesized using a similar procedure: 100 mg Al-doped ZnO nanoparticle seeds were added in a 160 ml solution of 0.49 M $\text{Zn}(\text{CH}_3\text{COO})_2 \cdot \text{H}_2\text{O}$, 0.01 M $\text{Al}(\text{NO}_3)_3$, ($\text{Zn}/\text{Al} = 98:2$), 0.1 M NaOH, and 0.17 mM sodium citrate. The mixture was first stirred at room temperature for 1 hour and then hydrothermal treated at 95 °C for 24 hours. And the following procedure is the same to that for making Al-doped ZnO rods.



Fig. 2.1 Stainless steel hydrothermal reactor and the Teflon liner.

Powder mould pressing is a very important step for ceramic processing. The final density of the sintered bulks is directly related to the quality of powder pressing. The press procedures used in this work included the uniaxial pressing and isostatic pressing. The uniaxial pressing was using stainless steel dies with an inner diameter of 20 mm. About 6 to 8 grams of powder was added into the die and a pressing force of 18 kN (~2 Tons) was applied for 60 sec. The isostatic pressing was following the uniaxial pressing. The samples were first wrapped with an ultrasonic rubber bag, and then immersed into the isostatic pressing mould filled with water. A pressing force of 450 kN (~ 50 Tons) was applied for 60 sec.

2.12 Ceramic Sintering

The sintering methods in this work included Solid-State-Reaction (SSR) method and Spark plasma sintering (SPS) method. The SSR method is using the conventional chamber furnace or tube furnace for sintering. The samples were either sintered in air or flowing nitrogen gas. The sintering profile was 1400 °C for 5 hours. The heating up and cooling down ramping rate was 300 K/h. The SPS method is a current-assisted hot pressing method. It simultaneously applies a high-intensity pulsed direct current and uni-axial pressure to the sample during the sintering process, which offers the possibility to densify the samples within a short time at a relatively lower temperature compared with conventional sintering method [62], as well as maintaining the power morphologies and realizing nanostructures[7]. For SPS method, the powder samples were

directly used and the powder pressing step could be skipped. The mixed dry powder was first loaded in to a graphite die with graphite foils as the delaminating agents. The inner diameter for the graphite die or the punch we used was 12.7 mm. The powder was first pre-pressed in graphite die under 50 MPa for 10 s before loaded into the SPS units. The SPS units of Dr Sinter 515S (Syntex Inc., Japan) was used, as shown in Fig. 2.2. During the sintering, a pulsed direct current regulated by on:off settings, each pulse lasts 3.3 ms and has a 12:2 on:off ratio. For the sintering parameters, a constant uniaxial pressure of 50 MPa was applied and the constant ramping rate of 130 K/min was used. The samples are sintered in vacuum. The sintering time and holding time could vary according to different investigation cases. Detailed information will be given in each chapter's experimental section.



Fig.2.2 The real picture of a SPS units of Dr Sinter 515S (Syntex Inc., Japan) during sintering.

2.2 Material Characterization

2.2.1 Structural characterization

X-ray diffraction analysis was performed on using a Bruker® D8 diffractometer (Bruker, Germany) with Cu-K α radiation. The phases were analyzed and identified with EVA software and the XRD refinements were performed using TOPAS software.

Microstructures of sintered bulk samples or powder samples were examined under Field Emission Gun Scanning Electron Microscopy (FEG-SEM) with Energy-dispersive X-ray Spectrometer (EDS). SEM observations and EDS elemental analysis were conducted on Zeiss® Supra systems (Carl Zeiss, Inc. Germany).

High resolution transmission electron microscopy (TEM) imaging with electron diffraction analysis was conducted in the bright-field mode using a transmission electron microscope (model JEM-3000F) operating at an acceleration voltage of 300 kV with the assistance from Dr. Wei Zhang. Elemental maps were obtained in STEM mode using EDS microanalysis.

2.22 Electrical transport properties characterization

The electrical transport properties investigated in the thesis include the electrical conductivity, Seebeck coefficient, carrier concentration, and carrier mobility. The electrical conductivity was measured using a 4-probe static DC method. The Seebeck coefficient was obtained by fitting the slope of the voltage difference dV against the temperature difference dT measured by two thermocouples. Before the measurements for electrical conductivity and Seebeck coefficient, samples were cut into about $4 \times 4 \times 12 \text{ mm}^3$ rectangular shape. Both properties were measured simultaneously using an ULVAC-RIKO ZEM-3 under a low pressure of helium atmosphere from room temperature up to 1173 K. The real picture of a sample measured in ZEM-3 and the corresponding illustrative scheme of the wire configuration are shown in Fig. 2.3.

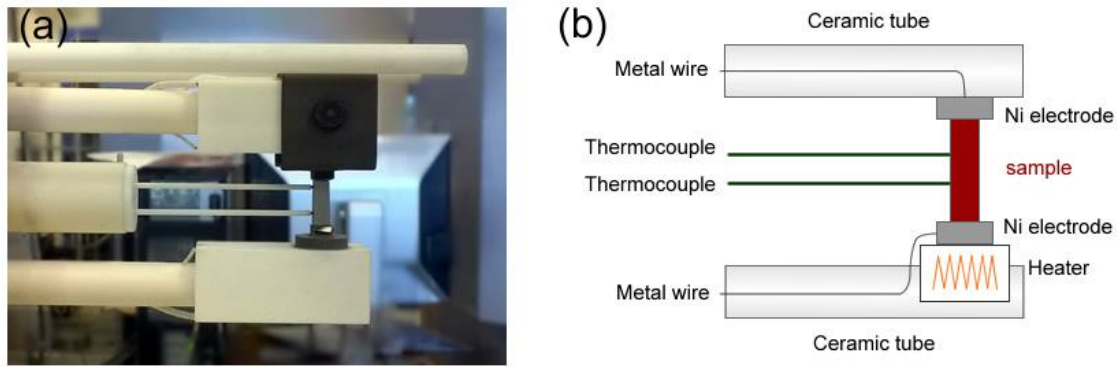


Fig.2.3 (a) the real picture of a sample measured in ULVAC-RIKO ZEM-3; (b) an illustrative scheme of the wire configuration with the sample for ULVAC-RIKO ZEM-3.

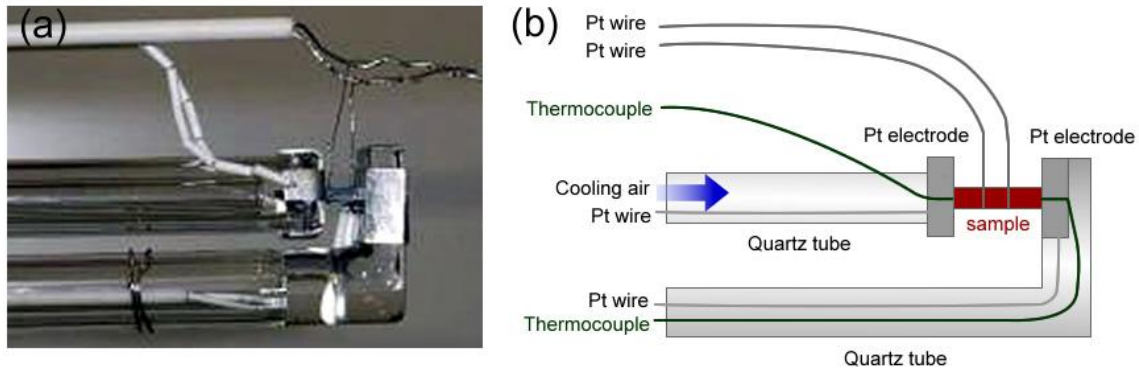


Fig.2.4 (a) the real picture of a sample measured in RZ-2001i (Figure taken from <http://www.empa.ch>); (b) an illustrative scheme of the wire configuration with the sample for RZ-2001i.

An RZ-2001i (OZAWA, Japan) from Kyushu University was used for the electrical conductivity and Seebeck coefficient measurements in air. The electrical conductivity and Seebeck coefficient were measured simultaneously as well. Unlike ZEM-3, it required no

vacuum or protective gas but directly measured samples from room temperature up to 1223 K in air. The real picture of a sample measured in RZ-2001i and the corresponding illustrative scheme of the wire configuration are shown in Fig. 2.3.

The carrier concentration and carrier mobility were obtained by Hall measurement at room temperature. Samples were cut into about $5 \times 5 \times 1 \text{ mm}^3$ squared pellets with contacts at four corners. The van der Pauw method was used with a superconducting magnet (5.08 T).

2.23 Thermal properties characterization

The thermal conductivity (κ) was determined from the thermal diffusivity (α), the mass density (ρ) and the specific heat capacity (C_p) according to the equation $\kappa = \alpha\rho C_p$. The thermal diffusivity was obtained by the laser flash method (Netzsch LFA-457, Germany), the mass densities of the samples were measured by Archimedes' method using water with surfactant, and the specific heat capacity was measured using a differential scanning calorimeter (Netzsch DSC 404C, Germany). In some cases, the specific heat capacity was calculated according to the Dulong-petit law.

2.3 Issues for ZnO thermoelectric properties measurement

As discussed in Chapter 1.2.4, the unstable thermoelectric properties of ZnO samples raised issues while measuring their electrical conductivities and Seebeck coefficients. Discrepancies will happen between different measurement techniques and in different atmospheres. This chapter will explain the reasons to the discrepancies.

Sample homogeneity is a prerequisite for accurate characterization of thermoelectric properties. However, ZnO based materials are very sensitive to the surrounding atmospheres and can form oxygen sufficient or deficient states reversibly. One can tell which state it is by simply looking at the color of the samples, where a dark greenish color mean the oxygen deficient state and the light yellowish color signifies the oxygen sufficient state. Fig.2.5 shows an example of a pellet sample losing its homogeneity due to post-annealing under different atmospheres.

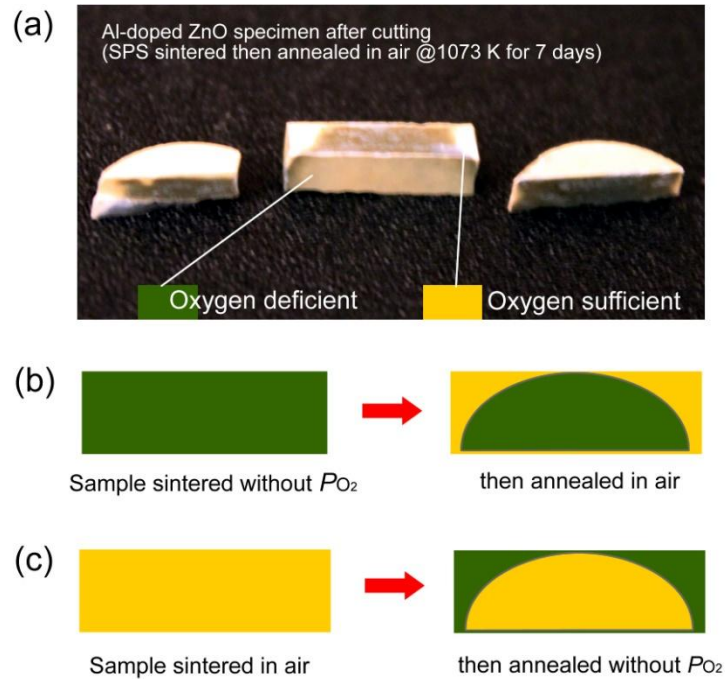


Fig. 2.5 An illustration of a pellet sample losing its homogeneity due to post-annealing under different atmospheres. (a) The real picture of a cut specimen; (b) An schematic of the specimen for (a); (c) An schematic of a reverse case—a sample first sintered in air and then post annealed without oxygen partial pressure.

As previously shown in Fig. 1.12, the dark greenish oxygen deficient parts may have a much smaller $|S|$ but with a much larger σ , while the light yellowish oxygen sufficient parts may have a large $|S|$ but very poor σ . So if the measured S and σ were not coming from a same spot of one sample, the power factor and zT will very likely to be overestimated.

Some characterization systems do not measure S and σ at exactly the same spot of a specimen, for example the RZ-2001i system. Thus special attention should be paid if the measurement atmosphere is different from the sintering atmosphere for the specimen. For the measurements in air using RZ-2001i (OZAWA, Japan) system, three different cases are illustrated in Fig. 2.6. The first case is shown in Fig.2.6a: the specimen was sintered in air, and thus there should be no changes if the measurement is running in air. The resulting power factor is correct. For the second case shown in Fig.2.6b, the specimen was sintered in N_2 or in vacuum. When the measurement is running in air at high temperature, the specimen surface would restore oxygen (get light yellowish). The volume fraction of the oxidized phase of the whole specimen is relatively larger than that at the middle part. So the calculated power factor would be overestimated from a larger $|S|$ and the similar σ , compared with the original oxygen deficient sample. For the third case shown in Fig.2.6c, the inhomogeneous specimen is measured in air. Inaccurate results would be immediately recorded even from room temperature. The

overestimation of the power factor should be very large and will be larger if the sample continues to uptake oxygen at high temperature measurements.

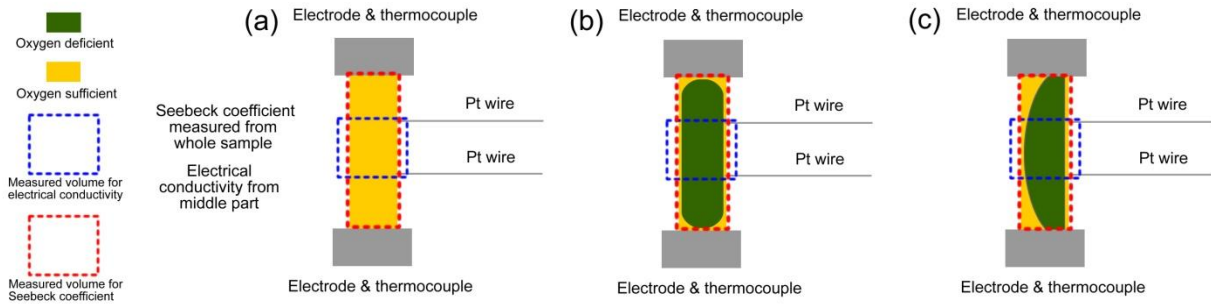


Fig.2.6. Three cases for the measurements in air using RZ-2001i (OZAWA, Japan) system: (a) measurement of an oxygen sufficient sample: the results are reliable; (b) measurement of an oxygen deficient sample at high temperature: the surface restores oxygen, the power factor is overestimated; (c) measurement of an inhomogeneous sample: the power factor is seriously overestimated.

For characterization systems like the ULVAC-RIKO ZEM-3, it measures S and σ simultaneously from the same spot of a specimen. Thus it should hold a better accuracy, even if the measurement atmosphere is different from the sintering atmosphere for the specimen. For the measurements in vacuum using ULVAC-RIKO ZEM-3 system, three different cases are illustrated in Fig. 2.7. For the first case shown in Fig. 2.7a, the specimen is oxygen deficient. The measurement results are reliable as long as the sample stays away from decomposition. The resulting power factor is correct. For the second and third cases shown in Fig. 2.7a and b, the inhomogeneous specimens are measured. The volume fraction of the oxidized/deoxidized phase at the middle part of the specimen is relatively small. So the calculated power factors are close to the values of their majority phases.

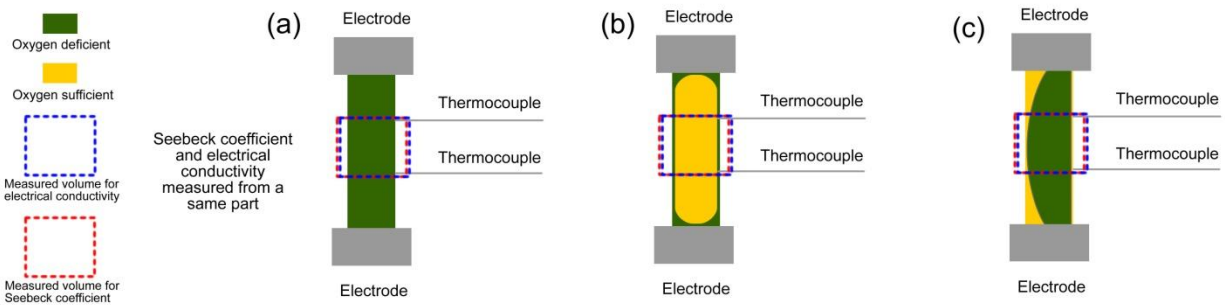


Fig.2.7. Three cases for the measurements in vacuum using ULVAC-RIKO ZEM-3 system: (a) measurement of an oxygen deficient sample, the results are reliable; (b) measurement of an oxygen sufficient sample at high temperature, the surface loses oxygen, but the power factor is close to the oxygen sufficient value; (c) measurement of an inhomogeneous sample, the power factor is close to the oxygen deficient value.

For other characterization systems that do not measure S and σ simultaneously, for example, S values are individually obtained using one apparatus while σ values are obtained using a four-probe method, the measurement of an inhomogeneous sample would result in large inaccuracies.

As shown in Fig. 2.8, the measurements of the inhomogeneous sample look very problematic. For S , the measured values are different from either the oxygen sufficient phase or the oxygen deficient phase. For σ , the measured values are close to the oxygen deficient phase for case 1 (see Fig.2.8b) and close to the oxygen sufficient phase for case 2 (see Fig.2.8c). Furthermore, if the measurements were carried out at high temperature and the sample phases continuously change during the measurements, the cases will be influenced even by the sequence of measuring S or σ first.

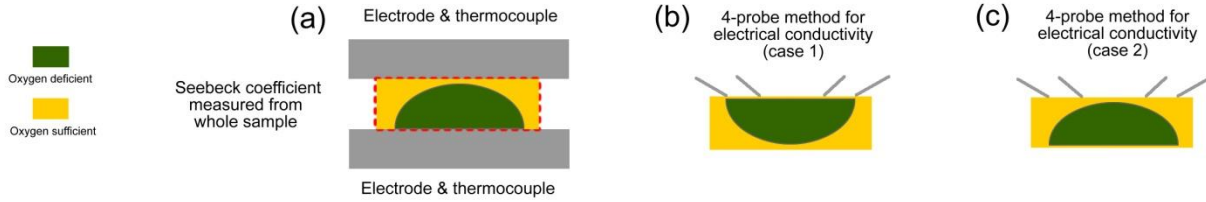


Fig.2.8. Illustrations for the measurements of inhomogeneous samples; (a) measurement of S using a two-probe method; (b) measurement of σ using a four-probe method, the σ is close to the oxygen deficient value. Using the as-measured σ will result in an overestimation of power factor; (c) measurement of σ using a four-probe method, the σ is close to the oxygen sufficient value. Using the as-measured σ will result in an underestimation of power factor.

In summary, the homogeneity of the specimen and the changing oxygen stoichiometry during the measurement are two issues for ZnO base thermoelectric characterizations. The systems that measure S and σ simultaneously from the same specimen part will be less influenced by these issues. On contrary, the systems that do not measure S and σ from the same location on the specimen or do not measure them simultaneously will result in large discrepancies for the calculated power factor and zT . Accurate results can be obtained by using homogenous specimens and avoiding dramatic changes of oxygen stoichiometry during the measurement.

Chapter 3 The Influence of α - and γ -Al₂O₃ Phases on the Thermoelectric Properties of Al-doped ZnO

Abstract:

A systematic investigation on the microstructure and thermoelectric properties of Al-doped ZnO using α - and γ -Al₂O₃ as dopants was conducted in order to understand the doping effect and its mechanism. The samples were prepared by the spark plasma sintering technique from precursors calcined at various temperatures. Clear differences in microstructure and thermoelectric properties were observed between the samples doped with α - and γ -Al₂O₃. At any given calcination temperature, γ -Al₂O₃ resulted in the formation of a larger amount of the ZnAl₂O₄ phase in the Al-doped ZnO samples. The average grain size was found to be smaller for the γ -Al₂O₃-doped samples than that for the α -Al₂O₃-doped ones under the same sintering condition. It is proposed that the ZnAl₂O₄ phase is the reason for the observed suppression of grain growth and also for the slightly reduced lattice thermal conductivity exhibited by these samples. The γ -Al₂O₃ promoted the substitution for donor impurities in ZnO, thus resulting in shrinkage of the unit cell volume and an increase in the electrical conductivity compared with the α -Al₂O₃ doped ZnO. At a calcination temperature of 1173K, the γ -Al₂O₃ doped sample showed a zT value of 0.17 at 1173 K, which is 27% higher than that of the α -Al₂O₃ doped sample.

The work discussed in this chapter is published in: L. Han, N. V. Nong, T. H. Le, T. Holgate, N. Pryds, M. Ohtaki and S. Linderoth, *J. Alloys Compd.*, 2013, **555**, 291.[56]

3.1 Introduction

Thermoelectric oxide materials are strong candidates for high temperature power generation from waste heat. The promising high temperature n-type thermoelectric properties of Al-doped ZnO were first brought to the public sight by Ohtaki et al. in 1996 [50]. Recently, a figure-of-merit, zT of 0.44 at 1000 K was obtained for nanostructured Al-doped ZnO [10], and again this showed the possibility of using ZnO for low-cost practical waste heat harvesting. In the last few years, intensive investigations have been targeted to improve the thermoelectric properties and the preparation conditions of Al-doped ZnO [59,63–65], but little attention has been paid to the choice of which phases of Al_2O_3 should be used as the dopant. This is probably one of the reasons for the controversial results reported by many research groups on the thermoelectric performance of Al-doped ZnO. Therefore, it is noteworthy to investigate systematically the influences of using different phases of Al_2O_3 as dopants on the thermoelectric properties of Al-doped ZnO. In fact, the α - and γ -phases of Al_2O_3 have different crystal structures and physical properties with their specific reaction kinetics with ZnO [66–68]. Moreover, the phase transition of Al_2O_3 is temperature dependent, suggesting that the synthesis temperature of Al-doped ZnO is crucial and can result in different material properties.

From this point of view, we have conducted a systematic investigation of the microstructure and the thermoelectric properties of Al-doped ZnO synthesized by various heat treatments using two different phases of Al_2O_3 as dopants: γ - Al_2O_3 with a defect spinel structure and α - Al_2O_3 with the corundum structure. We observed a noticeable difference in the microstructure and thermoelectric properties between α - and γ - Al_2O_3 -doped ZnO when the synthesis temperature was lower than 1273 K. The correlations between the thermoelectric properties, microstructure evolutions, and the solid state reaction kinetics of the secondary phases are discussed herein.

3.2 Experimental Procedure

The starting materials used in these investigations are: ZnO (99+% 40-100 nm APS powder, Alfa-Aesar), γ - Al_2O_3 (99.5% 45-55 nm APS Powder, Alfa-Aesar), and α - Al_2O_3 (99.5% 0.9-2.2 Micron APS Powder, Alfa-Aesar).

The synthesis of Al-doped ZnO ceramics: Aluminum oxide (γ - Al_2O_3 or α - Al_2O_3) was mixed with ZnO at a molar ratio of 1:98 (the atomic ratio of Al:Zn = 2:98) by ethanol-aided roll milling using ceramic balls for 24 h. The resulting mixtures were then dried at room temperature for 24 h followed by further drying at 403 K for 3 h. The dried powders were put into porcelain boats and calcined at various temperatures (973, 1073, 1173, and 1273 K) under N_2 for 1 h. After calcination, the powders were sieved using a 300 mesh sieve, corresponding to a mean particle size of 48 μm . The precursors were densified using optimized conditions into compact bulk pellets by spark plasma sintering (SPS) at 1173 K for 5 min in argon under a uniaxial pressure of 50 MPa. The six sintered samples are denoted as γ -973, α -1073, γ -1073, α -1173, γ -1173, α -1273 according to the phase of Al_2O_3 used and the calcination temperatures. These samples and their precursors were examined by power X-ray diffraction (XRD) on a Bruker D8 diffractometer

(Bruker, Germany) using Cu-K α radiation. The density of the samples was measured on an AccuPyc-1340 Pycnometer. A scanning electron microscope (SEM) (Supra, Carl Zeiss, Inc. Germany) equipped with an EDX spectrometer was used to observe the microstructures of the samples. The measurements of the electrical resistivity and the Seebeck coefficient were carried out on an ULVAC-RIKO ZEM-3 from room temperature up to 1173 K under a low pressure of helium atmosphere. The thermal conductivity was determined from the thermal diffusivity obtained by the laser flash method (a Netzch FLA-457) and the specific heat capacity calculated by the Dulong-Petit relation.

3.3 Results and Discussion

3.3.1 Structural properties

The relative density of the bulk sintered ZnO samples doped with α/γ -Al₂O₃ was found to be 95 \pm 3% regardless of the calcination temperature. X-ray diffraction analysis for these samples showed that most of the observed XRD peaks (see Fig. 3.1a) are assigned to those of pure ZnO phase (ICDD card PDF#36-1451). It also reveals in the inset of Fig. 3.1 that the peak at $2\theta = 36.83^\circ$ assigned to the strongest peak of ZnAl₂O₄ gahnite phase [69]. Comparing this peak over the samples, it seems as if those peaks of the α -1073 and γ -973 samples are more diffused than those of the samples with higher calcination temperature. The cell volume monotonically decreased with increasing calcination temperature for both α - and γ -Al₂O₃-doped samples (see Fig. 3.1b). The ionic radius of Al³⁺ (0.039 nm, 4-fold coordination) is smaller than that of Zn²⁺ (0.060 nm, 4-fold coordination) [70], suggesting that the decrease of the unit cell volume may originate from the substitutions of Al³⁺ at Zn-sites promoted by the elevated calcination temperature. It should also be noted that the unit cell volume was smaller for the γ -1073 and γ -1173 samples than that for the α -1073 and α -1173 samples, respectively.

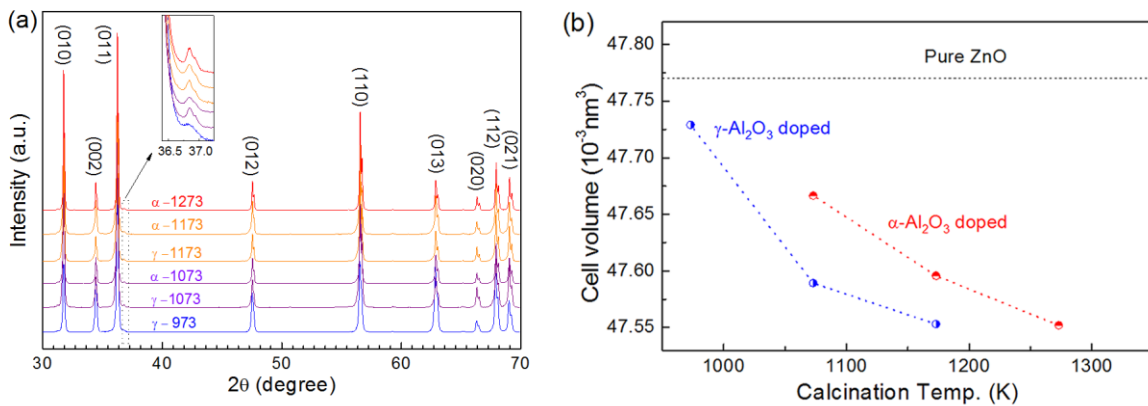


Fig. 3.1 (a) XRD patterns of α/γ -Al₂O₃-doped ZnO with different calcination temperatures (from 973 to 1273 K). The dotted box magnified as the inset shows the position of the strongest peak from ZnAl₂O₄. (b) The unit cell volume obtained from the lattice parameter refinement as a function of the calcination temperature.

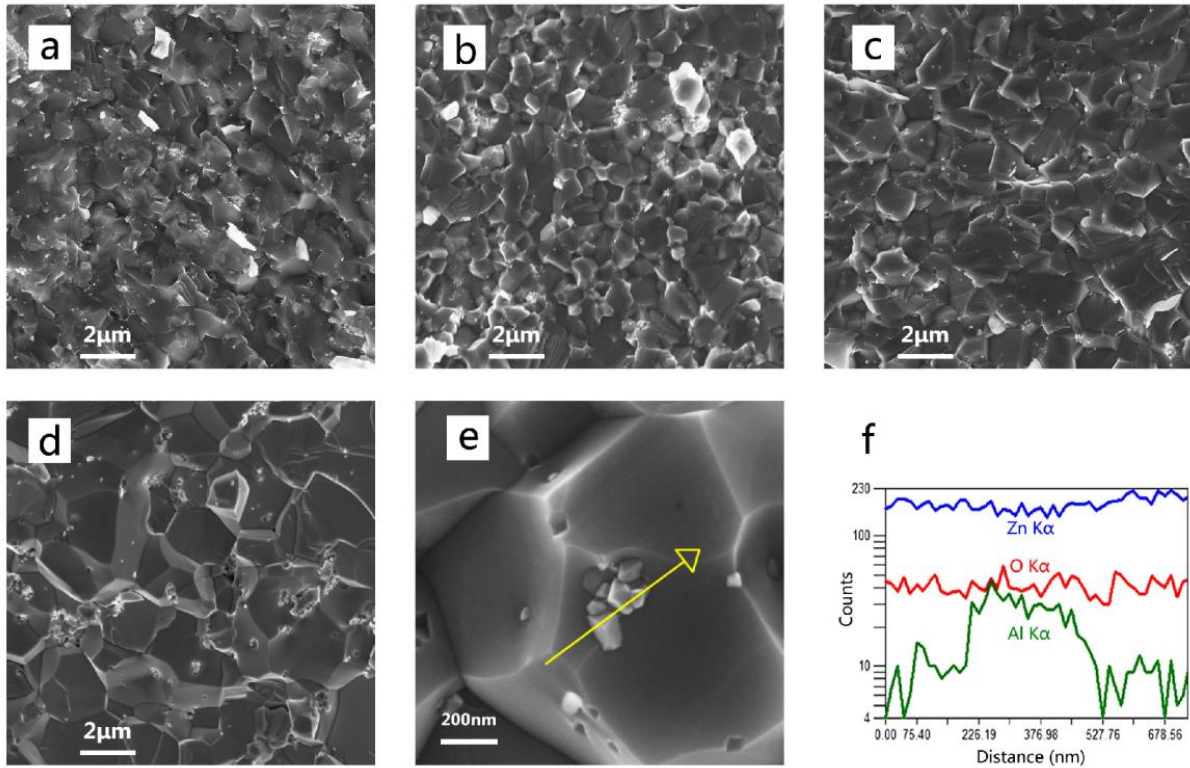


Fig. 3.2 SEM photographs of the fracture surfaces of α/γ - Al_2O_3 -doped ZnO. (a) γ -973, (b) γ -1073, (c) α -1073, (d) α -1273, (e) a representative high-magnification SEM image of the ZnAl_2O_4 nanoprecipitates. EDX line scans of Zn, O, and Al $\text{K}\alpha_1$ X-ray peaks obtained along the yellow arrow are shown in (f).

Fig. 3.2a-f shows the SEM micrographs of fracture surfaces and the EDX analysis from a selected area of α/γ - Al_2O_3 -doped ZnO samples sintered by SPS. Fig. 3.2a-e reveal that besides the ZnO grains with the size of several micrometers, there exist some interspersed nano-sized grains, which precipitate within the ZnO grain interiors or at the grain boundaries. An EDX line scan was taken across the nanoprecipitates (see Fig. 3.2e, f), showing that these nano-grains have enriched Al concentrations. This observation, together with the ZnAl_2O_4 gahnite phase detected by XRD, suggests the formation of ZnAl_2O_4 precipitates in these samples. A difference in the grain growth was also clearly observed as the calcination temperature increased. At the same calcination temperature the γ - Al_2O_3 -doped samples have smaller average grain sizes ($\sim 1\mu\text{m}$) than those of the α - Al_2O_3 -doped samples ($\sim 1.5\mu\text{m}$), as shown in Figs. 3.2b and 3.2c. This difference in grain size would be caused by the boundary pinning effect of the ZnAl_2O_4 nanoprecipitates during grain growth [71]. These results indicate that the formation rate of ZnAl_2O_4 is closely correlated to the phases of the Al_2O_3 precursors, and this will be discussed in the following section with relation to the kinetic calculation.

3.3.2 Thermoelectric properties

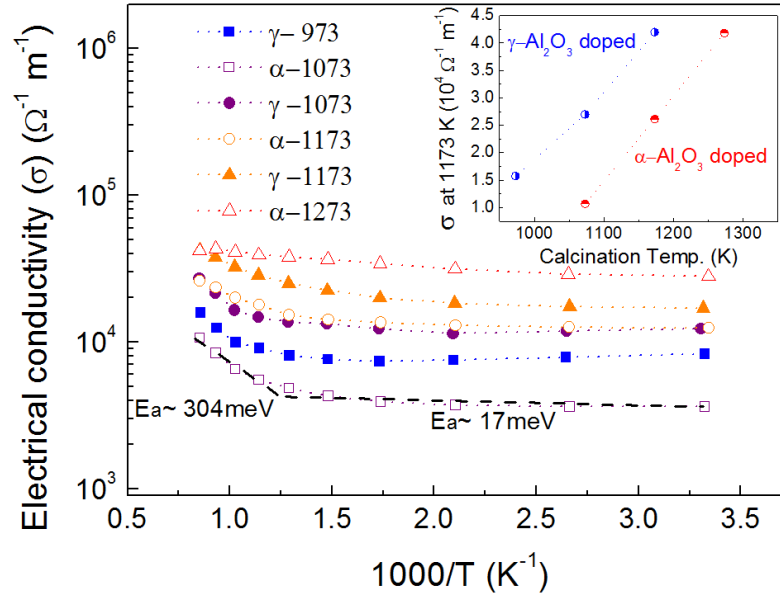
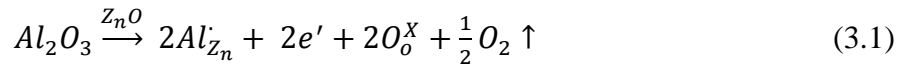


Fig. 3.3 Temperature dependence of the electrical conductivity of α/γ - Al_2O_3 -doped ZnO samples. The inset shows the electrical conductivity at 1173 K as a function of the calcination temperature.

Fig. 3.3 shows the temperature dependence of the electrical conductivity (σ) of α/γ - Al_2O_3 -doped ZnO samples. All the investigated samples showed a semiconducting behavior over the whole measured temperature range, i.e. the electrical conductivity increases with increasing temperature. The calculated activation energy for electronic conduction of the α -1073 sample changed from ~ 17 meV to ~ 304 meV at and above 770 K. With increasing calcination temperature, this change became less pronounced suggesting that more carriers are available for conduction. For both α - and γ - Al_2O_3 -doped ZnO samples, the electrical conductivity increased with increasing calcination temperature. The σ values of the γ -1073 and γ -1173 samples are notably higher than those of the α -1073 and α -1173 samples, respectively. Shown in the inset of Fig. 3.3 is the electrical conductivity, which was extracted from the data at 1173 K, as a function of the calcination temperature. It appears that the change of σ is consistent with the change of the unit cell volume (Fig. 3.1b), which could be attributed to the Al substitution at the Zn-site according to the following equation [72]:



From Eq. 3.1, one can see that the substitution of Zn^{2+} by Al^{3+} is the reason for the unit cell volume shrinkage which may result in the increase in the donor impurity concentration [73], thus providing excess charged carriers available for electrical conduction.

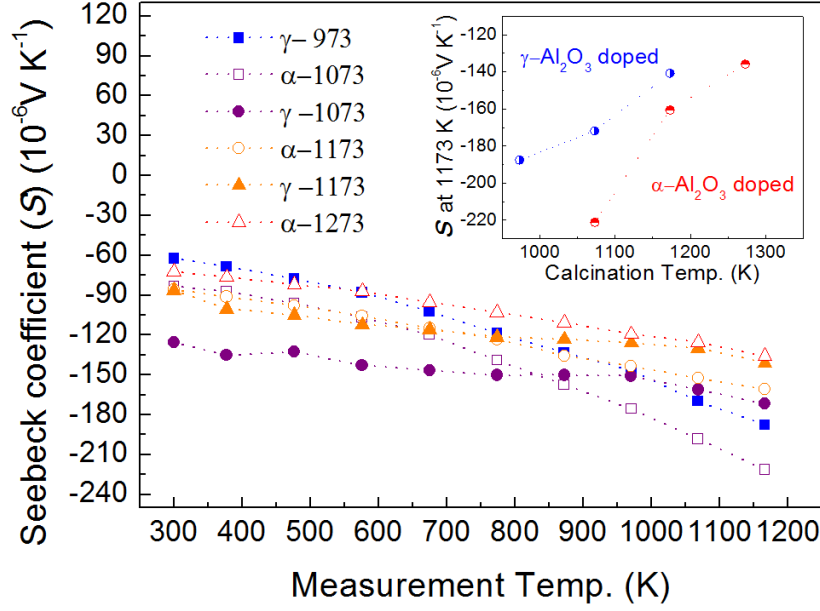


Fig. 3.4 Temperature dependence of the Seebeck coefficient of α/γ - Al_2O_3 -doped ZnO samples. The inset shows the Seebeck coefficient at 1173 K as a function of the calcination temperature.

Fig. 3.4 shows the temperature dependence of the Seebeck coefficients, S , of the α/γ - Al_2O_3 -doped samples. The S values of all the samples are negative over the whole temperature range examined, indicating n-type conduction. As shown in the inset of Fig. 3.4, at 1173 K, the α/γ - Al_2O_3 -doped samples exhibit a monotonic decrease of S with increasing calcination temperature. According to Jonker and the Pisarenko relation, a simple broad band model for extrinsic n-type semiconductors with negligible hole conduction can describe this behavior [74],

$$\sigma = ne\mu \quad (3.2)$$

$$|S| = A'Tm_d^* \left(\frac{\pi}{3n}\right)^{2/3} \quad (3.3)$$

where n is the carrier concentration, e is the electric charge of the carrier, μ is the mobility, A' is a constant, T is the absolute temperature, m_d^* is a density of the state (DOS) effective mass at the Fermi level. As the electrical conductivity (σ) and the Seebeck coefficient (S) are both a function of the carrier concentration (n), Eq. 3.2 and 3.3 clearly show that a higher n value causes an increase in σ but a decrease in $|S|$, which well explains the tendency observed in Fig.3.4. For example, the α -1273 sample with the highest electrical conductivity showed the smallest $|S|$ in the investigated temperature region.

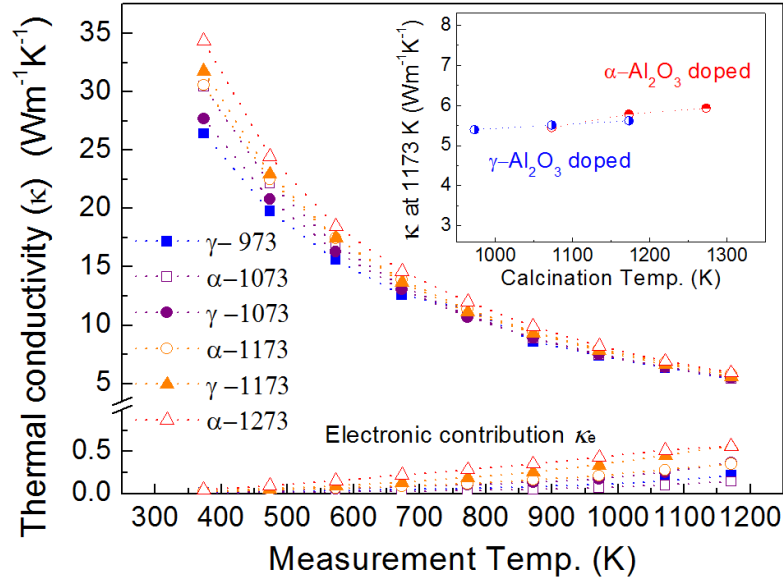


Fig. 3.5 Temperature dependence of the thermal conductivity of α/γ - Al_2O_3 -doped ZnO samples. The inset shows the thermal conductivity at 1173 K as a function of the calcination temperature.

The total thermal conductivity (κ) of the sintered samples using different α/γ - Al_2O_3 and various calcination temperatures is shown in Fig. 3.5. In general, κ rapidly decreases with increasing temperature, which is in good agreement with the result reported by Ohtaki et al [51]. It can also be seen from Fig. 3.5 that κ tends to increase with increasing calcination temperature. We estimated the electronic contribution κ_e using the Wiedemann–Franz law and found that the increase in κ with increasing calcination temperature is attributed to the increase in κ_e , particularly in the high temperature region. Although the total κ values at 1173 K as a function of the calcination temperature (see Fig. 3.5 inset) appeared to be virtually the same for both α - and γ - Al_2O_3 -doped samples, the lattice thermal conductivity, κ_L , of the samples at 1173 K was somewhat smaller for the γ -1073 and γ -1173 samples ($5.06 \text{ Wm}^{-1}\text{K}^{-1}$ and $5.15 \text{ Wm}^{-1}\text{K}^{-1}$, respectively) than those of the α -1073 α -1173 samples ($5.31 \text{ Wm}^{-1}\text{K}^{-1}$ and $5.43 \text{ Wm}^{-1}\text{K}^{-1}$, respectively). As illustrated by the microstructure in Fig. 3.2, the reason for the lower conductivity in the γ -1073 sample as compared with the α -1073 sample is probably due to the formation of disperse ZnAl_2O_4 nanoprecipitates in γ -1073 sample which might act as a phonon scattering center.

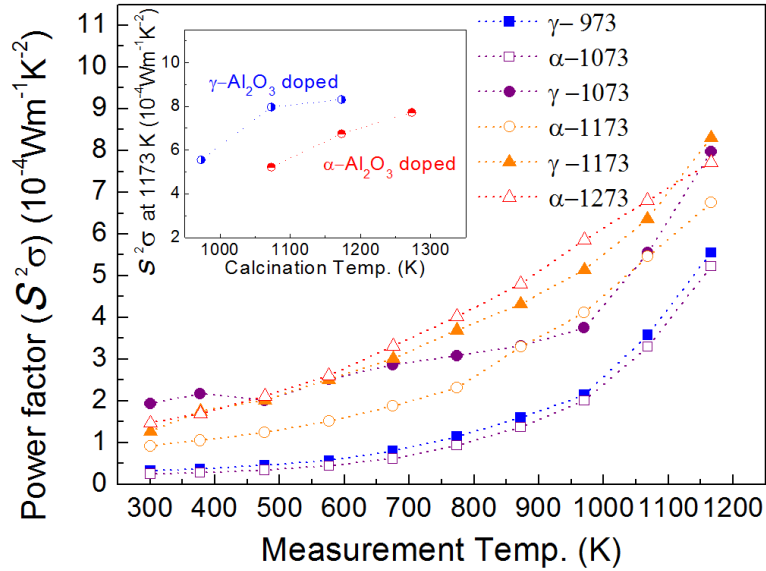


Fig. 3.6 Temperature dependence of the power factor of α/γ - Al_2O_3 -doped ZnO samples. The inset shows the power factor at 1173 K as a function of the calcination temperature.

The power factor, $S^2\sigma$, of the samples is presented in Fig. 3.6. It shows that the power factor values of γ -1073 and γ -1173 are notably higher than that of α -1073 and α -1173. Also, the power factor monotonically increases with increasing calcination temperature, as shown in the inset of Fig. 3.6. The higher power factor observed for the γ - Al_2O_3 -doped samples was mainly due to the increase in their electrical conductivity as compared to that of the α - Al_2O_3 -doped samples. At 1173K, the highest power factor of $\sim 8.31 \times 10^{-4} \text{Wm}^{-1} \text{K}^{-2}$ measured in this study is comparable to the value of $\sim 8 - 15 \times 10^{-4} \text{Wm}^{-1} \text{K}^{-2}$ reported by Ohtaki et al [50] and the value of $\sim 8.3 \times 10^{-4} \text{Wm}^{-1} \text{K}^{-2}$ reported by Jood et al [54] for Al-doped ZnO.

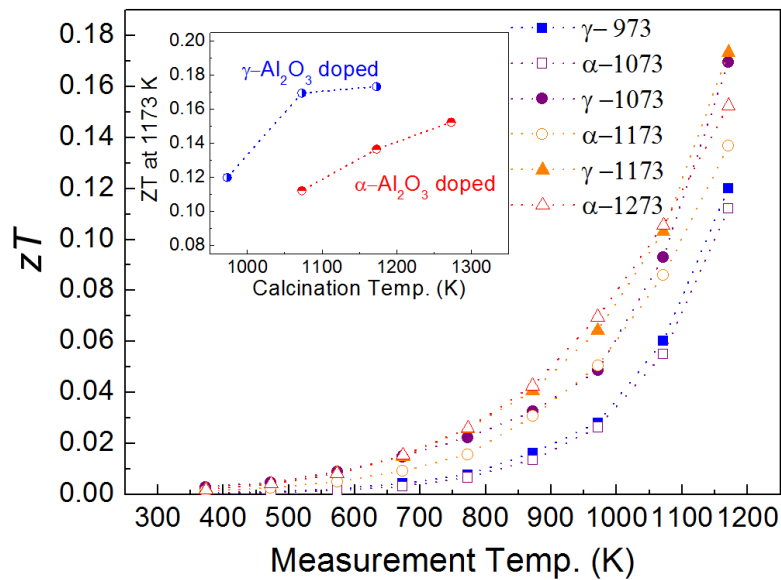


Fig. 3.7 Temperature dependence of zT of α/γ - Al_2O_3 -doped ZnO samples. The inset shows the zT values at 1173 K as a function of the calcination temperature.

The dimensionless figure of merit, zT , is given in Fig. 3.7, showing that the zT values of γ -1073 and γ -1173 are also higher than those of α -1073 and α -1173. At 1173K, the γ -1173 sample with the highest power factor attained a zT of 0.17, which is about 27% higher than that for the α - Al_2O_3 -doped counterpart at the same temperature. The highest zT value of our sample is on the same order of the one reported by Ohtaki et al [50] at the same temperature. It should be noted here that the higher zT value ($zT \sim 0.44$ at 1000 K) reported by Jood et al is mainly due to the suppression in the thermal conductivity of the sample by nanostructuring [54]. Nevertheless, our zT value is higher than the ones reported by Cai et al [72] and Tanaka et al [75] at the same temperature.

3.3.3 Theoretical analysis and discussions

According to the above results, we found that the ZnO samples doped with γ - Al_2O_3 showed a better thermoelectric performance compared to those doped with α - Al_2O_3 , when calcined at a temperature lower than 1273 K. At a calcination temperature higher than 1273 K, the difference in the thermoelectric properties gradually diminishes due to the intrinsic phase transformation of γ - Al_2O_3 to α - Al_2O_3 .

To understand these observations, we looked into the kinetics and mechanism of the reaction between ZnO and Al_2O_3 . The formation of the secondary phase, ZnAl_2O_4 , resulting from the reaction between ZnO and Al_2O_3 is well known, and can be represented as follows:



It should be noted that the formation of ZnAl_2O_4 cannot be avoided during the preparation process of Al-doped ZnO [54,64,65]. The limited solubility of Al atom into ZnO [69] could be one of the reasons. According to the thermodynamics description of the reaction (Eq. 3.4) suggested by K. T. Jacob [66], the standard Gibbs free energy change (ΔG) of the ZnAl_2O_4 formation from the reaction of α - Al_2O_3 and ZnO equals $-45.0081+0.0066T$ kJ, indicating that the formation of ZnAl_2O_4 is favored from room temperature to far above 1673 K ($\Delta G < 0$). The reaction rate is kinetically controlled by solid state diffusion [68,76].

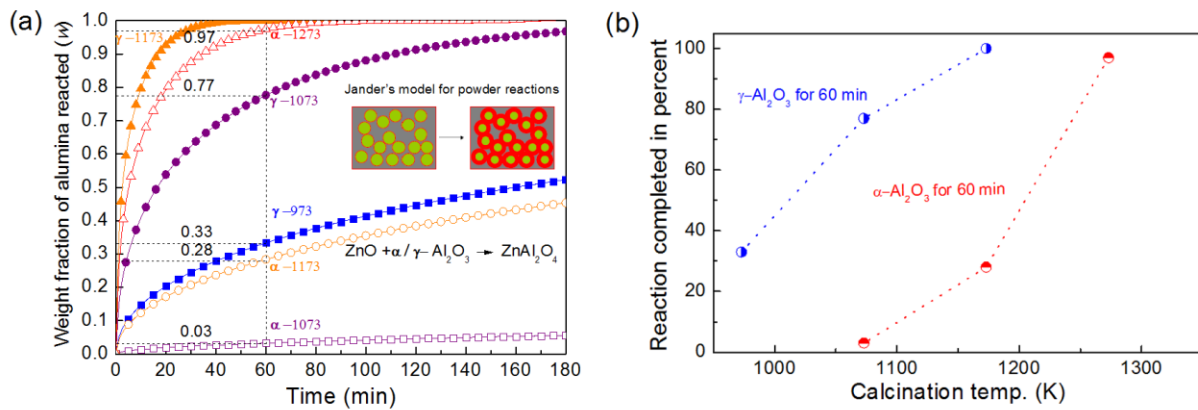


Fig. 3.8 (a) The calculated reaction time course as a weight fraction of reacted Al_2O_3 for the ZnAl_2O_4 formation. (b) The percentage of reaction completed after 1 hour as a function of the calcination temperature.

Fig. 3.8 shows the calculated reaction time course of ZnAl_2O_4 formation using Jander's model for powder reactions. According to this model, it is assumed that Al_2O_3 particles are embedded in a quasi-continuous ZnO medium. The reaction rate of the ZnAl_2O_4 formation from ZnO and Al_2O_3 is diffusion-controlled and hence follows a parabolic rate law:

$$\left[1 - (1 - W)^{\frac{1}{3}}\right]^2 = 2 \cdot k_p \cdot t / r_o^2 \quad (3.5)$$

where W is the weight fraction of the reacted Al_2O_3 , k_p is the practical parabolic rate constant, t is the reaction time and r_o is the particle size of Al_2O_3 powder. The practical parabolic rate constant k_p follows the Arrhenius law:

$$k_p = A \cdot e^{-\frac{E_a}{RT}} \quad (3.6)$$

where A is pre-exponential factor (a term which includes factors like the frequency of collisions and their orientation), E_a is the activation energy, R is the gas constant, T is temperature. By combining Eq. 3.5 and Eq. 3.6, one can obtain:

$$W = 1 - \left[1 - (2A \cdot t)^{\frac{1}{2}} \cdot e^{-\frac{E_a}{2RT}} \cdot r_o^{-1}\right]^3 \quad (3.7)$$

According to the experimental data reported by Tsuchida et al [68], the parameters of A and E_a can be obtained by Arrhenius fitting. A equals $18076 \mu\text{m}^2 \text{min}^{-1}$. E_a for $\alpha\text{-Al}_2\text{O}_3$ and $\gamma\text{-Al}_2\text{O}_3$ equals 4.9 and 2.04 eV, respectively. r_o equals the average particle size of Al_2O_3 powder. Using Eq. 3.7, the reacted Al_2O_3 fraction can be plotted as a function of time. As shown in Fig. 3.8a, the reaction rate of $\gamma\text{-Al}_2\text{O}_3$ with ZnO is significantly higher than that of $\alpha\text{-Al}_2\text{O}_3$ at the same temperature due to the lower activation energy of $\gamma\text{-Al}_2\text{O}_3$. From these data, we calculated the percentage of reaction completed after 1 hour as a function of the calcination temperature, and the results are shown in Fig. 3.8b. A clear correlation was found between the percentage of the reacted Al_2O_3 and the thermoelectric properties of these samples. The α -1073 sample with the smallest calculated percentage of the reacted Al_2O_3 showed the lowest σ values, while the α -1273 and γ -1173 samples with almost fully reacted Al_2O_3 showed relatively high σ . Accordingly, the electrical conductivities of the γ -1073/1173 samples were higher than those of the α -1073/1173 samples (Fig. 3.3). Also, the smaller grains size of the $\gamma\text{-Al}_2\text{O}_3$ -doped samples compared to that of the $\alpha\text{-Al}_2\text{O}_3$ -doped ones may be explained by a stronger boundary pinning effect during grain growth caused by a larger number of ZnAl_2O_4 nanoprecipitates. This is presumably due to the faster reaction and larger fraction of ZnAl_2O_4 formation for the $\gamma\text{-Al}_2\text{O}_3$ -doped samples.

3.3.4 Doping mechanisms of Al_2O_3 into ZnO

The detailed mechanisms of the reaction between ZnO and Al_2O_3 have already been studied by Branson [76] and Tsuchida et al [68]. Branson carried out marker transport experiments at the interfaces between ZnO , ZnAl_2O_4 and Al_2O_3 , and pointed out that the formation of ZnAl_2O_4 is a result of Zn ions diffusing into Al_2O_3 . Later, Tsuchida et al. not only showed evidence to support this result but also revealed the reason for the ZnAl_2O_4 formation speed. They pointed out that the reaction of α or $\gamma\text{-Al}_2\text{O}_3$ with ZnO resulted in different degrees of crystallinity of the product

layers, i.e. formation of $ZnAl_2O_4$ as “hereditary structure” [68]. Owing to the different degrees of crystallinity, the diffusivity of Zn ions in $ZnAl_2O_4$ can be varied. As a result, in the γ - Al_2O_3 , the formation of a defect $ZnAl_2O_4$ layer with a higher diffusivity of the Zn ions is observed. Correspondingly, α - Al_2O_3 results in a nearly perfect, defect free $ZnAl_2O_4$ structure with a lower diffusivity of the Zn ions and higher activation energy.

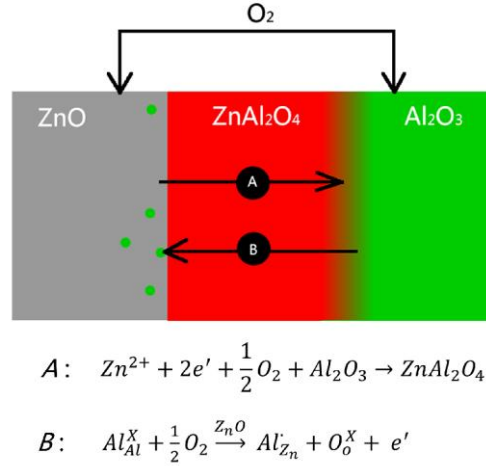
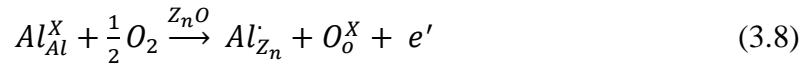


Fig. 3.9 A modified schematic diagram for the solid-state reaction process of ZnO and Al_2O_3 based on Branson’s investigation.

However, the faster formation of the $ZnAl_2O_4$ phase is not likely to be the direct reason for the increase of the electrical conductivity in the γ - Al_2O_3 -doped samples, since the $ZnAl_2O_4$ phase is reported to be unfavorable for the electrical conductivity [50]. By comparing Fig. 3.1b and 3.8b, the unit cell volume shrinkage increases along with increasing the $ZnAl_2O_4$ phase formation, indicating that the substitution of Al for Zn simultaneously occurred during the formation of the $ZnAl_2O_4$ phase, which can be represented as:



According to the previous investigations by Branson, the diffusion of Al toward ZnO does not contribute to the formation of $ZnAl_2O_4$ [76]. His explanation of the reaction between ZnO and Al_2O_3 did not take the Al diffusion into consideration. From our experimental results and investigations by other groups who observed the existence of Al diffusion into ZnO using HRTEM [77], a modified Branson’s schematic diagram of the reaction process is proposed and the details is presented in Fig. 3.9. It includes a counter-diffusion between ZnO and Al_2O_3 . The formation of $ZnAl_2O_4$ is only caused by the diffusion of Zn to Al_2O_3 , while the Al substitution for Zn results from the diffusion of Al into ZnO. The disordered structure of γ - Al_2O_3 may lead to the disordered product layers of $ZnAl_2O_4$. The Al and Zn ions would be easier to diffuse through the disordered product layer. It promotes both the formation of $ZnAl_2O_4$ and the substitutions of Al for Zn as donor impurities in ZnO, thus resulting in enhanced grain boundary pinning by

ZnAl₂O₄ and the observed higher electrical conductivity of the γ -Al₂O₃-doped ZnO than that of the α -Al₂O₃-doped counterpart.

3.4 Conclusions

In summary, we observed a close correlation between the thermoelectric properties, microstructure evolution, and the solid state reaction kinetics of the ZnAl₂O₄ formation using Jander's solid-state reaction model. At a given calcinations temperature, the addition of γ -Al₂O₃ resulted in a larger fraction of the ZnAl₂O₄ formation in the Al-doped ZnO samples, which also inhibited the grain growth and slightly reduced the lattice thermal conductivity. The higher diffusion rate of Al observed for the γ -Al₂O₃ resulted in a larger unit cell volume shrinkage and higher electrical conductivity as compared with the α -Al₂O₃-doped ZnO. As a consequence, γ -Al₂O₃-doped ZnO exhibited a higher zT than the α -Al₂O₃-doped counterpart under the same preparation conditions with calcination temperatures lower than 1273 K.

Chapter 4 The Influence of Spark Plasma Sintering Temperature on the Microstructure and the Thermoelectric Properties of Al, Ga dually-doped ZnO

Abstract:

ZnO dually-doped with Al and Ga was prepared by spark plasma sintering with different sintering temperatures. The microstructural evolution and thermoelectric properties of the samples were investigated in detail. The samples with a sintering temperature above 1223K obtained higher relative densities and higher electronic conductivity than the sample sintered at 1073K. These results were supported by solid-state-reaction completion rate which suggested that the sintering temperature above 1223K would be preferable for the complete solid state reaction of the samples. The sintering mechanism of ZnO particles and microstructure evolutions at different sintering temperatures were investigated by the simulation of the self-Joule-heating effect of the individual particles.

The work discussed in this chapter is published in: L. Han, T. H. Le, N. V. Nong, N. Pryds and S. Linderoth, *J. Electron. Mater.*, 2013, **42**, 1573. [78]

4.1 Introduction

Thermoelectric materials have received increasing attention for their wide applications such as radioisotope thermoelectric generators used for space probes or energy recovery systems from waste heat [79]. The conversion efficiency of thermoelectric modules depends on its operating temperature, with higher temperature yielding higher efficiency, as well as the materials figure of merit (zT). Thus the development of high temperature thermoelectric materials may be of considerable value in practical applications. High-temperature stable, non-toxic and low-cost zinc oxide (ZnO) is a promising candidate of n-type thermoelectric materials for such applications [10,63,65,80]. It has been reported by Ohtaki et.al [51] that dual doping of ZnO with Al and Ga resulted in a large enhancement on the $zT = 0.47$ at 1000 K and 0.65 at 1247 K for the composition of $Zn_{0.96}Al_{0.02}Ga_{0.02}O$ using conventional pressing techniques. However, the conventional sintering process such as hot pressing of doped ZnO requires a long processing time at high temperature, a process which limit one from controlling the grain size. Spark plasma sintering (SPS) is an alternative advanced sintering method. It simultaneously applies a high-intensity pulsed direct current and uni-axial pressure to the sample during the sintering process, which offers the possibility to densify the samples within a short time at a relatively lower temperature compared with conventional sintering method [62].

The present study is aimed to investigate the influence of SPS sintering temperature on the thermoelectric properties and the microstructure evolution of $Zn_{0.96}Al_{0.02}Ga_{0.02}O$, and to understand the sintering mechanism. This is done by relating the experimental observations to theoretical analysis of solid-state-reaction kinetics and temperature distribution in the particles.

4.2 Experimental Procedure

The starting materials used in these investigations are: ZnO (99.9% -200 Mesh Powder, Alfa-Aesar), $\gamma-Al_2O_3$ (99.5% 40-80 nm APS Powder, Alfa-Aesar), and Ga_2O_3 (99,99% -50 Mesh Powder, Alfa-Aesar).

The synthesis of Al, Ga co-doped ZnO ceramics ($Zn_{0.96}Al_{0.02}Ga_{0.02}O$): $\gamma-Al_2O_3$ and Ga_2O_3 were mixed with ZnO at a molar ratio of 1:1:96 (the atomic ratio of Al:Ga:Zn = 2:2:96) by ethanol-aided roll milling using ceramic balls for 24 h. The resulting mixtures were then dried at room temperature for 24 h followed by further drying at 403 K for 3 h. The dried powders were sieved using a 300 mesh, corresponding to a mean particle size of 48 μ m. The precursors were put into graphite die and sintered by spark plasma sintering (SPS). The SPS units of Dr Sinter 515S (Syntex Inc., Japan) was used, with a pulsed direct current regulated by on:off settings, each pulse lasts 3.3 ms and has a 12:2 on:off ratio. For the sintering parameters, a constant uniaxial pressure of 50 MPa, was used. The sintering temperatures were chosen to be 1073, 1173, 1223, and 1273 K. The four sintered samples are made and denoted as SPS1073K, SPS1173K, SPS1223K, and SPS1273K according to their corresponding sintering temperatures. A constant ramping rate of 130 K/min was used for all the samples. The samples are sintered in vacuum with a holding time of 8 min.

These samples were examined by power X-ray diffraction (XRD) on a Bruker D8 diffractometer (Bruker, Germany) using $\text{Cu-K}\alpha$ radiation. The densities of the samples were measured by Archimedes' method using water with surfactant. A scanning electron microscope (SEM) (Supra, Carl Zeiss, Inc. Germany) was used to observe the microstructures of the samples. The measurements of the electrical resistivity and the Seebeck coefficient were carried out on an ULVAC-RIKO ZEM-3 from room temperature up to 1173 K under a low pressure of helium. The thermal conductivity was determined from the thermal diffusivity obtained by the laser flash method (a Netzch FLA-457) and the specific heat capacity calculated by the Dulong-Petit relation.

4.3 Results and Discussion

4.3.1 Structural properties

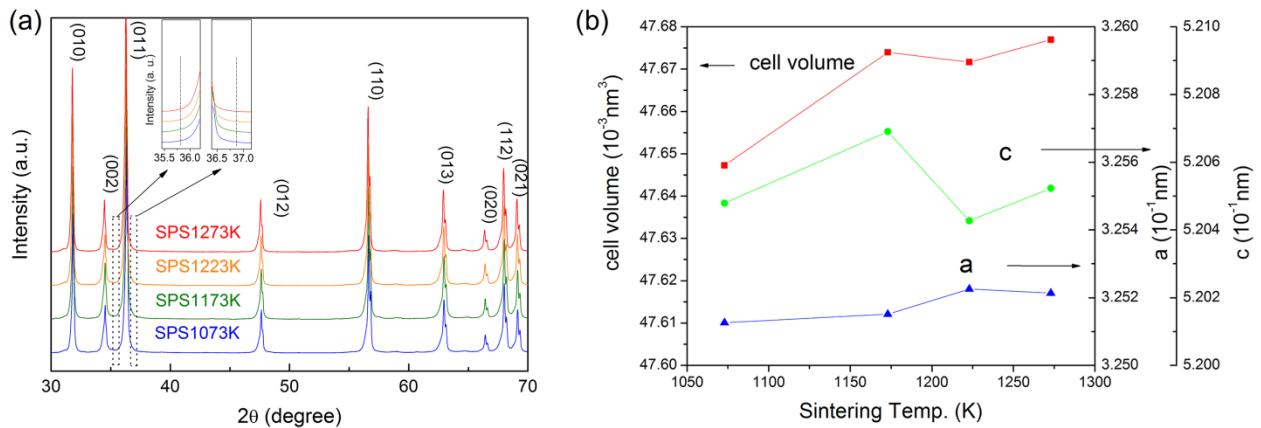


Fig. 4.1 (a) XRD patterns of $\text{Zn}_{0.96}\text{Al}_{0.02}\text{Ga}_{0.02}\text{O}$ with different sintering temperatures (from 1073 to 1273 K). The left and right dotted box magnified as the inset shows the position of the strongest peaks from ZnGa_2O_4 and ZnAl_2O_4 , respectively. (b) The lattice parameters and unit cell volume of $\text{Zn}_{0.96}\text{Al}_{0.02}\text{Ga}_{0.02}\text{O}$ samples with different sintering temperatures.

Fig. 4.1a displays the X-ray diffraction patterns of these samples sintered after SPS, showing that most of the observed XRD peaks can be identical to those of pure ZnO phase (ICDD card PDF#36-1451). The left and right inset of Fig. 4.1 magnifies the 2θ positions at 35.69° and 36.87° , where two the strongest peaks will show up if the sample contains impurity phases of the ZnGa_2O_4 and ZnAl_2O_4 , respectively. From these patterns it is clear that no peaks can be observed for either the ZnAl_2O_4 or the ZnGa_2O_4 phase. However, detailed chemical analysis using SEM-EDX (refer to Chapter 3.3) indicated that these phases may still exist and the reason for not seeing them by XRD is due to the fact that their content is below the detection limit of XRD analysis method.

Fig. 4.1b shows the refined lattice parameters and unit cell volumes of these sintered samples as a function of sintering temperature. The unit cell volumes of these samples are all smaller than that of pure ZnO ($\sim 47.77 \times 10^{-3} \text{ nm}^3$ as reported by Jood et al [10]), suggesting that the

decrease of the unit cell volume may originate from the substitutions of Al^{3+} and Ga^{3+} at Zn-sites since the ionic radius of Al^{3+} (0.039 nm, 4-fold coordination) and Ga^{3+} (0.047 nm, 4-fold coordination) are smaller than that of Zn^{2+} (0.060 nm, 4-fold coordination) [70]. It can also be observed that the unit cell volume slightly increase with the sintering temperature, which is different from our previously observed monolithic decrease of unit cell volume of Al doped ZnO [56]. This difference should be attributed to the interaction between Ga^{3+} and Al^{3+} (the Ga^{3+} is larger than Al^{3+} in ionic radius), although further investigations are needed.

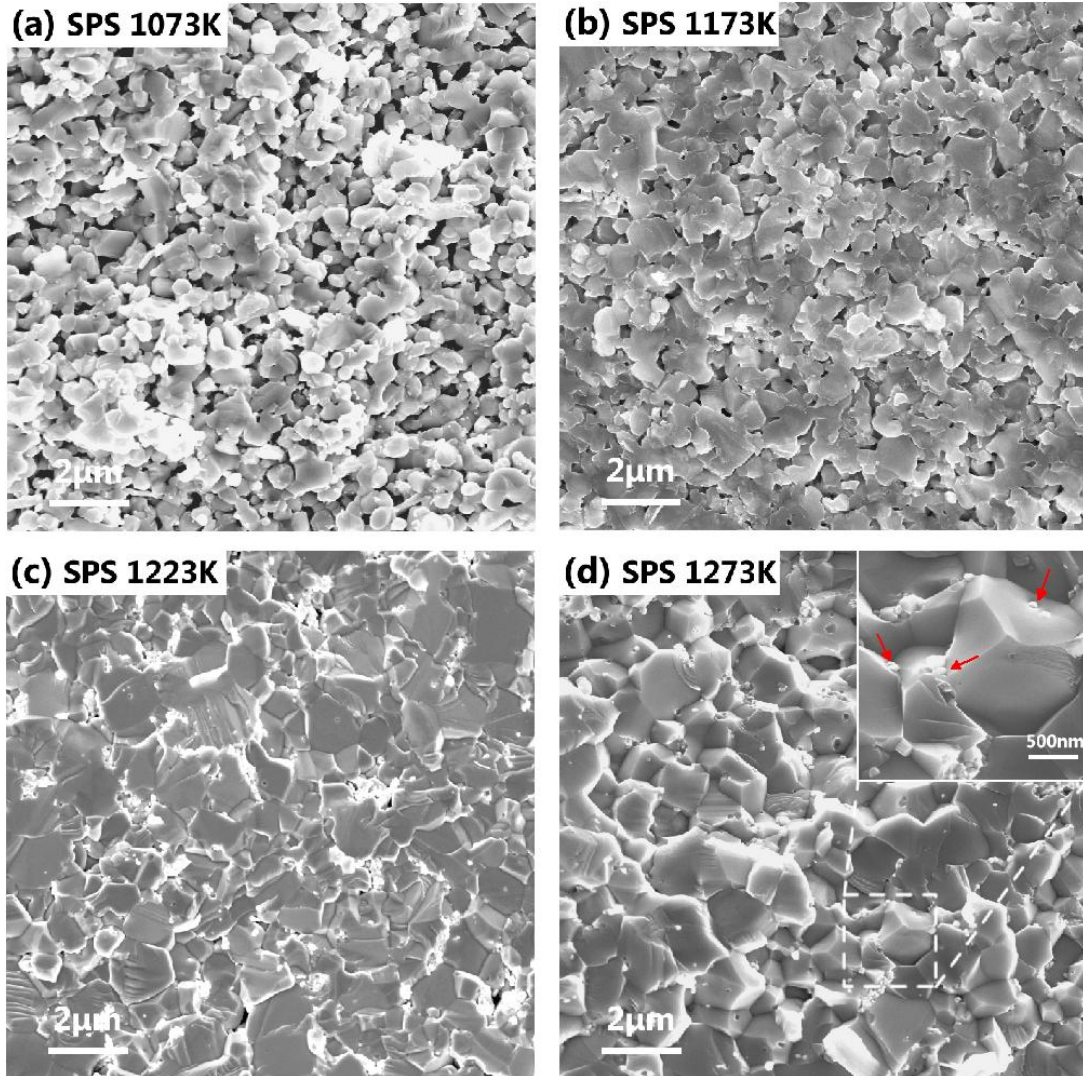


Fig. 4.2. SEM photographs of the fracture surfaces of $\text{Zn}_{0.96}\text{Al}_{0.02}\text{Ga}_{0.02}\text{O}$ with different sintering temperatures of (a) 1073K, (b) 1173K, (c) 1223K, and (d) 1273K .

Figs. 4.2a-d shows the SEM micrographs of fracture surfaces of $\text{Zn}_{0.96}\text{Al}_{0.02}\text{Ga}_{0.02}\text{O}$ samples sintered at different temperatures. The samples became denser with the increasing sintering temperature. This is consistent with the densities measured by Archimedes' method: the relative densities measured are 89.17, 93.95, 99.06 and 99.75% for the samples sintered at 1073K, 1173K, 1223K and 1273K, respectively. As clearly seen in Fig. 4.2a for the sample sintered at

1073K, the ZnO particles are partly connected to each other resulting in a relatively large amount of pores trapped in between. For the samples sintered at a temperature of 1223K and 1273K (Figs. 4.2c,d), ZnO grains with an average size of 1~2 μ m were observed. Interspersed nano-sized grains that precipitate within the ZnO grain interiors or at the grain boundaries can be seen from these fractured surfaces as shown in the inset of Fig. 4.2d.

4.3.2 Thermoelectric properties

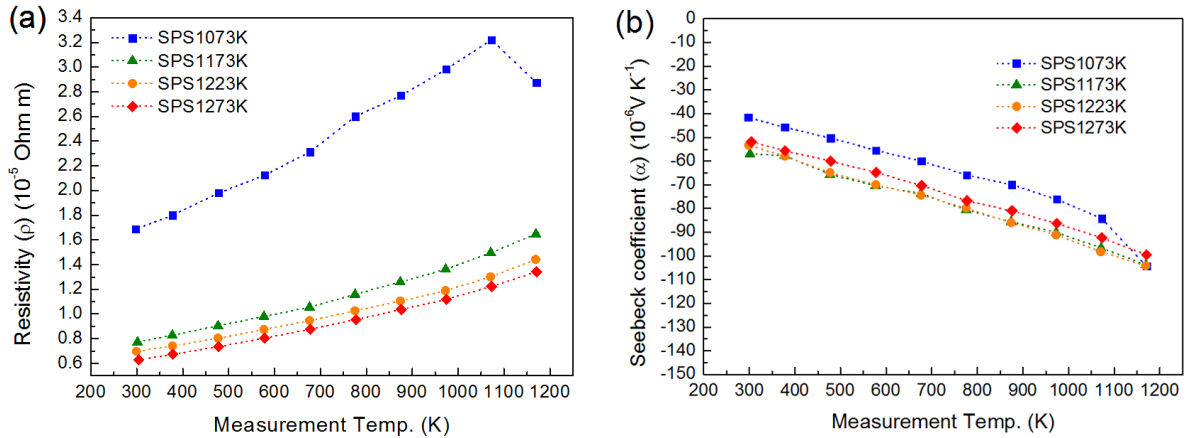


Fig. 4.3 Temperature dependence of (a) the electrical conductivity, and (b) the Seebeck coefficient of Zn_{0.96}Al_{0.02}Ga_{0.02}O samples with different sintering temperatures.

Fig. 4.3a shows the temperature dependence of the electrical resistivity (ρ) of Zn_{0.96}Al_{0.02}Ga_{0.02}O samples. All the investigated samples showed a metallic behavior over the whole measured temperature range, i.e. the resistivity increases with increasing temperature. The electrical resistivity seems to decrease with increasing sintering temperature. The decrease in ρ with increasing sintering temperature may be associated with the densities of the sintered samples. Accordingly, the SPS1073K sample with the lowest density showed the highest value of electrical resistivity, while the other samples sintered at higher temperatures resulted in higher densities and lower values of electrical resistivity. On the other hand, the decrease of electrical resistivity could be attributed to the increase in carrier concentration. During solid state reaction of Al₂O₃, Ga₂O₃ and ZnO, the increase of the sintering temperature probably results in more Al and Ga impurities which go into the ZnO structure leading to a higher carrier concentration and as a result, the electrical resistivity decreases with the increasing sintering temperature, as shown in Fig. 4.3a. This effect is not completely clear yet and further investigations to determine the carrier concentration (Hall measurements) at different sintering temperatures are the planned future work. The reaction rate of the system at various temperatures will be also treated using the Jander's model in the following section to support these observations.

Fig. 4.3b shows the temperature dependence of the Seebeck coefficients, α , of the Zn_{0.96}Al_{0.02}Ga_{0.02}O samples. The α values of all the samples are negative over the whole examined temperature range, indicating n-type conduction. The absolute values of α of SPS1073K sample are notably smaller than the other samples. This may be caused by the

incomplete densification and poor connections of the particles inside the sample as shown by the microstructure image in Fig.4.2. When the sintering temperature increased to 1173K, the sample showed the highest $|\alpha|$ values. However, with further increasing the sintering temperature the $|\alpha|$ values slightly drop. As discussed above, this may be due to the increase of carrier concentrations (n) with the increasing of sintering temperature. The increase in carrier concentration causes a decrease in electrical resistivity leading to a decrease of the seebeck coefficient, as can also be seen from the Pisarenko relation,

$$|\alpha| = A'Tm_d^* \left(\frac{\pi}{3n}\right)^{2/3} \quad (4.1)$$

where A' is a constant, T is the absolute temperature, m_d^* is the effective mass at the Fermi level.

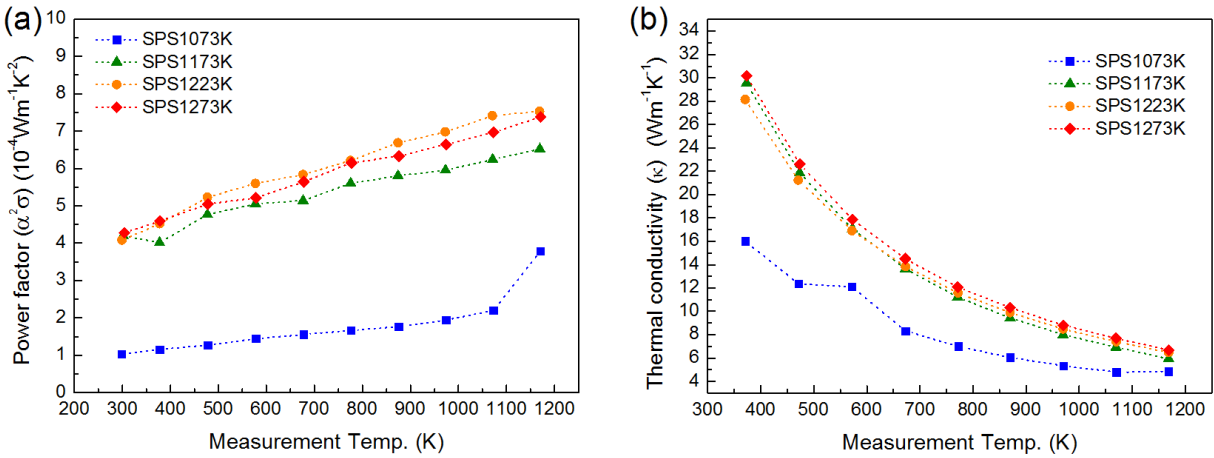


Fig. 4.4 Temperature dependence of (a) the power factor, and (b) the thermal conductivity of $\text{Zn}_{0.96}\text{Al}_{0.02}\text{Ga}_{0.02}\text{O}$ samples with different sintering temperatures.

The power factor, $S^2\sigma$, of the samples is presented in Fig. 4.4a. As reflected by the resistivity and the Seebeck measurements the power factor values of SPS1173K, SPS1223K, and SPS1273K are notably higher than that of SPS1073K. Also, the power factor values of SPS1223K are similar to that of SPS1273K.

The total thermal conductivity (κ) of the sintered samples is shown in Fig. 4.4b. In general, κ rapidly decreases with increasing temperature, which is in good agreement with the result reported by Ohtaki et al [51]. It can also be seen that the κ values increased with increasing sintering temperature. Not surprising the κ values of SPS1073K is notably lower than that of other samples. The increase in κ with increasing sintering temperature is attributed to the decrease of porosities as illustrated by the microstructure in Fig. 4.2. Comparing the thermal conductivity values we previously measured for Al-doped ZnO [56], the dual doping (Al, Ga) appears not to affect the thermal conductivity of ZnO.

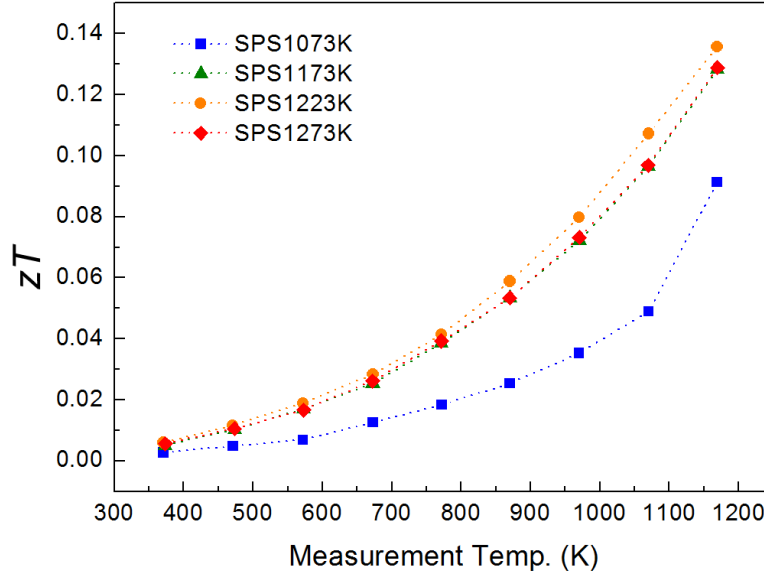


Fig. 4.5 Temperature dependence of zT of $\text{Zn}_{0.96}\text{Al}_{0.02}\text{Ga}_{0.02}\text{O}$ samples with different sintering Temperatures.

The dimensionless figure of merit, zT , is given in Fig. 4.5, showing that the zT values of the SPS1173K, SPS1223K and SPS1273K are higher than that of SPS1073K. The sample SPS1073K has the lowest zT value due to its lowest electrical properties even though it has a low thermal conductivity. The other three samples obtained the similar zT values mainly due to the trade-off relationships of thermal conductivity and electrical properties. At 1173K, the SPS1223K sample attained a zT of 0.14, which is about 35% higher than that of the SPS1073K sample at the same measurement temperature. Comparing the zT we previously obtained by Al doped ZnO ($zT = 0.17$ at 1173K), the results here are somewhat lower. This is mainly due to the decreased power factor and unaffected thermal conductivity by Al and Ga dually doping. The reason for this is still not clear. The doping mechanism of Ga and the corresponding influence on thermoelectric properties needs to be further studied.

4.3.3 Theoretical Analysis and Discussion

The different microstructures and thermoelectric properties of $\text{Zn}_{0.96}\text{Al}_{0.02}\text{Ga}_{0.02}\text{O}$ samples should be attributed to the different SPS sintering temperatures. Due to the special features of SPS, the sintering process remained a ‘black box’ from direct observation. However, modeling and calculation offered useful tools for understanding the sintering process. Using the Jander’s solid state reaction model, the reaction completion rate can be calculated [56]. The temperature distribution in ZnO particles can also be estimated using a method previously reported by Song et al [81].

4.3.3.1 The different reaction completion rate of ZnO and Al_2O_3 at various temperatures

The reaction between ZnO and Al_2O_3 is well known, and can be represented as follows:



It has been reported that the reaction progress follows Jander's solid state reaction model [68,76]. In this model, it is assumed that Al_2O_3 particles are embedded in a quasi-continuous ZnO medium. The reaction rate of ZnAl_2O_4 formed from ZnO and Al_2O_3 is diffusion-controlled and hence follows a parabolic rate law:

$$\left[1 - (1 - W)^{\frac{1}{3}}\right]^2 = 2 \cdot k_p \cdot t / r_o^2 \quad (4.3)$$

where W is the weight fraction of the reacted Al_2O_3 , k_p is the parabolic rate constant, t is the reaction time and r_o is the particle size of Al_2O_3 powder. The practical parabolic rate constant k_p follows the Arrhenius law,

$$k_p = A \cdot e^{-\frac{E_a}{RT}} \quad (4.4)$$

where A is pre-exponential factor, E_a is the activation energy, R is the gas constant, T is temperature. By combining Eq. 4.3 and Eq. 4.4, one can obtain the following equation,

$$W = 1 - \left[1 - (2A \cdot t)^{\frac{1}{2}} \cdot e^{-\frac{E_a}{2RT}} \cdot r_o^{-1}\right]^3 \quad (4.5)$$

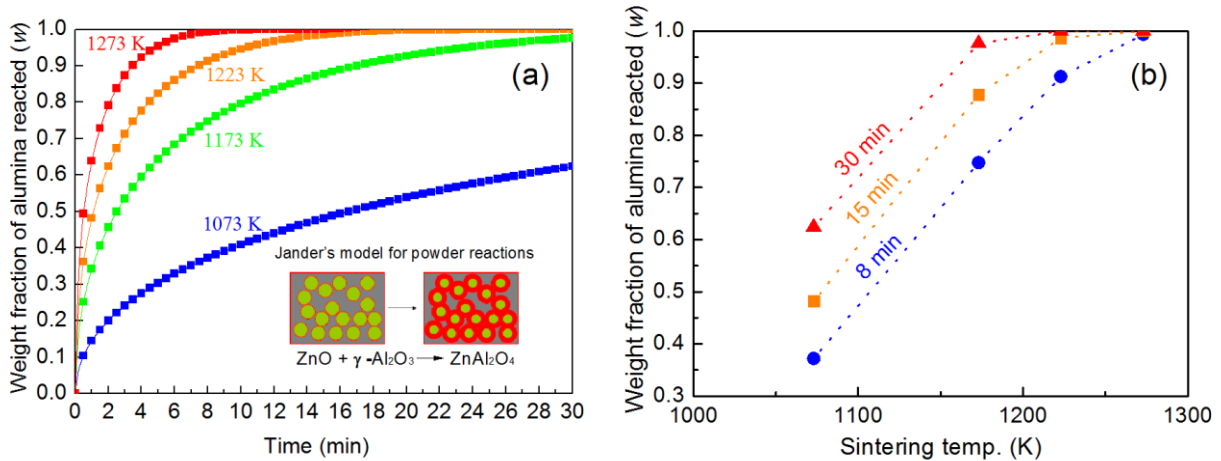


Fig.4.6 (a) The calculated reaction time course as a weight fraction of Al_2O_3 reacted with ZnO. (b) The calculated weight fraction of Al_2O_3 reacted with ZnO as a function of sintering temperature.

The parameters A and E_a were taken from Tuchida's previous experimental results on γ - Al_2O_3 with ZnO [68] which found to be, A equals $18076 \mu\text{m}^2 \text{min}^{-1}$ and E_a equals 2.04 eV respectively. r_o is the average particle size of the Al_2O_3 powder, and its value is 60nm in this study. Using Eq. 4.5, the fraction of the reacted Al_2O_3 can be plotted as a function of time, as shown in Fig. 4.6a. The reaction speed of ZnO and Al_2O_3 is correlated well with a sintering temperature, i.e. increasing reaction speed with increasing sintering temperature. At 1273 K, the reaction speed is much higher than that at 1073 K. Keeping the sintering time constant at 8 min, the sample sintered at 1273 K show nearly 100% reaction of Al_2O_3 with ZnO while the sample sintered at 1073 K has showed only 36%. It indicates that the Al_2O_3 does not fully react with ZnO in the samples sintered in a temperature lower than 1273 K within 8 min. This is consistent

with the experimental results: the resistivity decreases with an increasing sintering temperature. The substitution of Al ion with Zn ion happens along with the solid state reaction between ZnO and Al_2O_3 , it induces donor impurities which provide excess electron carriers for electronic conduction, thus reduces the resistivity. By increasing the sintering time to 15 or even 30 min, as shown in Fig.4.6b, the weight fraction of Al_2O_3 reacted at 1073K increases from 36% to 62%. Much longer time is thus needed for a complete reaction. Only the samples sintered in a temperature higher than 1173 K can reach the reaction completion within 30 min. As a conclusion, a sintering temperature above 1173 K is much preferred for the complete solid state reaction of $\text{Zn}_{0.96}\text{Al}_{0.02}\text{Ga}_{0.02}\text{O}$ by SPS. As we previously reported the sintering conditions of $\text{Zn}_{0.98}\text{Al}_{0.02}\text{O}$ [56], the thermoelectric properties were also improved by the complete solid state reaction of ZnO and $\gamma\text{-Al}_2\text{O}_3$ by calcination at 1173K for 1h.

As for the influence of Ga on the reaction kinetics, to our knowledge, the solid state reaction kinetics of ZnGa_2O_4 formation has not yet been investigated. In the near future we will carry out further investigations of ZnGa_2O_4 formation kinetics and the results will be updated accordingly.

4.3.3.2 The self-Joule-heating effect of the particles

During the sintering process using the SPS, a pulsed direct current passes through the graphite die and the sample (if the sample is electrically conductive), simultaneously generates Joule-heat. Calculating the effect of self-Joule-heating of the particles can provide insight into the sintering mechanism of ZnO particles; thereby help explaining the microstructure evolution of the samples sintered at different temperatures. The detailed derivations of the calculation can be found elsewhere [81,82].

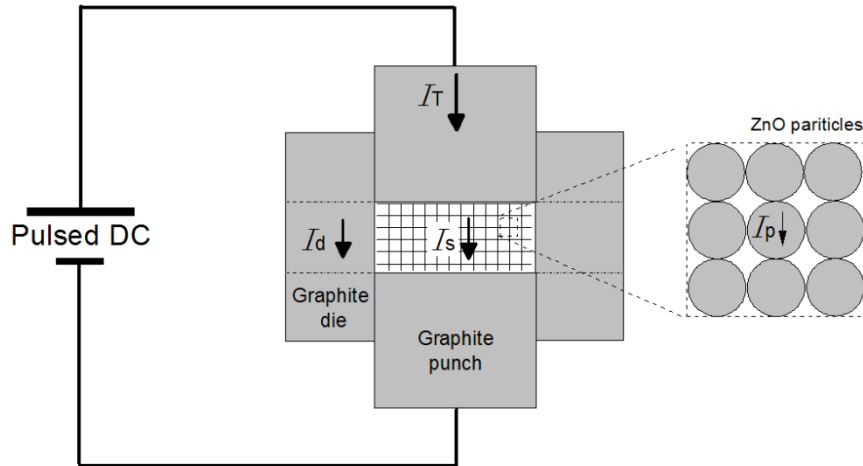


Fig. 4.7 A schematic of the sintering setups and the assumed ZnO sphere stacks.

A schematic of sintering setup of SPS are illustrated in Fig. 4.7. The total intensity of the output current during the sintering is denoted by I_T , it consists of two parts, I_d and I_s , which

passes through the graphite die and the sample respectively. Their relationship follows Eq. 4.6 due to the parallel connection of the resistances between the sample (R_s) and the die (R_d):

$$I_s = I_T \frac{1/R_s}{1/R_d + 1/R_s} = I_T \frac{\rho_d S_d}{\rho_s S_d + \rho_d S_s} \quad (4.6)$$

where S_s and S_d are the cross-sectional areas and ρ_s and ρ_d are the resistivity of the sample and the die respectively. Assuming the ZnO particles are uniformly stacked spheres with the same particle radius (r), as shown in Fig. 4.7. The local intensity of the current that passes through a single ZnO particle, I_p , can be estimated by

$$I_p = I_s \frac{4r^2}{d^2} \quad (4.7)$$

where d is the diameter of the sample. The temperature-increase (ΔT) of the particles as a function of distance from the contacting surface (“necking”) follows the equation:

$$\Delta T = \frac{16}{\pi^2} \frac{I_s^2 \rho_s \Delta t}{C_p \rho_m [r^2 - (r-x)^2]^2} \quad (4.8)$$

where Δt is the duration of the pulsed current, C_p is the specific heat capacity at constant pressure of ZnO, ρ_m is the density of ZnO, x is the distance to the contacting surface. The parameters used in this model are listed in Appendix A.

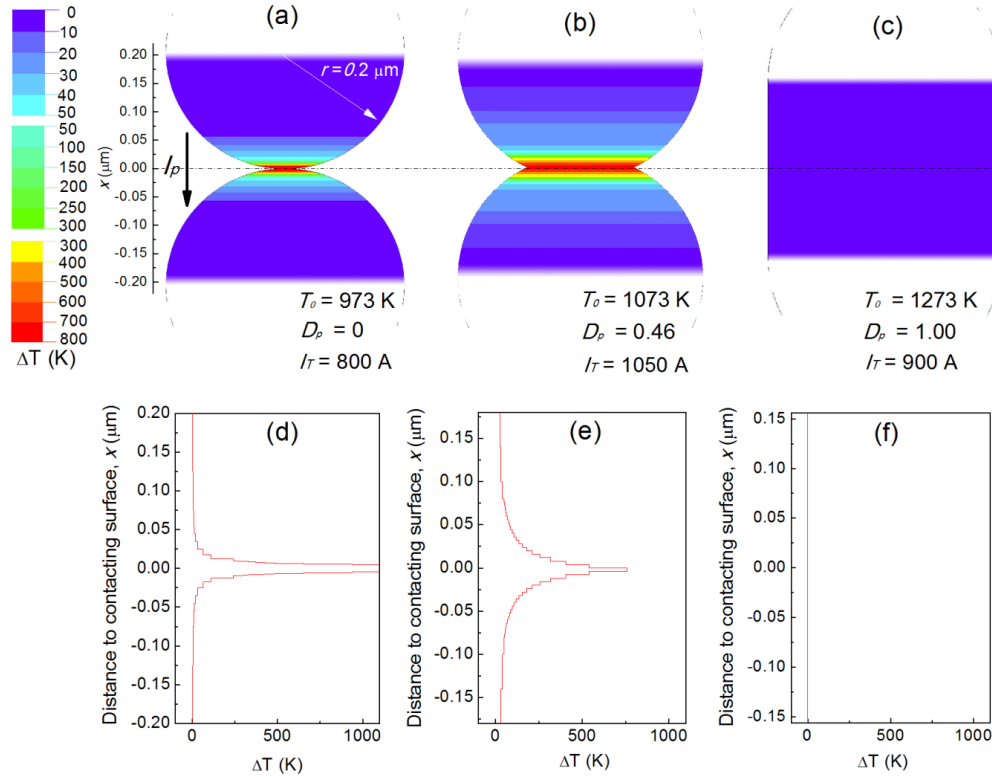


Fig. 4.8 (a, b, c) the calculated distributions of temperature-increase (ΔT) in ZnO particle (a) at the early stage of sintering, (b) half-sintered, and (c) fully sintered, T_0 is the background temperature, I_T is the total

current intensity, and D_p is the displacement percentage of the sample. (d), (e), and (f) are the corresponding plotted diagrams of (a), (b), and (c).

Based on the sintering temperature (T_o), the total current intensity (I_T), and the displacement percentage (displacement vs. maximum displacement) of the sample (D_p) extracted from the sintering profile of the sample SPS1273K, the calculated results are shown in Fig. 4.8. At the early stage of sintering, when $T_o = 973\text{K}$, $I_T = 800\text{A}$, $D_p = 0$, and the displacement is just about to start, there is a considerably high ΔT at the contacting surface of the two particles as shown in Fig. 4.8a, d. The highest ΔT which is above 1000K strongly stimulates the sintering of ZnO particles. When the sintering proceeds to $T_o = 1073\text{K}$, $I_T = 1050\text{A}$, $D_p = 0.46$, the distribution of ΔT becomes broadened due to the dissipation of heat, although ΔT at the contacting surfaces is still as high as 760K. When the sample is fully sintered at $T_o = 1273\text{K}$, $I_T = 900\text{A}$, $D_p = 1$, ΔT drops below 10K and the heat is distributed homogeneously in the sample.

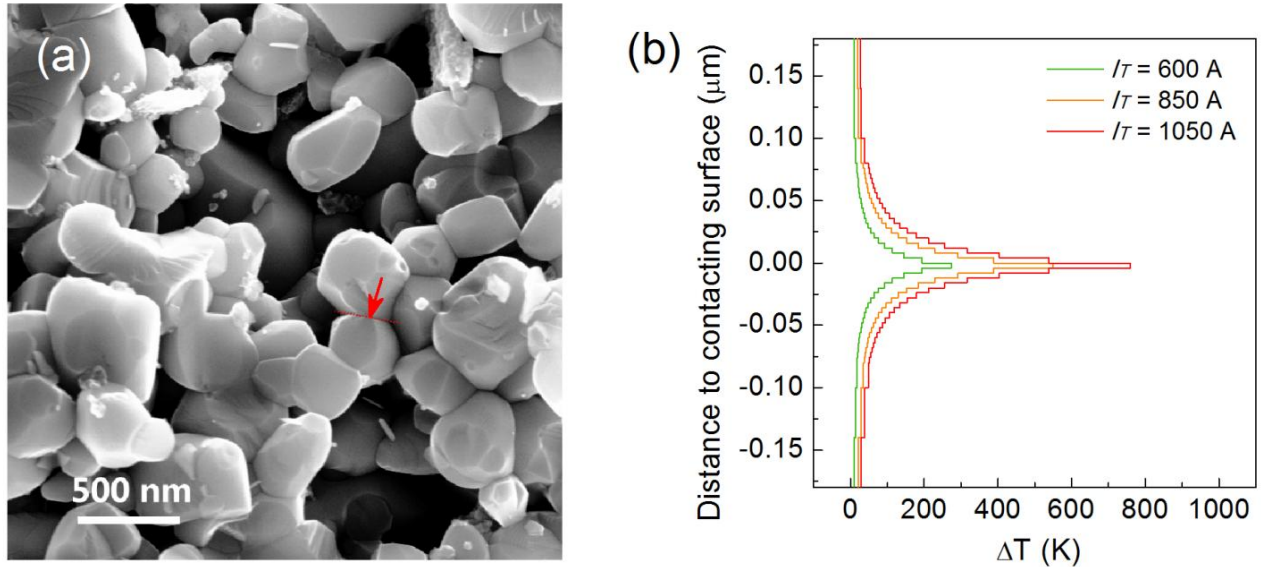


Fig. 4.9 (a) the fracture surface of the sample sintered at 1073 K with the arrow pointing at a typical contacting surface of two ZnO particles. (b) The simulated distribution of temperature increase near the contacting surface in (a) pointed by the arrow.

Fig. 4.9 shows the predicted ΔT distribution of two ZnO particles sintered at 1073K as shown in the SEM image. A typical contacting surface is chosen as shown in Fig. 4.9a. Given a sintering temperature of 1073K ($T_o = 1073\text{K}$), the ΔT distribution near the contacting surface varies with different total current intensity (I_T). The highest ΔT at the contacting surface exceeds 700K when $I_T = 1050\text{A}$, while it drops to lower than 300K when $I_T = 600\text{A}$. The input figures of I_T (600A, 850A, 1050A) are extracted from the sintering profiles (SPS1073K, SPS1173K, SPS1273K, respectively), so their corresponding local Joule-heat effect are simulated as shown in Fig. 4.9b. The simulation provides an insight to the microstructure evolution during the different sintering temperatures: For the samples sintered above 1173K, high intensity of pulsed current was applied to the sample during the sintering process and resulted in rather high ΔT

which promoted the sintering of the particles. Once the intensity of the current decreased, the solid mass diffusion would slow down rapidly due to the rapid dropping of Joule-heat generated at the contacting surface. This hindered the particles to be fully sintered within a desired time. The calculated results also suggest a possibility of manipulating the sintering process by controlling the current.

Comparing with conventional sintering method, SPS has the advantage of densifying a sample in a much shorter time with the help of the pulsed direct current through the sample. However, according to our calculation, the self-Joule heating effect became hardly pronounced after the sample already became fully densified as shown in Fig.4.8c,f. Moreover, the holding time of SPS takes only a few minutes while the holding time of e.g. hot-pressing usually takes hours for mass diffusion. Thus there could be an issue of inhomogeneity when using SPS.

4.4 Conclusion

Al, Ga dually-doped ZnO with the composition of $Zn_{0.96}Al_{0.02}Ga_{0.02}O$ was prepared by spark plasma sintering with different sintering temperatures of 1073, 1173, 1223 and 1273K. The observed microstructure of the samples sintered above 1223K showed higher relative densities compared with the sample sintered at 1073K. The sample sintered at 1073K has the lowest zT value due to its lowest electrical properties (high porosity) even though it has a low thermal conductivity. The other three samples obtained similar zT values mainly due to the trade-off relationships of the thermal conductivity and the electrical properties. The calculated results of solid-state-reaction completion rate suggested that the sintering temperature above 1223K would be preferable for the complete solid state reaction of the samples. The simulation of self-Joule-heating effect of the particles of the samples showed that, for the samples sintered at higher temperatures, the higher intensities of pulsed current applied to the sample could result in rather high temperature increase near the particles contact surfaces which strongly promoted the sintering of the particles. However, the influence of Ga doping on the thermoelectric properties of Al, Ga dually doped ZnO needs to be further studied.

Chapter 5 Effects of morphology on the thermoelectric properties of Al-doped ZnO

Abstract:

The nanoparticles of Al-doped ZnO were successfully grown into rod-like and platelet-like morphologies by soft chemical routes. These powders were consolidated using spark plasma sintering (SPS) technique. The samples consolidated from rods and platelets exhibited characteristic structures with preferential orientation while the sample consolidated from nanoparticles did not show any sign of preferential orientation. The measured zT values along the preferred orientation directions were found to be 0.16 and 0.25 at 1223 K for the samples consolidated from rods and platelets, respectively. The sample consolidated from nanoparticles exhibited fine grains and highly distributed nanoprecipitates, resulting in a zT value of 0.3 at 1223 K due to the lower thermal conductivity resulting from nanostructuring. Using the simple parabolic band model and Debye-Callaway thermal transport model, the anisotropic properties of the nanostructured samples were elucidated and the influence of the grain size and nanoprecipitates on the electron and phonon transport was analyzed and discussed in detail.

The work discussed in this chapter is published in: L. Han, N. V. Nong, W. Zhang, T. H. Le, T. Holgate, K. Tashiro, M. Ohtaki, N. Pryds and S. Linderoth, *RSC Adv.* **4**, 12353 (2014). [7]

5.1 Introduction

Thermoelectricity provides a promising opportunity for recovering electrical power from waste heat [5,22,83,84]. It improves the energy efficiency of many systems and reduces CO₂ emission. For industrial processes like those involving petroleum, steel manufacturing, transportation etc., there is an abundance of exploitable high temperature (above 500 °C) waste heat, which may be converted to usable electrical power by high temperature thermoelectric power generation. The conversion efficiency of a thermoelectric power generator is related to the dimensionless figure-of-merit (zT) of the constituent thermoelectric materials, depending on the intrinsic transport properties (i.e., the Seebeck coefficient (S), electrical conductivity (σ), and thermal conductivity (κ)) of the materials as $zT = S^2 \sigma T / \kappa$.

There are a few potential candidates for high temperature thermoelectric waste-heat recovery applications. Na doped PbTe–SrTe (4 mol%) holds the record for the highest thermoelectric zT value of 2.2 at 915 K [9], and SiGe [23,24], half-Heusler alloys [85,86], multiple-filled skutterudites [87,88] were also reported to show zT values near or surpassing 1. However, a few issues like the price, toxicity and stability in air hinders the large-scale applications of these materials. Oxide thermoelectric materials are alternatives to these materials, and their constituting elements are generally more abundant, cheaper, and less toxic. However, relatively lower zT values (usually lower than 0.7) are a challenging problem and urge further improvements [27]. The state-of-the-art p-type oxide thermoelectric materials are the layered cobaltates, such as Ca₃Co₄O_{9- δ} , which has been reported to show zT values of 0.45 at 1000 K and 0.65 at 1247 K [11,28]. For n-type oxide thermoelectric materials, the highest zT so far is 0.65 at 1247K obtained by bulk Zn_{0.96}Al_{0.02}Ga_{0.02}O [89].

ZnO is a wide direct band gap semiconductor with high electron mobility and thermal conductivity. It exhibits the most diverse and abundant configurations of nanostructures [90–94] and can be used for a wide range of applications including thermoelectrics. In technological and engineering perspectives, nanostructuring has been proven to provide an effective way to improve thermoelectric efficiency [8,16], and it has already been applied to ZnO-based materials [52–54]. Doping ZnO with Al at an optimum concentration resulted in one of the highest values of power factor among thermoelectric oxides due to its excellent charge carrier transport properties [35,95]. By introducing nanostructures using ZnO nanoparticles, Al-doped ZnO could obtain a low thermal conductivity of $\sim 2 \text{ Wm}^{-1}\text{K}^{-1}$ at room temperature and a projected $zT \sim 0.44$ at 1000 K was reported [54].

However, the complex correlations between the nanostructures and the thermoelectric properties of Al-doped ZnO were not yet fully elucidated. In order to quantitatively estimate the effect of the structural features including nanograins and nanoprecipitates on the electrical and thermal transport in a bulk Al-doped ZnO, we synthesized samples with uniform and textured grains instead of random grains by means of using spark plasma sintering in combination of starting particles with different morphologies: rods, platelets and nanoparticles. The thermoelectric properties of the samples were carefully measured and analyzed with

considerations of anisotropy. Microstructure information was used in the model analysis as well. The suppression of lattice thermal conductivity by introducing nanostructures was demonstrated and discussed using a phonon transport simulation.

5.2 Experimental Procedure

5.2.1 Preparation of samples

The Al-doped ZnO nanoparticles were synthesized by a forced-hydrolysis method. Zinc acetylacetonate and aluminum nitrate at a molar ratio of 98:2 were dissolved in ethanol, and the solution was then refluxed. Another ethanol solution containing sodium hydroxide was added dropwise into the zinc acetylacetonate solution and the mixture was then refluxed for 1 h. After the reaction was completed, white precipitates were centrifugally washed several times with de-ionized water and ethanol. The resultant nanoparticles were then used as seeds for the synthesis of Al-doped ZnO rods and platelets, as well as starting particles for sintering. The Al-doped ZnO rods were synthesized using the nanoparticles as a seed by hydrothermal method at 160 °C for 20 h in a solution of 0.49 M ZnCl₂, 0.01 mM AlCl₃, (Zn/Al = 98:2) and 0.1 mM PEG20000 after adjusting the pH value to 7–8 using aqueous ammonia. The Al-doped ZnO platelets were also synthesized using the nanoparticles as a seed by hydrothermal method at 95 °C for 24 h in a solution of 0.49 M Zn(CH₃COO)₂·H₂O, 0.01 M Al(NO₃)₃, (Zn/Al = 98:2), 0.1 M NaOH, and 0.17 mM sodium citrate. After hydrothermal process, the formed precipitates were centrifugally washed several times with de-ionized water and ethanol, and then dried in vacuum. Fig. 5.1 shows the schematic representation of formation of ZnO rods and platelets by hydrothermal synthesis. The reason why the nanoparticles were grown into rods is because in the wurtzite ZnO structure, the (001) surfaces are either Zn²⁺- or O²⁻- terminated, and during the growth process, these polarized planes attract OH⁻ or Zn²⁺ ions, whereby the crystal growth along the <001> direction occurs much faster than on the other surfaces of the crystal [96]. On the other hand, in the case of the platelets, covering the (001) surfaces by citrate ligands [97] hindered the crystal growth along the <001> direction and the growth along other directions is relatively preferred, thereby resulting in a hexagonal plate-like shape.

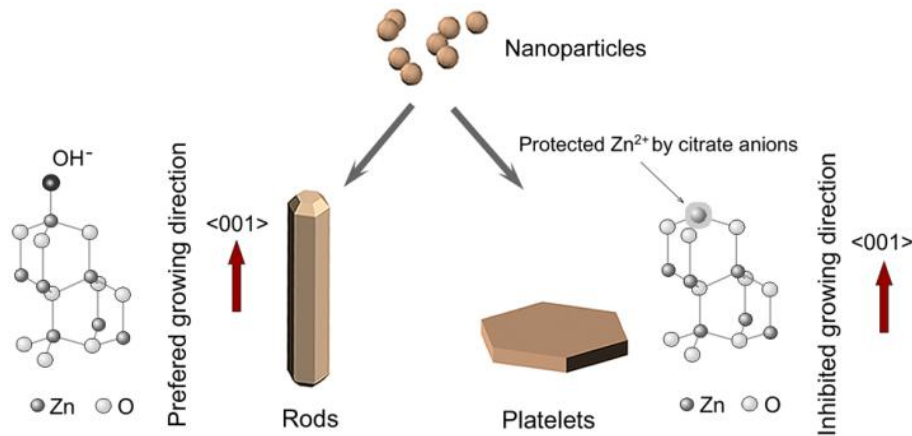


Fig. 5.1 Schematic representation of ZnO rods and platelets formation by hydrothermal synthesis.

Eight grams of each of the as-prepared Al-doped rods, platelets, and nanoparticles was individually loaded into a cylindrical graphite die of 12.7 mm in diameter, horizontally shaken for a few minutes and then pressed at an applied pressure of 50 MPa. A schematic of the preparation process is shown in Fig. 5.2. A spark plasma sintering (SPS) system of Dr Sinter 515S (Syntex Inc., Japan) was used to consolidate the samples. The following SPS parameters used were those optimized in our previous work [56,78] as follows: constant uniaxial pressure, 50 MPa; holding temperature, 1223 K; holding time, 8 min; constant ramping rate, 130 K/min. The consolidated bulk samples using the rods, platelets and nanoparticles as starting particles will be denoted as ‘Rod’, ‘Platelet’ and ‘Nanoparticle’ samples, respectively. For all the samples after SPS densification, the densities were measured as ~90% of the theoretical density.

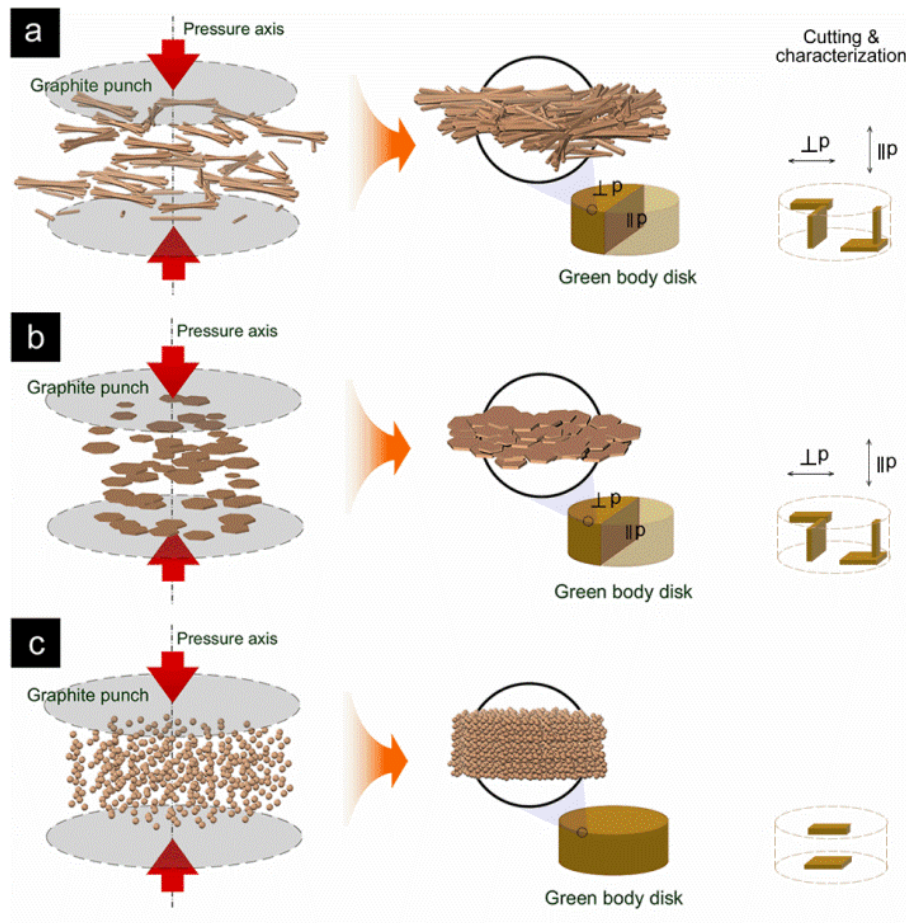


Fig. 5.2 Schematics of the consolidation process for (a) rods, (b) platelets and (c) nanoparticles, respectively. The consolidated samples of the rods and platelets were cut and characterized along both perpendicular ($\perp p$) and parallel ($\parallel p$) directions to the pressure axis. The anisotropy of the consolidated sample of the nanoparticles was negligible.

5.2.2 Measurements

Disc-shaped Rod and Platelet samples with a thickness of ~1.1 cm were cut into rectangular and square shapes, both parallel ($\parallel p$) and perpendicular ($\perp p$) to the pressure direction, as shown

in Fig. 5.2, in order to measure the electrical conductivity (σ), Seebeck coefficient (S), carrier concentration (n), and thermal conductivity (κ) along the same direction for the determination of zT in the specific directions. As for the Nanoparticle sample, the anisotropy was found to be negligible. For all the samples, the electrical conductivity and Seebeck coefficient were measured simultaneously using an RZ-2001i (OZAWA, Japan) from room temperature up to 1223 K in air. The Hall measurement was carried out at room temperature by van der Pauw method with a superconducting magnet (5.08 T). The thermal conductivity (κ) was determined from the thermal diffusivity (α), the mass density (ρ) and the specific heat capacity (C_p) according to the equation $\kappa = \alpha\rho C_p$. The thermal diffusivity was obtained by the laser flash method (Netzsch LFA-457, Germany), the mass densities of the samples were measured by Archimedes' method using water with surfactant, and the specific heat capacity was measured using a differential scanning calorimeter (Netzsch DSC 404C, Germany). The sound velocity in the samples was measured using ultrasonic sing-around method [98] on an Ultrasonic Industries Co. Ltd., UVM-2. X-ray diffraction (XRD) pattern was obtained using a Bruker D8 diffractometer (Bruker, Germany) with Cu-K α radiation. A scanning electron microscope (SEM, Supra; Carl Zeiss, Inc., Germany) was used to observe the microstructures of the samples. TEM analysis was conducted in the bright-field mode using a transmission electron microscope (model JEM-3000F) operating at an acceleration voltage of 300 kV. Elemental maps were obtained in STEM mode using EDS microanalysis.

5.3 Results and discussions

5.3.1 Structural properties

Rod samples. SEM images of the Al doped ZnO rods are shown in Fig. 5.3a. The hydrothermally grown crystals appear to have a hexagonal rod-like morphology with a preferential growth along the $\langle 001 \rangle$ axis. The rods were measured to be $\sim 25 \mu\text{m}$ in length and $\sim 4 \mu\text{m}$ in width. Transmission electron microscopy (TEM) and selected-area electron-diffraction of the rods (see Fig. 5.3b and c) indicate that each 'rod' is single crystalline in the wurtzite structure, as confirmed also by powder X-ray diffraction of the rods (see Fig. S1 in Appendix B). Fig. 5.3d and 5.3e show the fracture surface of the consolidated bulk sample. The surface perpendicular to the pressure axis (denoted as Rod ($\perp p$)) consists of rod-shaped ZnO grains with an average size of $\sim 10 \mu\text{m}$ in length and $\sim 4 \mu\text{m}$ in width (see Fig. 5.3d). Some fine particles with sizes varying from 100 nm to 300 nm were observed to precipitate mostly along the grain boundaries as shown in the inset of Fig 5.3d,e). EDX analysis shows that the precipitates are enriched in Al (see Fig. S3 in Appendix B). The precipitates were either formed during the hydrothermal treatment or during sintering as a byproduct of the reaction between ZnO and Al $_2$ O $_3$ as previously discussed in our earlier work [56]. Similar precipitates were also observed and identified as ZnAl $_2$ O $_4$ gahnite phase using TEM by Nam et al [53]. The fracture surface parallel to the pressure axis (denoted as Rod ($\parallel p$)) consists of fine grains of $\sim 4 \mu\text{m}$ in size, which is similar to the

width of the rods. It is also shown in the inset of Fig. 5.3d and e that the size and distribution of the precipitates are similar regardless of the directions of the fracture surfaces.

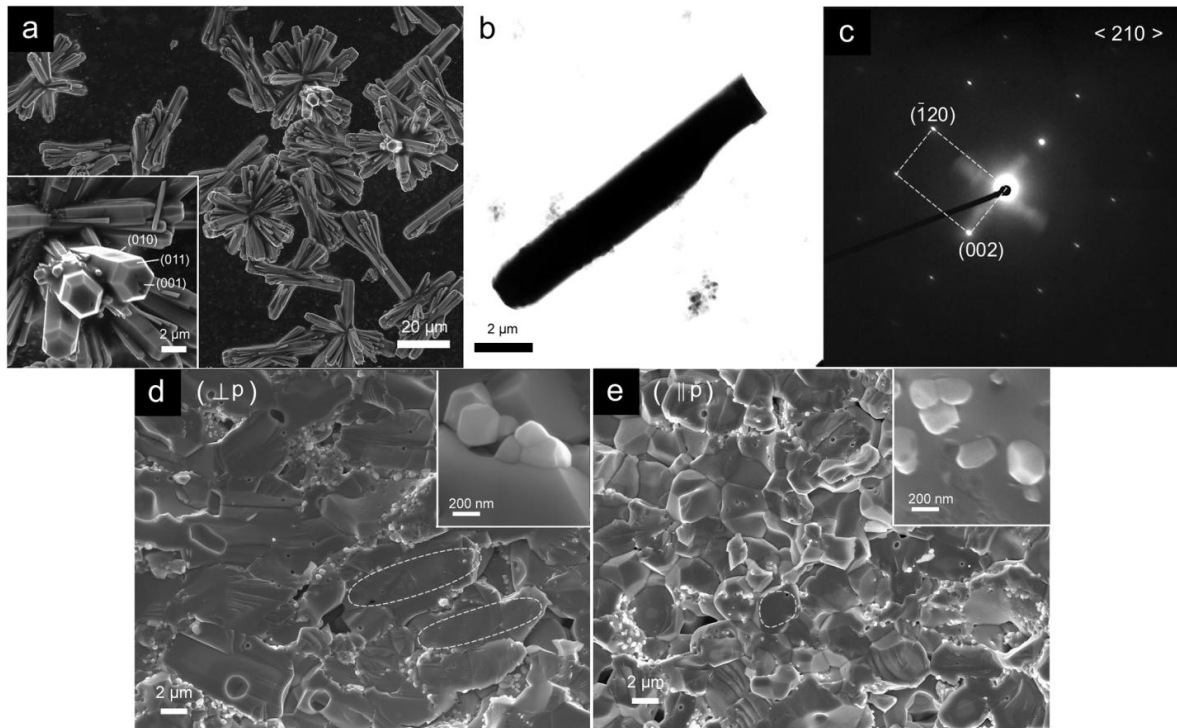


Fig. 5.3 (a) SEM images of hydrothermally grown Al-doped ZnO rods. (b) TEM image of a single rod and (c) its electron diffraction pattern along the $\langle 210 \rangle$ direction, indicating the wurtzite structure. SEM images of the fracture surfaces of the Rod sample (d) perpendicular ($\perp p$) and (e) parallel ($\parallel p$) to the pressure axis.

Platelet samples. Hexagonally shaped platelets were synthesized with an average diameter and thickness of 800 nm and 100 nm, respectively, as shown in Fig. 5.4a. A TEM image and selected-area electron diffraction of a single platelet indicates the existence of a single crystal with a wurtzite structure (see Fig. 5.4b and c). Fig. 5.4d and e show the fracture surface of the bulk sample consolidated from Al doped ZnO platelets. The fracture surface perpendicular to the pressure axis (denoted as Platelet ($\perp p$)) consists of uniform grains with similar sizes as those seen in Fig. 5.4a. Nanosized precipitates and nano voids with an average size of 30 nm can be seen in the insets of Fig. 5.4d and e. The surface parallel to the pressure axis (denoted as Platelet ($\parallel p$)) reveals a laminated structure as a result of compressing the ZnO platelets, indicating the preferential orientation of the grains (see Fig. 5.4e).

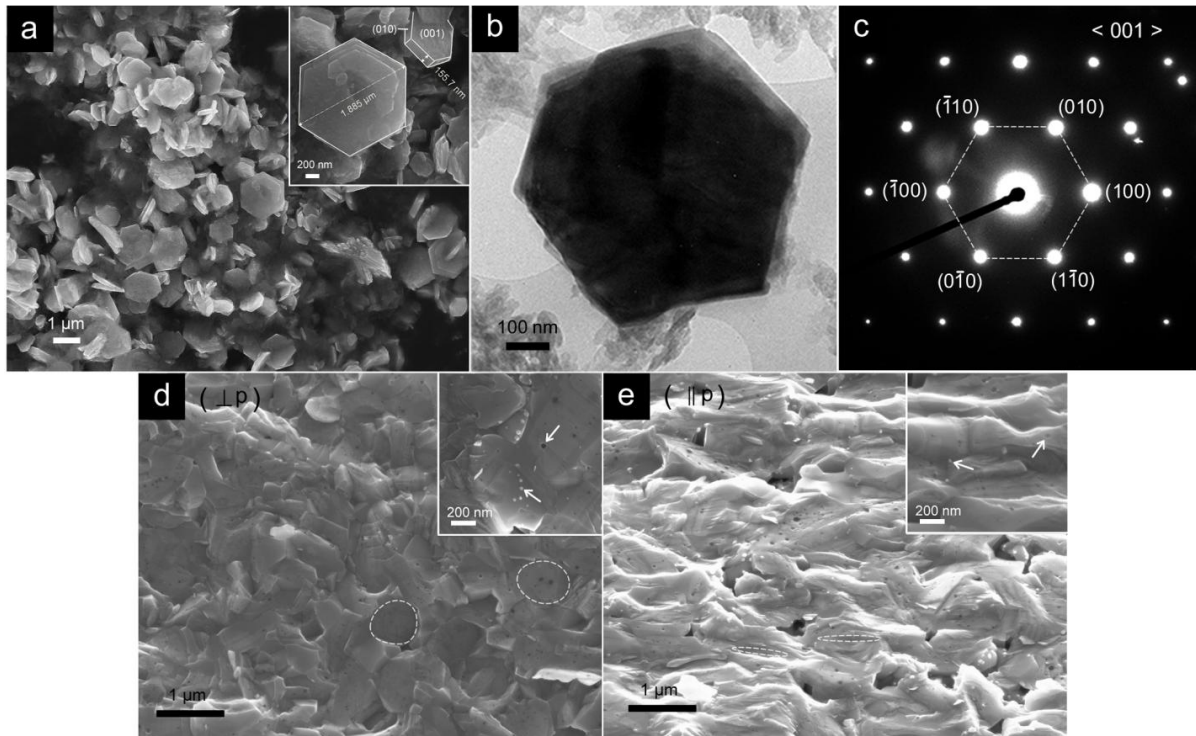


Fig. 5.4 (a) SEM images of hydrothermally grown Al doped ZnO platelets. (b) A TEM image of a single platelet and (c) its electron diffraction pattern along the $\langle 001 \rangle$ direction, indicating the wurtzite structure. SEM images of the fracture surfaces of the Platelet sample (d) perpendicular ($\perp p$) and (e) parallel ($\parallel p$) to the pressure axis.

Nanoparticle samples. Fig. 5.5a shows the HRTEM image of the Al doped ZnO nanoparticles. It reveals that each nanoparticle is a single crystal in the wurtzite structure, which is also consistent with the powder X-ray diffraction data, as shown in Fig. S1 in Appendix B. The average particle size is estimated to be ~ 8 nm by using XRD Rietveld refinement and it is consistent with the TEM observation (see Fig. 5.5b). The EDX mapping by STEM reveals the existence of Al-containing nanoparticles (see Fig. S2b in Appendix B). The as-prepared ZnO nanoparticles in the present study are similar in sized to that of Meulenkamp's work [99], which are much smaller than those fabricated by Jood et al [54] and Nam et al [53]. Fig. 5.5d and e show the fractured surface of the bulk sample consolidated from Al-doped ZnO nanoparticles (denoted as Nanoparticle). Besides the ZnO grains with the size of several hundred nanometers, there exist highly distributed nano precipitates with sizes from 10 to 15 nm, both within the ZnO grain interiors or along the grain boundaries. Compared with other Al-doped ZnO nanocomposites synthesized by Jood et al and Nam et al, the nanoprecipitates shown in this work is 10 to 20 times smaller in size [53,54], presumably due to the much smaller precursors in combination with a short densification time of SPS used in this work.

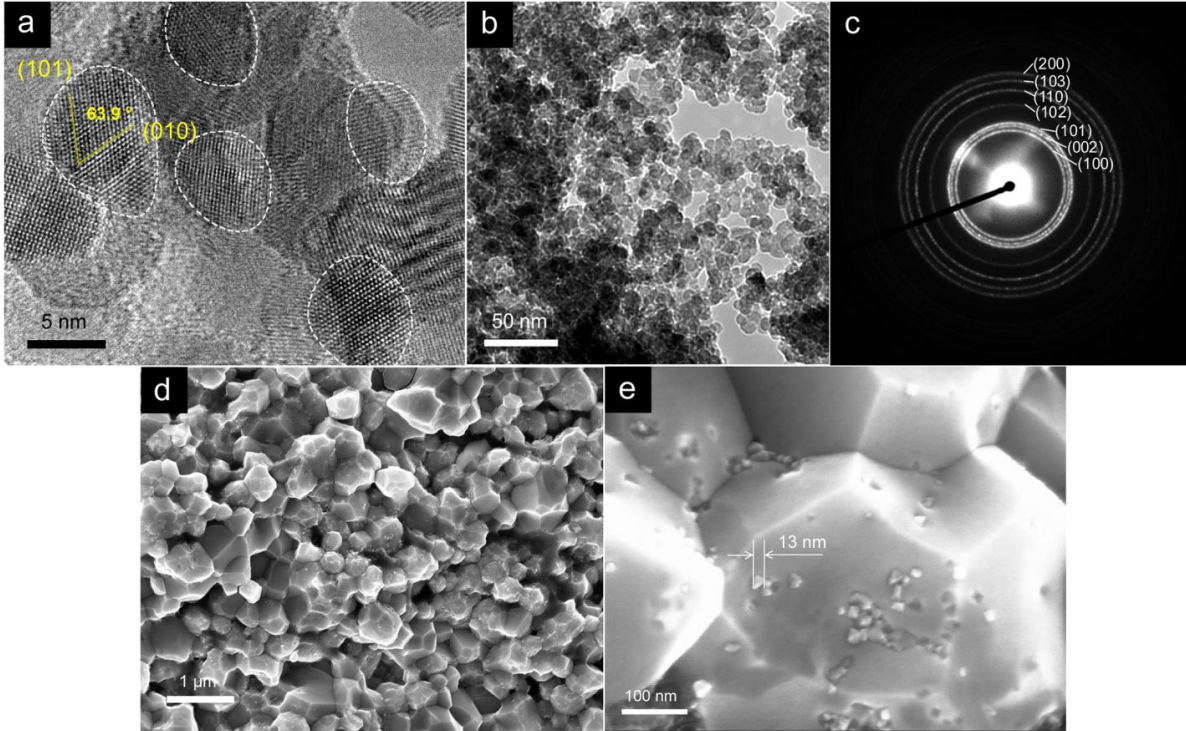


Fig. 5.5 (a) An HRTEM image of Al-doped ZnO nanoparticles. (b) A TEM image of the nanoparticles and (c) its selected-area electron diffraction pattern. (d) An SEM image of a bulk consolidated fracture surface of the Nanoparticle sample consolidated from nanoparticles. (e) A high magnification SEM image of the Nanoparticle sample showing highly dispersed nanoprecipitates within the ZnO nanograins.

X-ray diffraction patterns of the consolidated samples are shown in Fig. 5.6. All observed XRD peaks can be assigned to those of pure ZnO phase (ICDD card PDF#36-1451), though the relative intensity of some peaks may vary due to the preferred orientation. For example, the intensity ratio of the (002)/(100) peaks in Rod (\perp p) was $\ll 1$, while that of Platelet (\perp p) was $\gg 1$. To evaluate the degree of orientation of the samples, the volume fraction of a-axis-oriented grains, $\alpha_{(100)}$, and that of c-axis-oriented grains, $\alpha_{(001)}$, in the samples were calculated using the following equations [100]:

$$\alpha_{(100)} = \frac{\sum(I_{n00}/I_{n00}^*)}{\sum(I_{hkl}/I_{hkl}^*)} \quad (5.1)$$

$$\alpha_{(001)} = \frac{\sum(I_{00n}/I_{00n}^*)}{\sum(I_{hkl}/I_{hkl}^*)} \quad (5.2)$$

where I_{hkl} is measured intensity of the (hkl) peak and I_{hkl}^* is the intensity of the randomly oriented powders. The results of the degrees of orientation are shown in the inset of Figure 5.6. The Rod (\parallel p) and Platelet (\perp p) have higher degrees of (001) grains orientation. The degrees of (100) grains orientation are higher for the Rod (\perp p) and the Platelet (\parallel p) samples. The Nanoparticle sample consolidated from ZnO nanoparticles shows negligible anisotropy in this analysis as expected. It also reveals that the preferred orientation of the Platelet sample is stronger than the Rod sample. The results showed in the inset of Fig. 5.6 are consistent with the SEM observation.

The lattice parameters were from the Rietveld refinement of the XRD patterns. The results of unit cell volume are plotted in the inset in Fig. 5.6. The decrease of the unit cell volume is probably due to the substitutions of Al^{3+} at the Zn site, as the ionic radius of Al^{3+} (0.039 nm, 4-fold coordination) is much smaller than that of Zn^{2+} (0.060 nm, 4-fold coordination) [70]. The smaller unit cell volume of the Rod sample suggests a possibility of a larger substitution fraction. A direct consequence of a larger substitution fraction is a higher carrier concentration, which will be discussed in the following section.

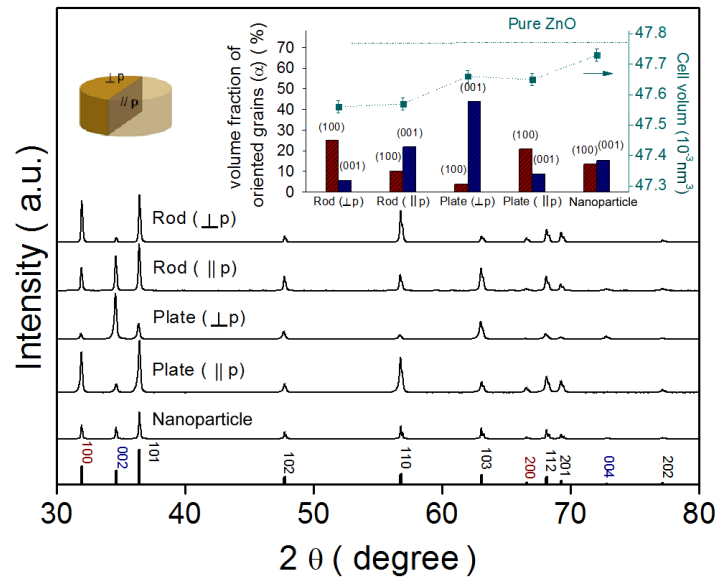


Fig. 5.6 X-ray diffraction patterns of the samples. The inset shows the degrees of orientation and the unit cell volume. The red and blue columns indicate the degrees of (100) orientation and (001) orientation, respectively.

5.3.2 Thermoelectric properties

The electrical conductivity (σ) of the consolidated samples is shown in Fig. 5.7. The Rod and Platelet samples showed a metallic conduction behavior. The electrical conductivity measured along different directions varied due to the preferred orientation of the Rod and Platelet samples. Both samples showed a higher σ along the $\langle \perp p \rangle$ direction, by a factor of 1.7 and 2.5 for Rod and Platelet samples, respectively, than along the $\langle \parallel p \rangle$ direction. The Rod ($\perp p$) sample showed a high conductivity of 6409 S cm^{-1} at room temperature, higher than any other σ values reported from Al-doped ZnO [52,53,56,95]. The Nanoparticle sample showed a semiconductor-like electrical conductivity. The σ value increased with increasing temperature due to the thermal excitation of shallow donors at $\sim 45.6 \text{ meV}$ below the conduction band-edge, as derived from the activation energy of the electrical conductivity.[54]

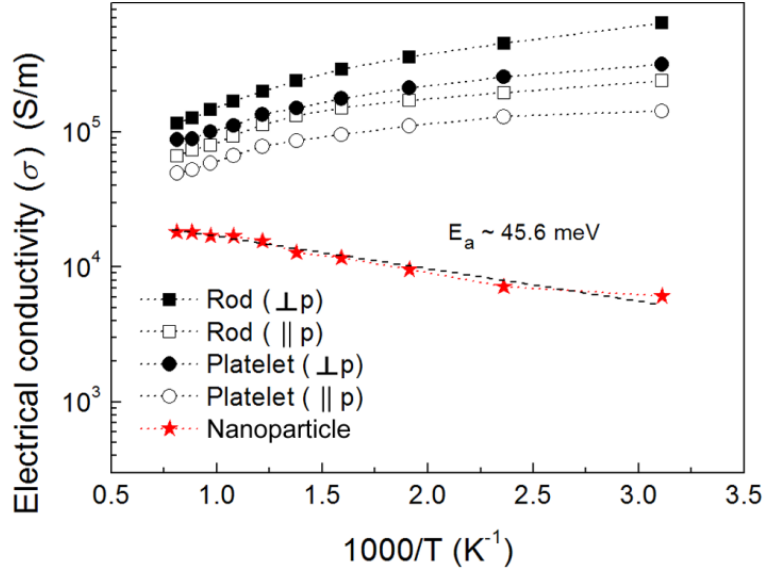


Fig. 5.7 Temperature dependence of the electrical conductivity of the samples, a clear anisotropy of the Rod and Platelet samples being observed.

A room temperature Hall measurement was carried out to determine the carrier concentration (n) of the samples. As shown in Fig. 5.8, the carrier concentration did not show anisotropy for these samples. The charge carrier concentration of the Rod sample is higher than that of the Platelet sample. There is a possibility of the different substitution fraction of Al^{3+} ions at the Zn sites in these two samples. This substitution not only causes the shrinkage of the unit cell, but also donates excessive electrons for conduction. As the shrinkage increases, the electron carrier concentration increases as well. (see Figs. 5.6 and 5.8). The n values of these samples are higher than 10^{20} cm^{-3} , indicating that they are degenerate semiconductors. The carrier mobility along the $\langle \perp p \rangle$ direction was found to be more than two times higher than that along the $\langle \parallel p \rangle$ direction for both Rod and Platelet samples. These findings suggest that the grain boundary scattering plays a key role for the difference in the carrier mobility in accordance with the microstructure observation. It is also noteworthy to point out that a higher mobility of $65 \text{ cm}^2 \text{ V}^{-1} \text{ s}^{-1}$ was obtained for Platelet ($\perp p$) as compared with $45 \text{ cm}^2 \text{ V}^{-1} \text{ s}^{-1}$ for Rod ($\parallel p$), although the average grain size of Platelet ($\perp p$) is smaller. This can be explained by the higher degrees of orientation in Platelet ($\perp p$), and hence the grain boundaries in Platelet ($\perp p$) may have less impact on the transport of electrons, similar observations has been previously reported [101–103]. Presumably affected by intensive boundary and impurity defect scattering, the carrier mobility of the Nanoparticle sample was the smallest among all the samples in this study. The n value of the Nanoparticle sample was also found to be the smallest. This tendency is consistent with the previous discussion on the Al^{3+} ion substitutions. A lower substitution fraction may cause a smaller shrinkage of the unit cell volume, as well as a lower electron carrier concentration.

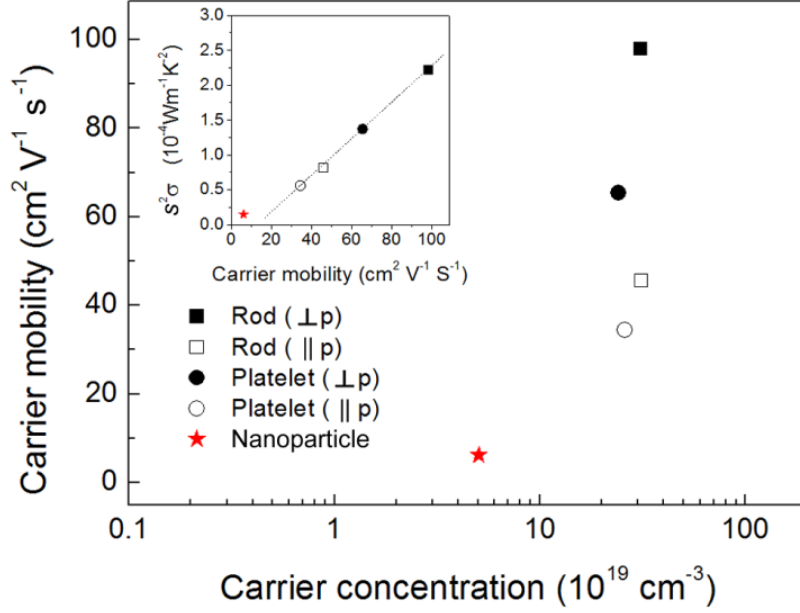


Fig. 5.8 The carrier concentration and carrier mobility of the samples at room temperature. The inset shows the monotonic increase of the power factor with increasing carrier mobility.

Fig. 5.9a shows the temperature dependence of the Seebeck coefficients (S) of the samples. The S values for the Rod and Platelet samples showed negligible anisotropy. This behavior is consistent with the theoretical calculations based on the Boltzmann transport theory [104]. According to the Pisarenko relation for degenerated semiconductors,

$$|S| = \frac{8\pi^2 k_B^2 T}{3qh^2} m^* \left(\frac{\pi}{3n}\right)^{2/3} \quad (5.3)$$

where k_B is the Boltzmann constant, T is the absolute temperature, h is Planck's constant, q is the unit charge of electron, m^* is the effective mass. As smaller n results in bigger $|S|$, the Platelet samples had a larger $|S|$ values than the Rod samples. By plotting the room temperature S vs. $n^{-2/3}$, m^* of the samples can be estimated to be between $0.43 m_e$ and $0.35 m_e$, as shown in the inset of Figure 5.9(a). The estimation of the effective mass is consistent with the results obtained by Kim et al [49]. However, the Pisarenko relation is based on carrier degeneracy, and hence m^* for the Nanoparticle sample is only a rough approximation. According to the measured n and estimated m^* values, a simple parabolic band model [6] can be applied by employing the following equations:

$$F_\lambda(\xi) = \int_0^\infty \frac{x^\lambda dx}{1+Exp(x-\xi)} \quad (5.4)$$

$$S = -\frac{k_B}{q} \left[\frac{(2+\lambda)F_{\lambda+1}}{(1+\lambda)F_\lambda} - \xi \right] \quad (5.5)$$

$$n = 4\pi \left(\frac{2m^* k_B T}{h^2} \right)^{3/2} F_{1/2} \quad (5.6)$$

where $F_\lambda(\xi)$ is the Fermi integral and ξ is the reduced electrochemical potential. λ is a scattering parameter and 0 is assumed for acoustic phonon scattering, 1 for optical phonons scattering, and

2 for ionized impurity scattering [6]. At room temperature, the calculated S values as a function of carrier concentration are shown in Fig. 5.9b. The three lines correspond to the three different scattering mechanisms. The S values for the Rod and Platelet samples corresponds very well with the calculation when $\lambda=0$, indicating that the acoustic phonon scattering is the dominating scattering mechanism. The S value for Nanoparticle sample lies below the calculated values for all the above scattering mechanisms, implying strong scattering by highly distributed grain boundaries and densely dispersed nanoprecipitates.

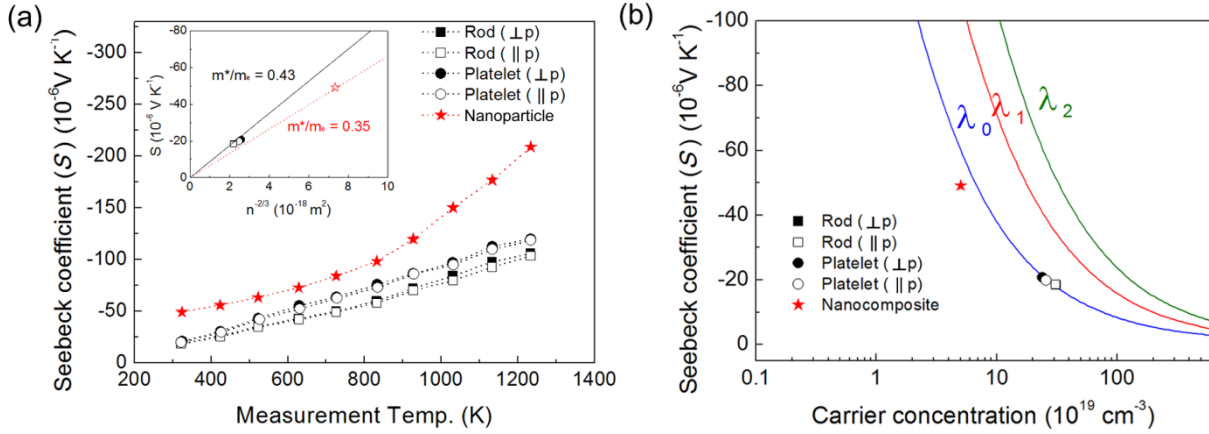


Fig. 5.9 (a) Temperature dependence of the Seebeck coefficient of the samples. The inset shows the plot of the room temperature Seebeck coefficient vs. (carrier concentration)^{-2/3}. The colored diagonal lines correspond to the theoretical relationship when $m^*/m_e = 0.43$ and 0.35 according to the Pisarenko relation. (b) The Seebeck coefficient plotted as a function of the carrier concentration. The solid colored lines are the calculated values for $\lambda = 0, 1,$ and 2 , denoting electron scattering by acoustic phonons, optical phonons, and ionized impurities respectively.

Fig. 5.10a shows the thermal conductivity as a function of temperature for all the samples. The measured data of the thermal diffusivity and specific heat at a constant pressure are shown in Figs. S4 and S5 in Appendix B. The apparent effect of anisotropy on the thermal conductivity can be observed from the Rod and Platelet samples. The κ values measured along the pressure axis ($\parallel p$) for both samples are relatively smaller compared with the values measured perpendicular to the pressure axis ($\perp p$) over the whole temperature range. The Nanoparticle sample showed significantly small κ values of $8.46 \text{ Wm}^{-1}\text{K}^{-1}$ at 373K and $3.21 \text{ Wm}^{-1}\text{K}^{-1}$ at 1223 K , which are roughly $1/5$ and $1/2$ as large as those for the Rod ($\perp p$) sample at 373 K and 1223 K , respectively. These small κ values are comparable to those previously reported for the Al-doped ZnO nanocomposites [52–54]. For the reference, the theoretical lower limit of the lattice thermal conductivity, κ_{\min} , for $\text{Zn}_{0.98}\text{Al}_{0.02}\text{O}$ was calculated to be $1.22 \text{ Wm}^{-1}\text{K}^{-1}$ as shown in Fig. 5.10a. To estimate the lattice contribution κ_L to the total κ , the following equation was applied:

$$\kappa_L = \kappa - \kappa_e = \kappa - L_0 \sigma T \quad (5.7)$$

where κ_e is the electron component of κ . The degenerate limit of the Lorenz number is given by $L_0 = (\pi^2 k_B^2 / q^2) = 2.45 \times 10^{-8} \text{ W}\Omega\text{K}^{-2}$, and is valid only at high degeneracy regardless of the

carrier scattering mechanism. At high temperatures, this value typically results in an overestimation of κ_e . In this case, the following equation was used for the calculation of L_o [6]:

$$L_o = \left(\frac{k_B^2}{q^2}\right) (3F_0F_2 - 4F_1^2)/F_0^2 \quad (5.8)$$

where F_n denotes $F_n(\zeta)$. The results of these calculations for the different morphologies are shown in the inset of Fig. 5.10a. The L_o values are consistently smaller than the degenerate limit and monotonically decrease with increasing temperature. By using Eq. 5.7, the κ_L values can be extracted, as shown in Fig. 5.10b. The values of κ_L are somehow similar to the values of κ , indicating that the lattice component dominates the thermal conductivity for all the samples. The Nanoparticle sample shows the lowest κ_L among all the samples in this study, and a clear anisotropy of κ_L can be observed for the Rod and Platelet samples. The Debye-Callaway model [105–107] was used to calculate the lattice thermal conductivity using parameters obtained by microscopy (see Appendix B). The calculated values are shown as solid lines in Fig. 5.10b, agreeing well with the experimental data. The calculations indicated that the anisotropy of κ_L for the Rod and Platelet samples was mainly caused by grain boundaries. The grain sizes along the pressure axis are nearly 5 to 8 times smaller than those in the perpendicular direction, which resulted in a smaller phonon mean free path along this direction. The calculation also clearly shows the temperature-dependent anisotropic behavior of κ_L for the Rod and Platelet samples, where κ_L along the (\perp p) and (\parallel p) directions differs noticeably at 300K, but the difference became smaller and unobvious above 800K. As for the Nanoparticle sample, very low κ can be attributed to the strong phonon scattering from nano-grains, point defects and densely dispersed nanoprecipitates.

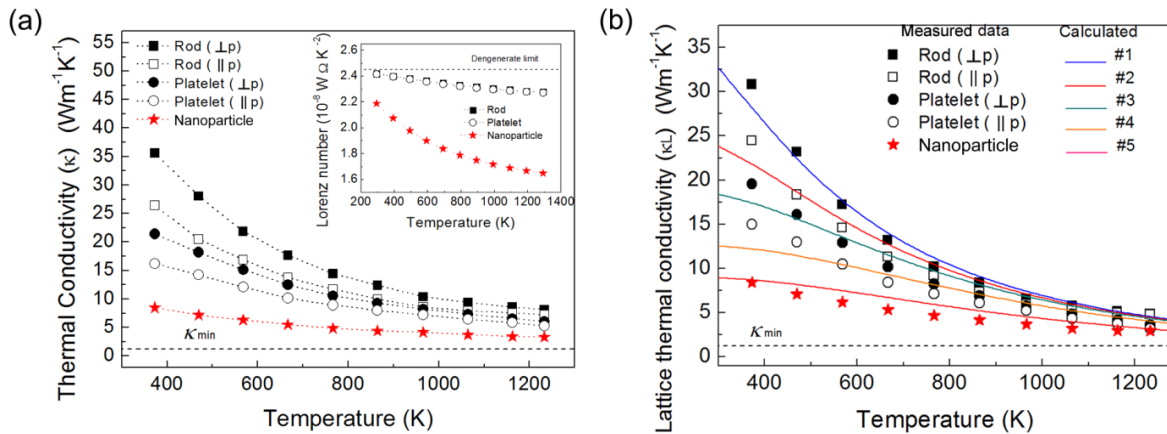


Fig. 5.10 (a) Temperature dependence of the thermal conductivity of the samples. The inset shows the calculated Lorenz number of the samples as a function of temperature. The lower limit of the lattice thermal conductivity, κ_{\min} , for $\text{Zn}_{0.98}\text{Al}_{0.02}\text{O}$ was calculated using Cahill's equation (dashed line). (b) Temperature dependence of lattice thermal conductivity of the samples. The solid color lines are the calculated values using the Debye-Callaway model.

5.3.3 Theoretical Analysis and Discussion

To further analyze the effects of grain boundaries and nanoprecipitates on phonon scattering, κ_L at three different temperature (273 K, 673 K, and 1223 K) was plotted as a function of grain size using the Debye-Callaway model (as shown in Fig. 5.11a). The calculated values agree with the experimental values in this study. By changing the grain size from 100 μm to 10nm, κ_L at 273K reduced significantly, but κ_L at 1223 K was hardly affected. This is consistent with some results reported previously, showing that the nano-scaled grains have a limited effect to reduce lattice thermal conductivity at high temperature region, where the phonon-phonon scattering dominates [57,108]. As for the phonon scattering by nanoprecipitates, κ_L vs. nanoprecipitates particle concentration was also plotted as shown in Fig. 5.11b. κ_L at both 273 K and 1223 K decreased noticeably with increasing particle concentration. The phonon scattering by grain boundaries and nanoprecipitates can be illustrated by plotting the phonon mean free path (MFP) vs. normalized phonon frequency ($\hbar\omega/K_B T$) as shown in Fig. 5.11c and d. The dashed lines are the reference MFP values without neither grain boundary scattering nor nanoprecipitate scattering. When grain boundary scattering takes place, given the grain size of 400nm, the phonon MFP at the low frequency region reduces significantly, leaving the high frequency phonons nearly unaffected (see the blue area in Fig. 5.11c); when nanoprecipitates scattering takes place, given the size of 10nm and concentration of $1.4 \times 10^{20} \text{m}^{-3}$, the phonon MFP at both intermediate and high frequency regions decreases moderately (see the red area Fig. 5.11c). At 1223 K, however, the grain boundary scattering becomes very limited, while the scattering from nanoprecipitates is still very well pronounced (see the red area in Fig. 5.11d). It indicates that, the grain boundaries selectively depress the phonon spectrum at the low frequency region, while the nanoprecipitates selectively depress the phonon spectrum at the intermediate and high frequency region. By combining the two scattering mechanisms, the entire phonon spectrum can be effectively dampened. The Nanoparticle sample could have benefited from the combined scattering mechanisms. The low frequency phonons were scattered by nanograins, and the middle to high frequency phonons were scattered by point defects and highly dispersed nanoprecipitates. Thus the sample showed the strongly suppressed lattice thermal conductivity. The above observations and discussion are consistent with the work by Biswas et al [9].

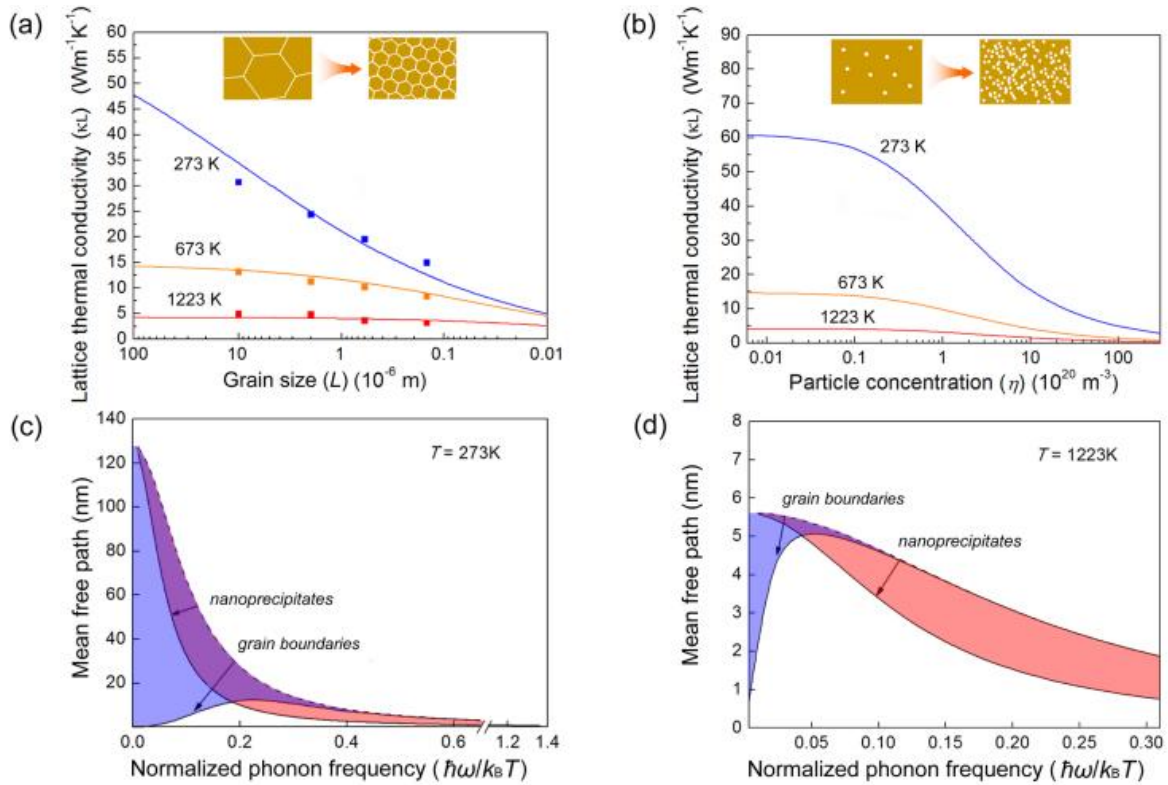


Fig. 5.11 Calculated lattice thermal conductivity plotted as a function of (a) grain size, and (b) nanoprecipitate particle concentration at different temperatures. The calculated mean free path (MFP) of the phonons was plotted as a function of normalized phonon frequency at (c) 273K and (d) 1223K. The dots in (a) are experimental values of Rod ($\perp p$), Rod ($\parallel p$), Plate ($\perp p$), and Plate ($\parallel p$), with grain sizes of 10 μm , 2 μm , 600 nm and 150 nm, respectively; the dashed lines in (c) and (d) are the reference MFP values without phonon scattering by neither grain boundaries nor nanoprecipitates, and the solid lines are predicted values when phonon scattering by either nanoprecipitates or grain boundaries dominates.

The zT values thus obtained are shown in Fig. 5.12. Due to the preferential orientation of the Rod and Platelet samples, they showed different zT values along the different measured directions. The ($\perp p$) direction of both samples showed higher zT values than the ($\parallel p$) direction, reaching 0.2 to 0.25 at 1223 K. The Platelet sample showed higher zT values than the Rod sample along either measurement directions. The Nanoparticle sample was benefited from low κ of 3.2 $\text{Wm}^{-1}\text{K}^{-1}$ at 1223 K, and its electrical conductivity and Seebeck coefficient increased significantly with increasing temperature, attaining a power factor of $7.97 \times 10^{-4} \text{Wm}^{-1}\text{K}^{-2}$ at 1223 K. Thus the sample showed a peak zT of 0.3 at 1223 K, which is comparable to the zT values achieved by Al-doped ZnO bulk materials [52,95] but somehow lower than those of some other Al-doped ZnO nanocomposites reported [53,54]. As demonstrated in this paper, the Rod and Platelet samples exhibited fairly high electrical transport properties along the preferred directions due to the alignment of the micron-scale grains. However these grains are less effective to scatter high frequency phonons at high temperatures. On the other hand, the Nanoparticle sample with highly dispersed nanoprecipitates exhibited the strong suppression of the lattice thermal conductivity due to the effective scattering of phonons. It indicates that a combination of these

features, the alignment of micron-scale anisotropic grains and highly dispersed nanoprecipitates within/around them, would be a promising way to maintain sufficient electrical transport properties with suppressing the lattice thermal conductivity, thus being capable of improving zT of Al-doped ZnO further.

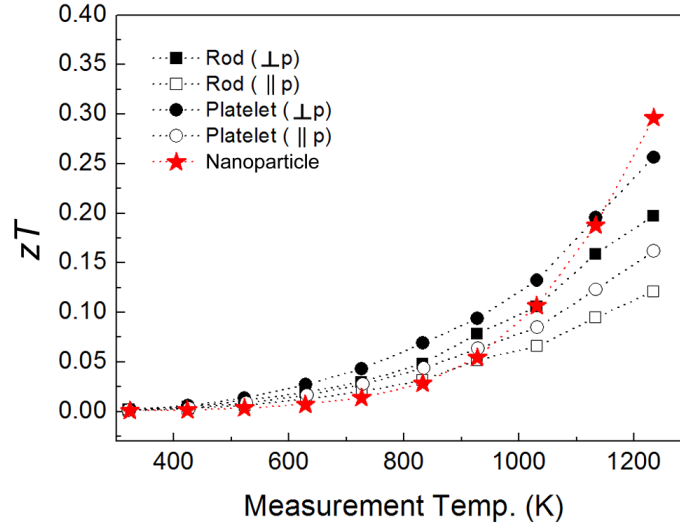


Fig. 5.12 Temperature dependence of figure-of-merit, zT , of the samples.

5.4 Conclusions

Nanostructured Al-doped ZnO nanostructured bulk samples were fabricated using precursors with different morphologies and SPS consolidation. Those fabricated from rods and platelets as starting powders exhibited textured microstructures and anisotropic thermoelectric properties. The anisotropy of the electrical and thermal conductivities was attributed to the grain boundary scattering in the samples with preferred orientation of the anisotropic grains, which are interacting in a different manner with the electron and phonon conduction. The Platelet sample with aligned laminar grains showed a superior zT value of 0.25 at 1223 K along the preferred ($\perp p$) direction, which is $\sim 47\%$ higher than our previously made non-textured bulk samples [56]. The Nanoparticle sample exhibited fine structure of micron-scaled grains and nanoprecipitates. A zT value of 0.3 at 1223 K was attained by the low κ . By using the Debye-Callaway model in combination with the experimental observations, the influence of grain boundaries and nanoprecipitates on the heat transport was investigated. The results showcased the selective depression of the phonon spectrum by grain boundary and nanoprecipitate scattering, also being capable of explaining the low κ obtained by the Nanoparticle sample as well as the anisotropic κ_L of the Rod and Platelet samples. This work elucidated the effect of the structural features on the electron/phonon transport properties of Al-doped ZnO bulks, and provided a promising approach to further improve the thermoelectric properties of Al-doped ZnO. However, the long-term stability of the tailored nanostructures was not included in this work since it is still under investigation, and further strategy for improving the high temperature thermoelectric efficiency of ZnO-based materials will be employed in our future work.

Chapter 6 Doped ZnCdO as stable n-type material for thermoelectric application

Abstract:

New composition of doped ZnCdO was developed. The thermoelectric properties and thermal stability of doped Zinc Cadmium Oxide ($\text{Zn}_{1-x}\text{Cd}_x\text{A}_y\text{O}$, A = Sc, Ga, Ce, Mg, Sn etc.) are investigated. Doped ZnCdO has a significant lower thermal conductivity (8.0 to $2.0 \text{ W/m}^{-1}\cdot\text{K}^{-1}$ from RT to 1173K) as compared with the ZnO:Al (49 to $8.0 \text{ Wm}^{-1}\cdot\text{K}^{-1}$ from RT to 1173K). Sc-doped ZnCdO also exhibits a rather low electrical resistivity (1.5×10^{-3} – $3.8\times 10^{-3} \Omega\cdot\text{cm}$) and good thermopower (70 – $160 \mu\text{V/K}$) in a wide temperature range from 300 up to 1173 K. The dimensionless figure-of-merit (zT) that determines the conversion efficiency of a thermoelectric power generator is found to be ~ 0.3 @1173 K and ~ 0.24 @1073K, which are comparable or better than the state-of-the-art n-type thermoelectric oxide materials. In this chapter, the thermoelectric properties of a series of samples with varied concentrations of Cd, Sc, and some other dopants are investigated and discussed in detail.

The work discussed in this chapter is in preparation for publication and used for a patent application.

6.1 Introduction

Thermoelectric (TE) technology is one of the most promising energy conversion technologies like photovoltaic, wind energy, and fuel cells etc. It directly converts heat into electricity without any moving parts. Its superior reliability has made it a crucial long-life power sources for space needs since the 1950s[6]. For civil use, thermoelectrics offers a promising solution for waste heat recovery[5]. By integrating thermoelectric generators into many systems such as cars, fossil fuel power stations, and solar panels etc., the overall energy efficiency of the system can be improved. For industrial processes like those involving petroleum, steel manufacturing, transportation etc., there is an abundance of exploitable high temperature (above 800 K) waste heat. It calls for thermoelectric systems consisted of high temperature stable materials with decent thermoelectric properties. Among many different types of materials, oxides are supposed to be a promising candidate due to their potentially high temperature chemical stability, abundant resources, and low-cost processing[27].

The current state-of-the-art oxide thermoelectric materials are calcium cobaltates for p-type[11,28], strontium titanates (STO)[109,110], aluminum-doped zinc oxide (AZO)[50,89], and calcium manganates (CMO)[32,34,111]for n-type. Promising zT of 0.61 at 1118 K and reliable thermal stability had been achieved for the p-type calcium cobaltates[11]. However, the n-type oxide candidates are suffering from either lower zT or poorer thermal stability[27]. ZnO based thermoelectric materials will experience severe degradation of electrical conductivity during the operation in air above 600 K due to restored oxygen vacancies[112]. Strontium titanates were also reported to be unstable in air above 670 K because the Ti^{3+} in STO is unstable and become easily oxidized to Ti^{4+} , thus the zT will intensively decrease in air above 670 K[27]. Calcium manganate is a good candidate at high temperature but the zT values are still much lower than the best p-type oxide materials[113,114]. Therefore, better n-type oxide candidates are needed for oxide thermoelectric module construction and sufficient energy conversion efficiency.

The integration of nanostructuring to the ZnO based thermoelectrics has become a popular topic since 2010 [7,10,53,57].The Al-doped ZnO nanocomposites sintered using nano precursors has achieved an ultra low thermal conductivity of $2.8 \text{ Wm}^{-1}\text{K}^{-1}$ at room temperature[54]. Though the nanostructuring has been proved to be useful for the reduction of thermal conductivity of Al-doped ZnO, there was also a consequence of heavily decreased electrical conductivity[7]. As a result, the nanostructuring of Al-doped ZnO turned out to be only useful for achieving a high peak zT at high temperature, but the near room temperature zT is usually lower than the zT from bulk samples due to lower electrical conductivity. However, there are other strategies for reducing its thermal conductivity which might be as effective as nanostructuring, like alloying. Accordingly, we selected CdO to alloy with ZnO because they have moderate solubility as well as significant atomic weight difference with each other. Besides, CdO is a n-type oxide semiconductor with superb carrier mobility as high as $230 \text{ cm}^2\text{V}^{-1}\text{s}^{-1}$ at room temperature[115]. Herein, we developed a new doped zinc cadmium oxide as a new n-type oxide compound for high temperature thermoelectric application. This material shows promising TE properties and

high-temperature stability in air. In this chapter, the electrical and thermal transport properties will be presented in detail and a discussion in order to understand the reason for the improved TE properties will also take place. Samples with different dopants and dopant concentrations will be systematically investigated to explore the potentials of this new n-type oxide compound.

6.2 Experimental Procedure

6.2.1 Preparation of samples

Doped Zinc Cadmium Oxide ($Zn_{1-x}Cd_xA_yO$, $A = Sc, Ga, Ce, Mg, Sn$ etc.) were all obtained by e.g. a conventional solid-state-reaction (SSR) from the starting powders of ZnO, CdO, Sc_2O_3 , Ga_2O_3 , Ce_2O_3 , MgO, Sn_2O_3 . The powders were mixed at different molar ratios by roll milling using ceramic balls for 24 h. The resulting mixtures were then uniaxial pressed with $\Phi 20$ mm stainless steel die under 65 MPa for 60 seconds followed by isostatic pressing under 5 GPa for 60 seconds. The green body was sintered in chamber furnace with a heating and cooling rate of 1 K/min at 850 °C for 24 h in air and then 1300 °C for 5h in air to maintain the oxygen stoichiometry. The sintered bodies reached relative densities above 96%. The sintered bulk material were then cut into desired configurations with diamond cutter and used for thermoelectric characterizations.

6.2.2 Measurements

The electrical resistivity (ρ) and Seebeck coefficient (S) were measured simultaneously using an ULVAC-RIKO ZEM-3 under a low pressure of helium atmosphere from room temperature up to 1173 K. Hall measurement was carried out at room temperature by van der Pauw method with a superconducting magnet (measured up to 2 T). The thermal conductivity (κ) was determined from the thermal diffusivity (α), the mass density (D_m) and the specific heat capacity (C_p) according to the equation $\kappa = \alpha D_m C_p$. The thermal diffusivity was obtained by the laser flash method (Netzsch LFA-457, Germany), the mass densities of the samples were measured by Archimedes' method using water with surfactant, and the specific heat capacities were estimated using Dulong-Petit law. X-ray diffraction (XRD) pattern to examine the phase purity of the materials was obtained using a Bruker D8 diffractometer (Bruker, Germany) with $Cu-K\alpha$ radiation. A scanning electron microscope (SEM, Supra; Carl Zeiss, Inc., Germany) was used to observe the microstructures of the samples.

6.3 Results and discussions

6.3.1 Structural properties

Different samples with varied amount of Cd were investigated using XRD. For $Zn_{1-x}Cd_xSc_{0.02}O$ ($x = 0$ to 0.15) samples, the main crystalline structure of this material appears to be wurtzite belonging to the space group of P63mc, similar to pure ZnO, as shown in Fig. 6.1 a. For samples with $x = 0.15$ and 0.125, the secondary phase be observed by the peaks marked with ‘*’

in Fig. 6.1a. Those peaks are identical to those peaks of pure CdO. It indicates that once the molar ratio of CdO and ZnO exceeds 1:9, the excess CdO phase could not fully incorporate into the ZnO under our sintering conditions discussed in the previous section 6.2. When the ratio is below 1:9, CdO can very well incorporate with wurtzite ZnO phase, this result is similar to the previous observations by Venkatachalapathy et al [116]. As the Cd concentration increases, the unit cell volumes increases accordingly (see Table 6.1 and Fig. 6.1b). The main peaks slightly shift to the left (see Fig. 6.1a). This is because the ionic radius of Cd^{2+} (0.078 nm, 4-fold coordination) is larger than that of Zn^{2+} (0.06 nm, 4-fold coordination). The Cd substitutions at Zn sites will expand the unit cell volume. For samples with $x = 0, 0.05$ and 0.1 , the Sc_2O_3 phase belonging to I213 space group can be observed by a weak peak marked with ‘o’ in Fig. 6.1a. Table 6.1 gives the detailed parameters from Rietveld refinement of the XRD patterns. For the sample of $\text{Zn}_{0.85}\text{Cd}_{0.15}\text{Sc}_{0.02}\text{O}$, the cell volume is surprisingly smaller than that of $\text{Zn}_{0.875}\text{Cd}_{0.125}\text{Sc}_{0.02}\text{O}$ and comparable to that of $\text{Zn}_{0.9}\text{Cd}_{0.1}\text{Sc}_{0.02}\text{O}$. This may be explained by the failed incorporation of Cd with Zn due to excessive CdO aggregations.

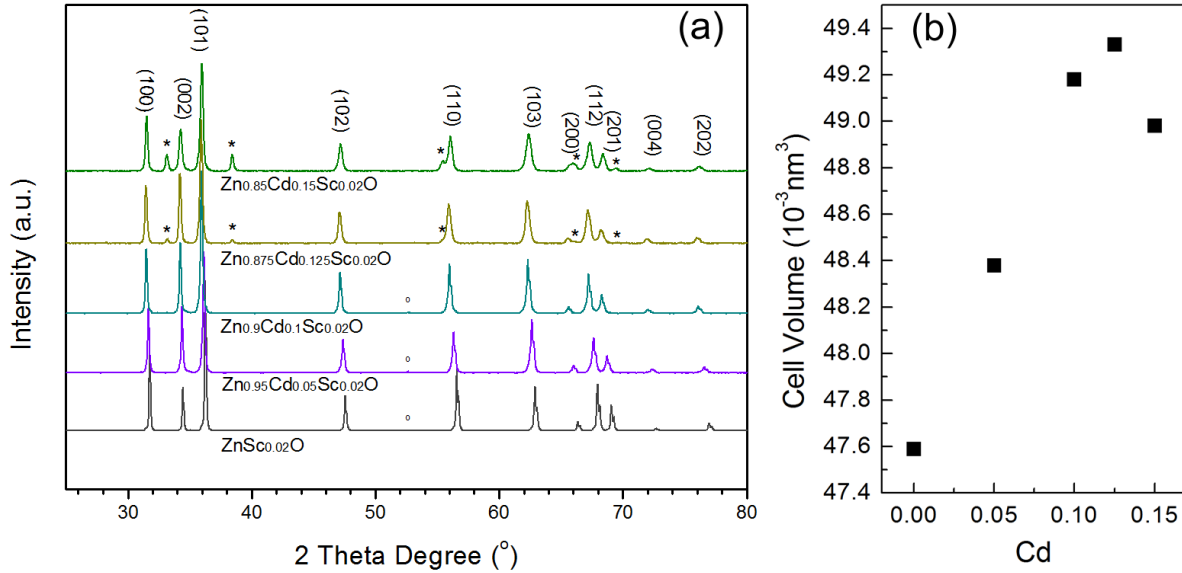


Fig. 6.1 (a) The XRD patterns for $\text{Zn}_{1-x}\text{Cd}_x\text{Sc}_{0.02}\text{O}$ ($x = 0$ to 0.15) samples. (b) Refined unit cell volume of the primary phase plotted as a function of Cd composition.

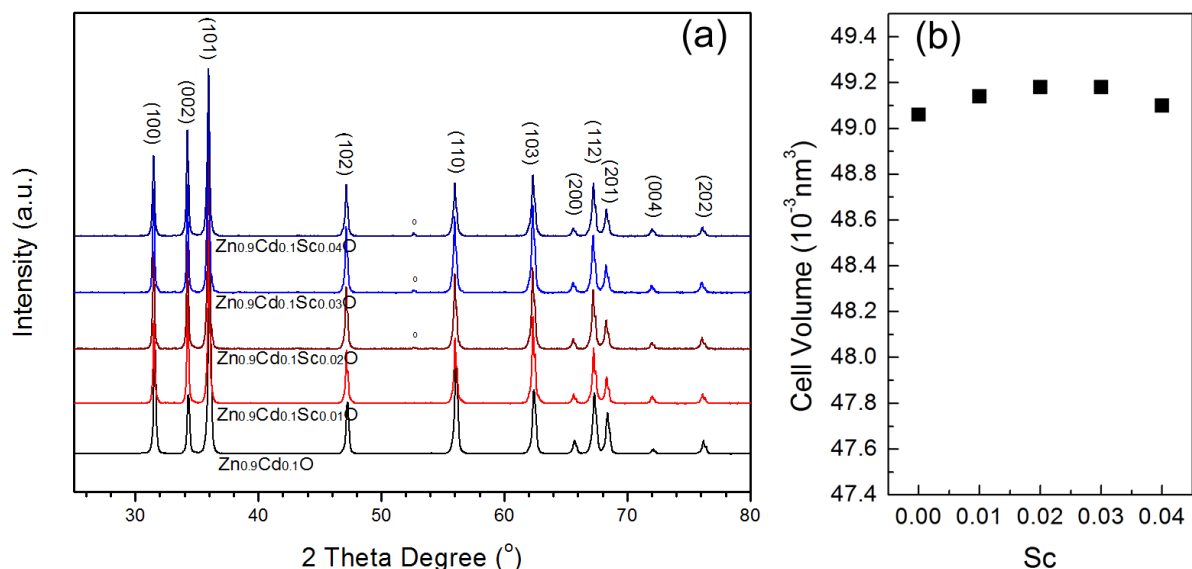


Fig. 6.2 (a) The XRD patterns for $Zn_{0.9}Cd_{0.1}Sc_yO$ ($y = 0$ to 0.04) samples. (b) Refined unit cell volume of the primary phase plotted as a function of Sc composition.

Table 6.1 Parameters from Rietveld refinement for $Zn_{1-x}Cd_xSc_{0.02}O$ ($x = 0$ to 0.15) samples.

| Sample | Main phase: Zincite | | | | | | Secondary phase | | | | | R-Values | | | |
|----------------------------------|---------------------|------------------------|------|------|-------------------------------|--------------------|-----------------|------------------------|------|------|-------------------------------|--------------------|------------------|-----------------|------|
| | Space group | Lattice parameters (Å) | | | Cell Volume (Å ³) | Wt% - Rietveld (%) | Space group | Lattice parameters (Å) | | | Cell Volume (Å ³) | Wt% - Rietveld (%) | R _{exp} | R _{wp} | GOF |
| | | a | b | c | | | | a | b | c | | | | | |
| $ZnSc_{0.02}O$ | P63mc | 3.25 | 3.25 | 5.20 | 47.59 | 99.440 | I213 | 9.84 | 9.84 | 9.84 | 954.5 | 0.560 | 2.95 | 10.6 | 3.62 |
| $Zn_{0.95}Cd_{0.05}Sc_{0.02}O$ | P63mc | 3.27 | 3.27 | 5.23 | 48.38 | 99.276 | I213 | 9.84 | 9.84 | 9.84 | 953.5 | 0.724 | 3.66 | 8.69 | 2.37 |
| $Zn_{0.9}Cd_{0.1}Sc_{0.02}O$ | P63mc | 3.28 | 3.28 | 5.25 | 49.18 | 99.683 | I213 | 9.85 | 9.85 | 9.85 | 956.5 | 0.317 | 3.54 | 7.41 | 2.09 |
| $Zn_{0.875}Cd_{0.125}Sc_{0.02}O$ | P63mc | 3.29 | 3.29 | 5.25 | 49.33 | 97.817 | Fm3m | 4.69 | 4.69 | 4.69 | 103.33 | 2.183 | 3.81 | 8.99 | 2.36 |
| $Zn_{0.85}Cd_{0.15}Sc_{0.02}O$ | P63mc | 3.28 | 3.28 | 5.24 | 48.98 | 93.392 | Fm3m | 4.69 | 4.69 | 4.69 | 103.18 | 6.608 | 3.61 | 8.80 | 2.44 |

Table 6.2 Parameters from Rietveld refinement for $Zn_{0.9}Cd_{0.1}Sc_yO$ ($y = 0$ to 0.04) samples.

| Sample | Main phase: Zincite | | | | | | Secondary phase | | | | | R-Values | | | |
|------------------------------|---------------------|------------------------|------|------|-------------------------------|--------------------|-----------------|------------------------|------|------|-------------------------------|--------------------|------------------|-----------------|------|
| | Space group | Lattice parameters (Å) | | | Cell Volume (Å ³) | Wt% - Rietveld (%) | Space group | Lattice parameters (Å) | | | Cell Volume (Å ³) | Wt% - Rietveld (%) | R _{exp} | R _{wp} | GOF |
| | | a | b | c | | | | a | b | c | | | | | |
| $Zn_{0.9}Cd_{0.1}O$ | P63mc | 3.28 | 3.28 | 5.25 | 49.06 | 100 | | | | | | | 2.89 | 9.69 | 3.35 |
| $Zn_{0.9}Cd_{0.1}Sc_{0.01}O$ | P63mc | 3.29 | 3.29 | 5.25 | 49.14 | 100 | | | | | | | 3.53 | 7.70 | 2.18 |
| $Zn_{0.9}Cd_{0.1}Sc_{0.02}O$ | P63mc | 3.29 | 3.29 | 5.25 | 49.18 | 99.683 | I213 | 9.85 | 9.85 | 9.85 | 956.5 | 0.317 | 3.54 | 7.41 | 2.09 |
| $Zn_{0.9}Cd_{0.1}Sc_{0.03}O$ | P63mc | 3.29 | 3.29 | 5.25 | 49.18 | 99.059 | I213 | 9.85 | 9.85 | 9.85 | 955.2 | 0.941 | 3.57 | 8.08 | 2.27 |
| $Zn_{0.9}Cd_{0.1}Sc_{0.04}O$ | P63mc | 3.29 | 3.29 | 5.25 | 49.10 | 98.618 | I213 | 9.85 | 9.85 | 9.85 | 954.5 | 1.382 | 3.57 | 8.08 | 2.27 |

Figure 6.2a shows an XRD of samples with different amount of Sc keeping the amount of Cd constant at 0.1. For $Zn_{0.9}Cd_{0.1}Sc_yO$ ($y = 0$ to 0.04) samples, the main crystalline structure of this material is the wurtzite which is belonging to the space group of P63mc, as shown in Fig. 6.2a. For samples with $y = 0.02, 0.03$ and 0.04 , the Sc_2O_3 phase belonging to I213 space group can be observed by weak peaks marked with ‘o’ (Fig. 6.2a). As the Cd concentration increases, the unit cell volumes remains almost constant with very slight changes (see Table. 6.2 and Fig. 6.2b). This is because the ionic radius of Cd^{2+} (0.078 nm, 4-fold coordination) is very similar to that of

Sc^{3+} (0.075 nm, 6-fold coordination) compared to that of Zn^{2+} (0.06 nm, 4-fold coordination), the substitution of Sc should mostly take place at Cd sites. Table 6.2 gives the detailed parameters from Rietveld refinement of those XRD patterns.

SEM images of the $\text{Zn}_{1-x}\text{Cd}_x\text{Sc}_{0.02}\text{O}$ ($x = 0.05$ to 0.15) samples are shown in Fig. 6.3. All the samples shown in Fig. 6.3 appear to be dense and with micron size grains. The grain sizes varied from $\sim 4 \mu\text{m}$ to $\sim 25 \mu\text{m}$. The addition of CdO into ZnO improved the sample sintering and 10 at% of Cd resulted in the largest grain sizes of to $\sim 25 \mu\text{m}$. Further addition of CdO caused the phase separation and thus changed the microstructure and resulted in smaller grains.

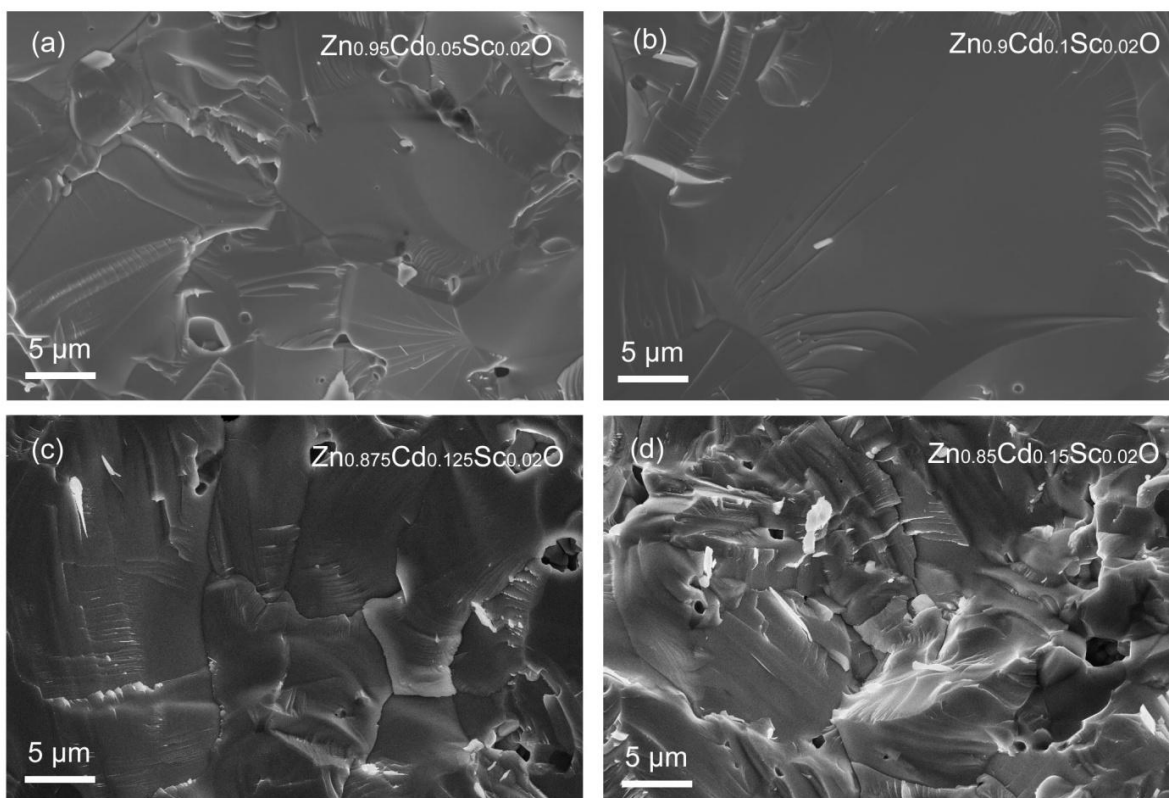


Fig. 6.3 SEM images for $\text{Zn}_{1-x}\text{Cd}_x\text{Sc}_{0.02}\text{O}$ ($x = 0$ to 0.15) samples. (a) $x = 0.05$, (b) $x = 0.1$, (c) $x = 0.125$, and (d) $x = 0.15$.

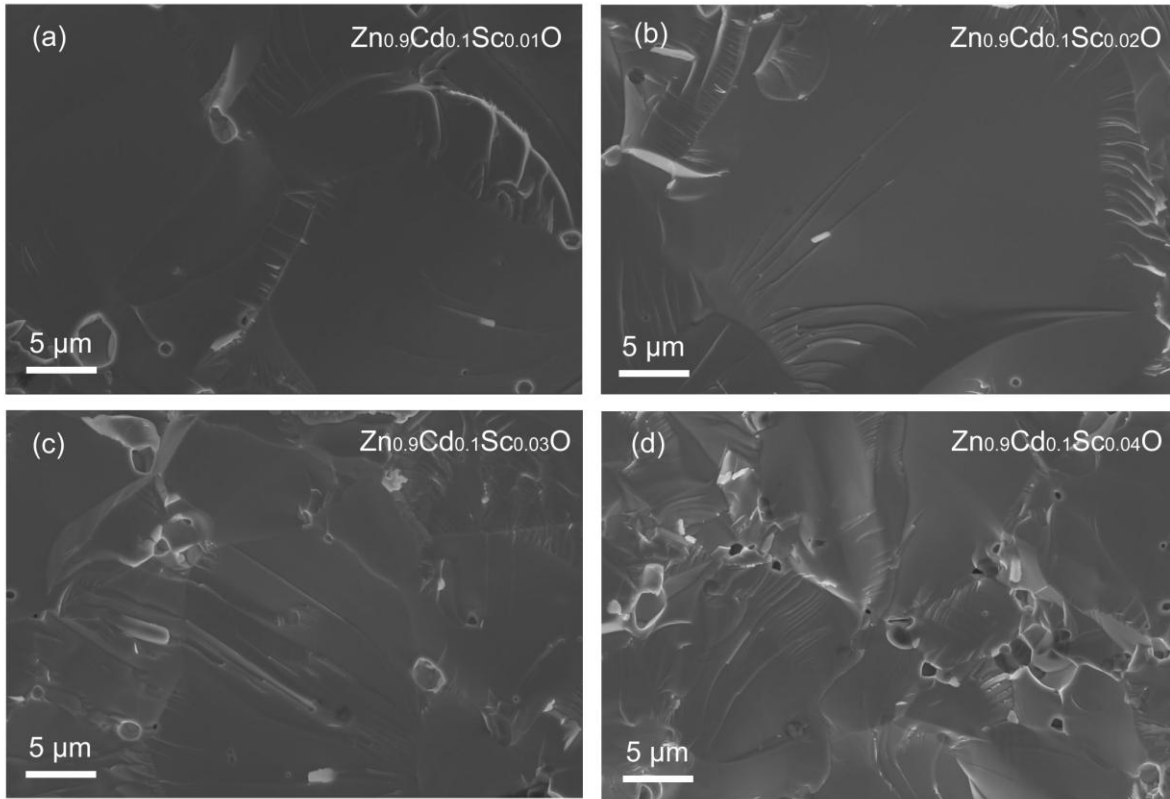


Fig. 6.4 SEM images for $Zn_{0.9}Cd_{0.1}Sc_yO$ ($y = 0.01$ to 0.04) samples. (a) $x = 0.01$, (b) $x = 0.02$, (c) $x = 0.03$, and (d) $x = 0.04$.

Fig. 6.4 shows the SEM images of $Zn_{0.9}Cd_{0.1}Sc_yO$ ($y = 0.01$ to 0.04) samples. The samples are dense, with micron size grains. The grain sizes of the samples in (a) and (b) are similar at about $\sim 25 \mu m$. When the concentration of Sc exceeded 2 at%, the grains became smaller (to ~ 5 to $10 \mu m$) and pores of approximately $\sim 1 \mu m$ appeared at grain boundaries, as shown in Fig. 6.4 (c) and (d).

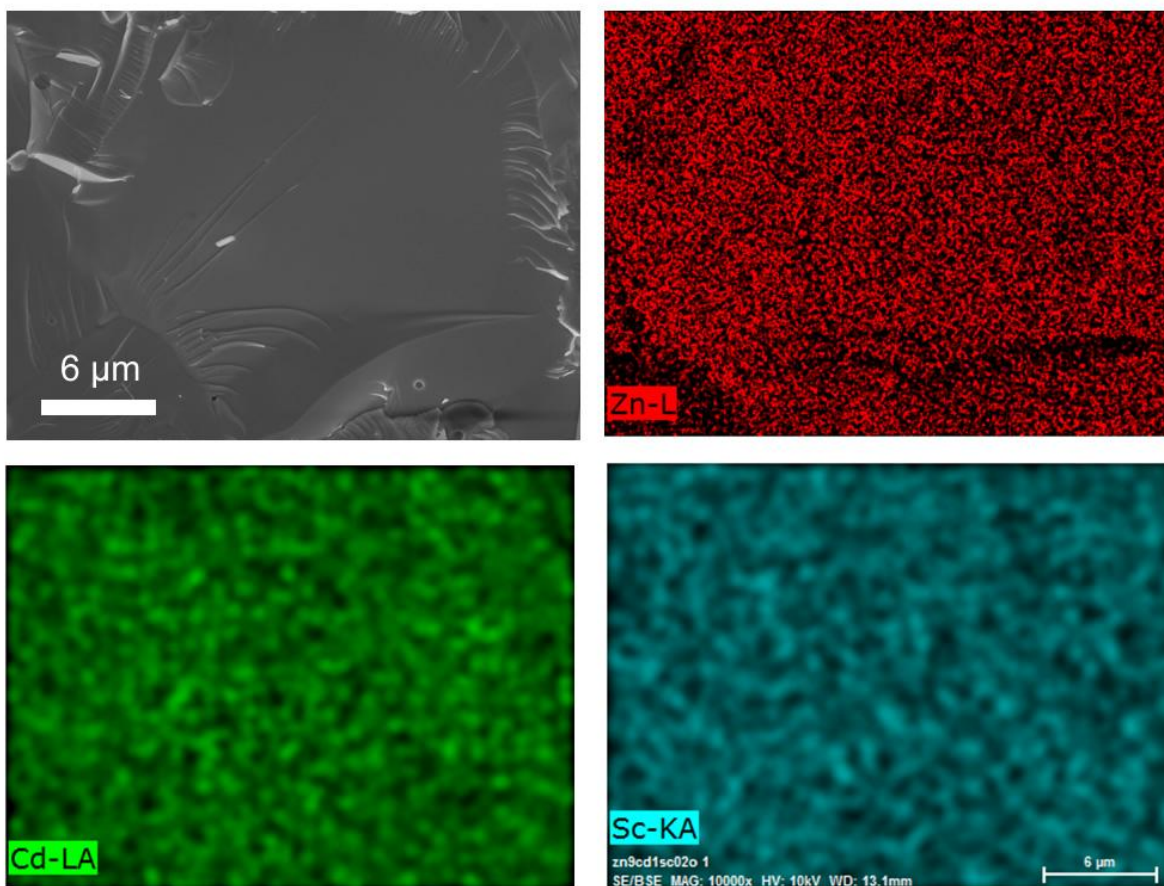


Fig. 6.5 SEM-EDS elementary mapping for $\text{Zn}_{0.9}\text{Cd}_{0.1}\text{Sc}_{0.02}\text{O}$ sample.

To verify the homogeneity and incorporation of Cd with ZnO, a SEM-EDS elemental mapping was performed on the sample $\text{Zn}_{0.9}\text{Cd}_{0.1}\text{Sc}_{0.02}\text{O}$. As shown in Fig. 6.5, the distribution of Cd and Sc in ZnO are both uniform at the grain interiors, and there is also evidence of Zn deficiency at the grain boundaries. These observations are consistent with the information observed from the X-ray diffraction patterns. The CdO and ZnO incorporated with each other and formed oxide alloys. The excessive CdO could enrich at the grain boundaries and can be detected by XRD when Cd concentration is larger than 10 at%.

6.3.2 Thermoelectric properties

The electrical resistivity (ρ) of the $\text{Zn}_{1-x}\text{Cd}_x\text{Sc}_{0.02}\text{O}$ ($x = 0$ to 0.15) samples is shown in Fig. 6.6. The $\text{ZnSc}_{0.02}\text{O}$ sample showed the highest resistivity with a mixed conduction characteristic. Its ρ first decreased from RT to 773 K like a semiconductor and then increased with increasing temperature above 773 K like a metal. The $\text{Zn}_{0.95}\text{Cd}_{0.05}\text{Sc}_{0.02}\text{O}$ sample showed second highest resistivity with metallic conduction behavior. As the Cd concentration increases, the sample resistivity decreases, and the $\text{Zn}_{0.9}\text{Cd}_{0.1}\text{Sc}_{0.02}\text{O}$ sample showed the lowest resistivity. Further increasing the Cd content resulted in increasing in resistivity. This may be explained by the

phase separation of CdO and the deterioration of the carrier mobility by increased grain boundary scattering and defect scattering. The inset of Fig. 6.6 shows the resistivity at 300 K as a function of x in $Zn_{1-x}Cd_xSc_{0.02}O$.

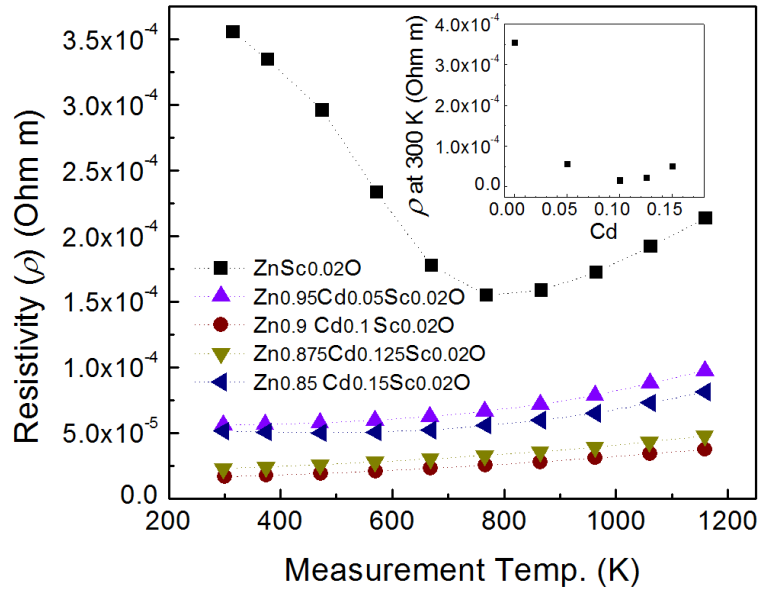


Fig. 6.6 Temperature dependence of electrical resistivity for $Zn_{1-x}Cd_xSc_{0.02}O$ ($x = 0$ to 0.15) samples.

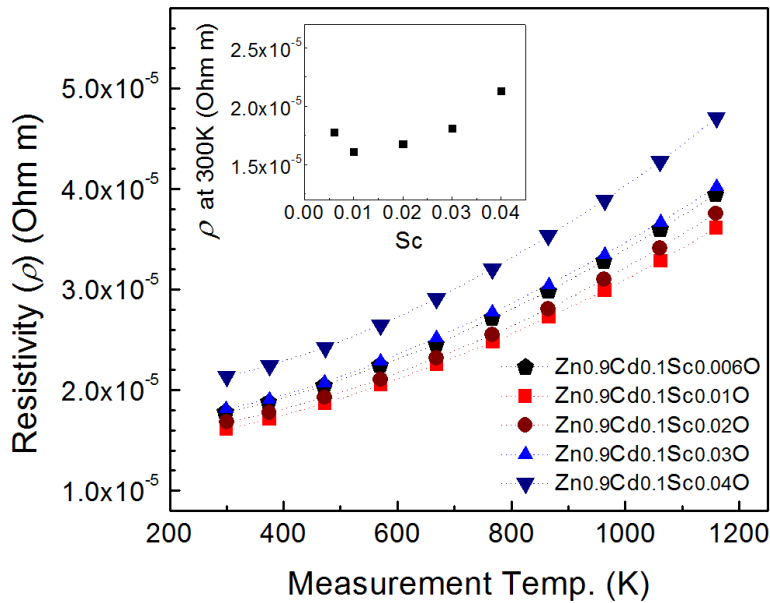


Fig. 6.7 Temperature dependence of electrical resistivity for $Zn_{0.9}Cd_{0.1}Sc_yO$ ($y = 0.006$ to 0.04) samples.

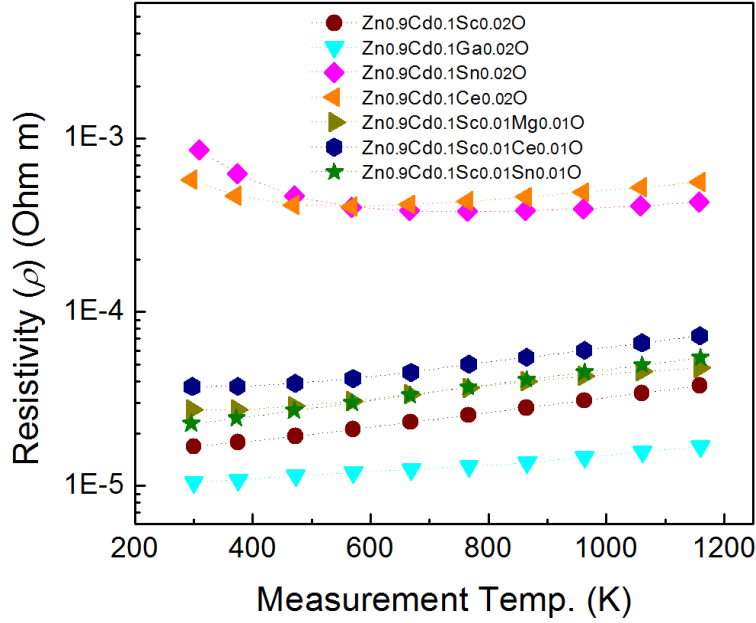


Fig. 6.8 Temperature dependence of electrical resistivity for $Zn_{0.9}Cd_{0.1}A_{0.02}O$ ($A = Sc, Ga, Sn, Ce$) and $Zn_{0.9}Cd_{0.1}Sc_{0.01}B_{0.02}O$ ($B = Mg, Sn, Ce$) samples.

The electrical resistivity (ρ) of the $Zn_{0.9}Cd_{0.1}Sc_yO$ ($y = 0.006$ to 0.04) samples is shown in Fig. 6.7. All the samples in this group showed metallic conduction behavior, the ρ increases with increasing temperature. As for the effect of Sc concentration, the resistivity of the sample first decreases as the y in $Zn_{0.9}Cd_{0.1}Sc_yO$ increases from 0.006 to 0.01 . The $Zn_{0.9}Cd_{0.1}Sc_{0.01}O$ sample shows the lowest resistivity. The resistivity started to rise with further increasing of Sc concentrations. This may be explained by the precipitation of secondary phase of Sc_2O_3 and the increased grain boundaries which may increase the electron scattering, as observed from Fig. 6.4. The inset of Fig. 6.7 shows the resistivity at 300 K as a function of y in $Zn_{0.9}Cd_{0.1}Sc_yO$.

A series of samples with different co-dopants were also investigated. Sample of co-doped or multi-doped with different elements, $Zn_{0.9}Cd_{0.1}A_{0.02}O$ ($A = Sc, Ga, Sn, Ce$) and $Zn_{0.9}Cd_{0.1}Sc_{0.01}B_{0.02}O$ ($B = Mg, Sn, Ce$) were prepared. Their electrical resistivity (ρ) as a function of temperature is shown in Fig. 6.8. The $Zn_{0.9}Cd_{0.1}Sn_{0.02}O$ and $Zn_{0.9}Cd_{0.1}Ce_{0.02}O$ samples showed a relatively high resistivity with a mixed conduction behavior similar to that of $ZnSc_{0.02}O$ sample shown in Fig. 6.6. The $Zn_{0.9}Cd_{0.1}Ga_{0.02}O$ sample showed the lowest resistivity with metallic conduction behavior and its low resistivity of 1.04×10^{-5} at 300 K is comparable to that of the best Al doped ZnO bulk materials[35]. As for the multi-doped materials $Zn_{0.9}Cd_{0.1}Sc_{0.01}B_{0.02}O$ ($B = Mg, Sn, Ce$), these compositions show higher resistivity than the $Zn_{0.9}Cd_{0.1}Sc_{0.02}O$ sample, indicating the other elements played stronger role as scattering centers for the electrons than the case of Sc.

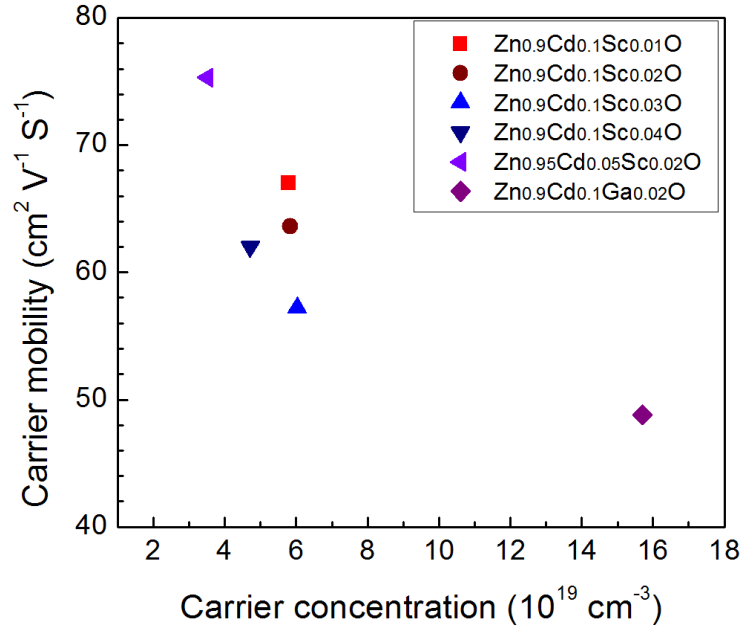


Fig. 6.9 The carrier concentration and carrier mobility of the samples at room temperature.

Table 6.3 Electrical transport properties at room temperature

| Sample | Resistivity (mΩ cm) | Seebeck coefficient (10 ⁻⁶ V K ⁻¹) | Carrier concentration (10 ¹⁹ cm ⁻³) | Carrier mobility (cm ² V ⁻¹ S ⁻¹) | D.O.S. effective mass (<i>m</i> [*] / <i>m</i> _e) |
|--|------------------------|---|--|---|---|
| Zn _{0.9} Cd _{0.1} Sc _{0.01} O | 1.610×10 ⁻⁵ | -73.9 | 5.79 | 67 | 0.56 |
| Zn _{0.9} Cd _{0.1} Sc _{0.02} O | 1.681×10 ⁻⁵ | -76.31 | 5.84 | 63.6 | 0.58 |
| Zn _{0.9} Cd _{0.1} Sc _{0.03} O | 1.813×10 ⁻⁵ | -76.51 | 6.02 | 57.2 | 0.59 |
| Zn _{0.9} Cd _{0.1} Sc _{0.04} O | 2.134×10 ⁻⁵ | -90.13 | 4.71 | 62 | 0.59 |
| Zn _{0.95} Cd _{0.05} Sc _{0.02} O | 5.642×10 ⁻⁵ | -60.12 | 3.52 | 75.3 | 0.33 |
| Zn _{0.9} Cd _{0.1} Ga _{0.02} O | 1.040×10 ⁻⁵ | -36.91 | 15.7 | 48.8 | 0.48 |

A room temperature Hall measurement was carried out to determine the carrier concentration (*n*) of the samples. As shown in Fig. 6.9, the Zn_{0.9}Cd_{0.1}Ga_{0.02}O sample showed the highest carrier concentration of $\sim 1.57 \times 10^{20} \text{ cm}^{-3}$. On the other hand, the Zn_{0.95}Cd_{0.05}Sc_{0.02}O sample showed the highest carrier mobility of $\sim 76 \text{ cm}^2 \text{ V}^{-1} \text{ S}^{-1}$, which is also higher than the Zn_{0.9}Cd_{0.1}Sc_{0.02}O sample. It indicates that Cd addition into ZnO may decrease the carrier mobility but increase the carrier concentration due to the increased Sc substitution at Cd sites. For the Zn_{0.9}Cd_{0.1}Sc_yO (*y* = 0.01 to 0.04) samples, the carrier concentration increases while the carrier mobility decreases with increasing Sc concentrations. But the Zn_{0.9}Cd_{0.1}Sc_{0.04}O sample is an exception. It has lower carrier concentration than Zn_{0.9}Cd_{0.1}Sc_{0.01}O and high carrier mobility than Zn_{0.9}Cd_{0.1}Sc_{0.03}O. This may be explained by the excessive Sc₂O₃ aggregations that resulted in fewer substitutions of Sc at Cd sites. This tendency is also consistent with the previous Rietveld refinement for Zn_{0.9}Cd_{0.1}Sc_yO (*y* = 0.01 to 0.04) samples. The increasing Sc concentration resulted in higher weight percent of secondary phases, thus deteriorated the carrier mobility as the secondary phases acted as electron scattering sites. The room temperature electrical transport properties of

these samples are included in Table 6.3. The effective mass (m^*) was obtained according to the Pisarenko relation as previously discussed [7].

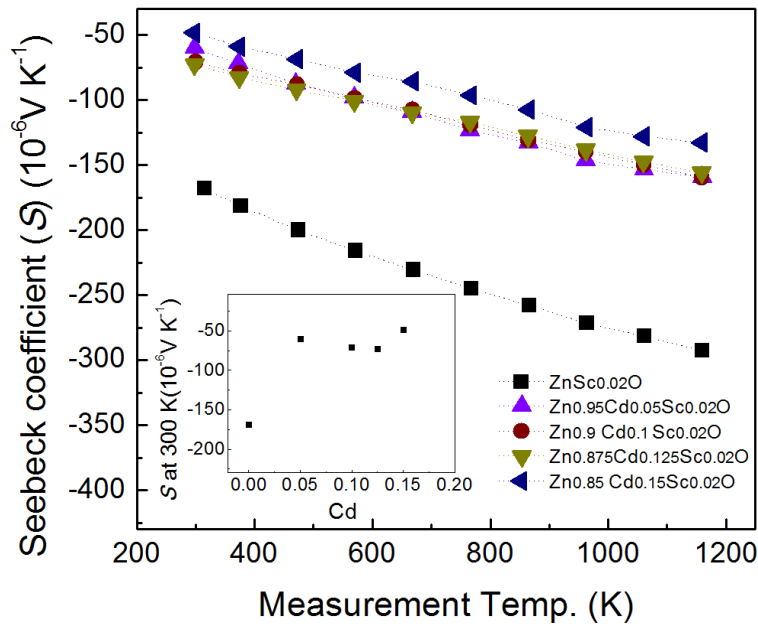


Fig. 6.10 Temperature dependence of Seebeck coefficient for $\text{Zn}_{1-x}\text{Cd}_x\text{Sc}_{0.02}\text{O}$ ($x = 0$ to 0.15) samples. The inset shows the plot of the room temperature Seebeck coefficient vs. x in $\text{Zn}_{1-x}\text{Cd}_x\text{Sc}_{0.02}\text{O}$.

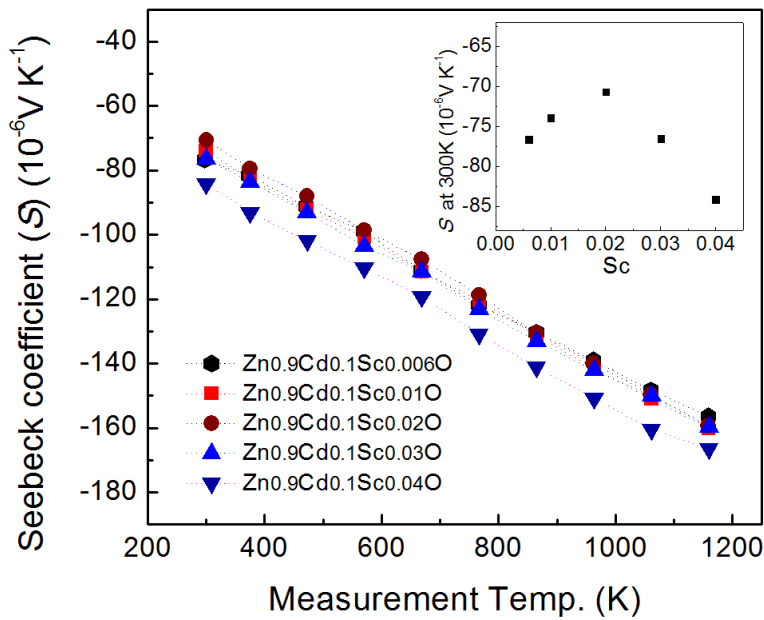


Fig. 6.11 Temperature dependence of Seebeck coefficient for $\text{Zn}_{0.9}\text{Cd}_{0.1}\text{Sc}_y\text{O}$ ($y = 0.006$ to 0.04) samples. The inset shows the plot of the room temperature Seebeck coefficient vs. y in $\text{Zn}_{0.9}\text{Cd}_{0.1}\text{Sc}_y\text{O}$.

Fig. 6.10 shows the temperature dependence of the Seebeck coefficients (S) of the $\text{Zn}_{1-x}\text{Cd}_x\text{Sc}_{0.02}\text{O}$ ($x = 0$ to 0.15) samples. All samples showed negative S values indicating n-type

conduction. And their absolute S values increased with increasing temperature due to the thermal excitation of electrons. The $\text{ZnSc}_{0.02}\text{O}$ sample has the highest $|S|$, while the $\text{Zn}_{0.85}\text{Cd}_{0.15}\text{Sc}_{0.02}\text{O}$ sample has the lowest $|S|$ values. The $|S|$ for other samples were found to be comparable to the $\text{Zn}_{0.85}\text{Cd}_{0.15}\text{Sc}_{0.02}\text{O}$ sample. The inset of Fig. 6.10 shows a plot of the Seebeck coefficient measured at room temperature vs. x for the $\text{Zn}_{1-x}\text{Cd}_x\text{Sc}_{0.02}\text{O}$.

Fig. 6.11 shows the temperature dependence of the Seebeck coefficients (S) of the $\text{Zn}_{0.9}\text{Cd}_{0.1}\text{Sc}_y\text{O}$ ($y = 0.006$ to 0.04) samples. All samples showed negative S values indicating again n-type conduction. And their absolute S values increases with increasing temperature due to the thermal excitation of electrons. The $\text{Zn}_{0.9}\text{Cd}_{0.1}\text{Sc}_{0.04}\text{O}$ sample has relatively higher $|S|$ than the others compositions due to its lower carrier concentration. The $|S|$ values for other samples were found to be very close. The inset of Fig. 6.11 shows the plot of Seebeck coefficient at room temperature vs. y for the $\text{Zn}_{0.9}\text{Cd}_{0.1}\text{Sc}_y\text{O}$.

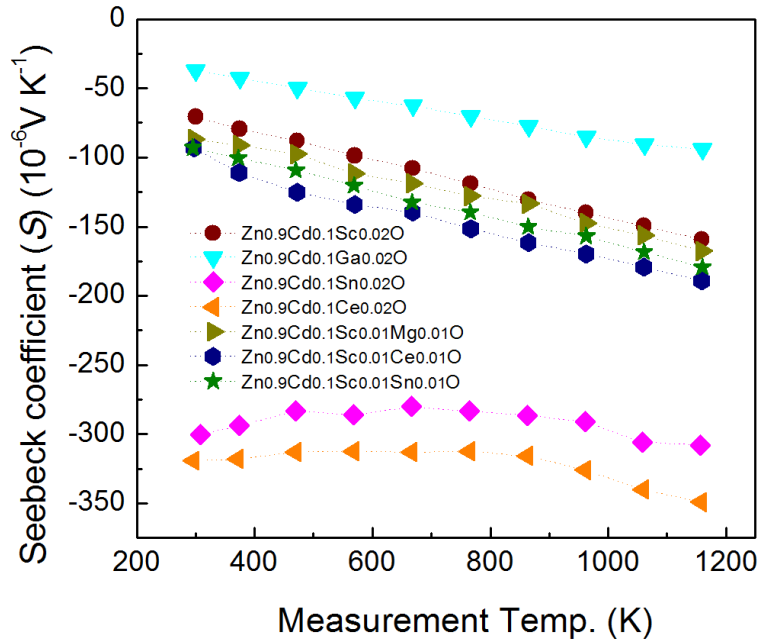


Fig. 6.12 Temperature dependence of Seebeck coefficient for $\text{Zn}_{0.9}\text{Cd}_{0.1}\text{A}_{0.02}\text{O}$ ($A = \text{Sc}, \text{Ga}, \text{Sn}, \text{Ce}$) and $\text{Zn}_{0.9}\text{Cd}_{0.1}\text{Sc}_{0.01}\text{B}_{0.02}\text{O}$ ($B = \text{Mg}, \text{Sn}, \text{Ce}$) samples.

Fig. 6.12 shows the temperature dependence of the Seebeck coefficients (S) of the $\text{Zn}_{0.9}\text{Cd}_{0.1}\text{A}_{0.02}\text{O}$ ($A = \text{Sc}, \text{Ga}, \text{Sn}, \text{Ce}$) and $\text{Zn}_{0.9}\text{Cd}_{0.1}\text{Sc}_{0.01}\text{B}_{0.02}\text{O}$ ($B = \text{Mg}, \text{Sn}, \text{Ce}$) samples. All samples showed negative S values with n-type conduction. The $\text{Zn}_{0.9}\text{Cd}_{0.1}\text{Sn}_{0.02}\text{O}$ and $\text{Zn}_{0.9}\text{Cd}_{0.1}\text{Ce}_{0.02}\text{O}$ samples showed $|S|$, which is higher than the others. The $\text{Zn}_{0.9}\text{Cd}_{0.1}\text{Ga}_{0.02}\text{O}$ sample showed the lowest $|S|$ due to its high carrier concentration. The multi-doped materials $\text{Zn}_{0.9}\text{Cd}_{0.1}\text{Sc}_{0.01}\text{B}_{0.02}\text{O}$ ($B = \text{Mg}, \text{Sn}, \text{Ce}$) showed slightly higher $|S|$ than that of the $\text{Zn}_{0.9}\text{Cd}_{0.1}\text{Sc}_{0.02}\text{O}$ sample.

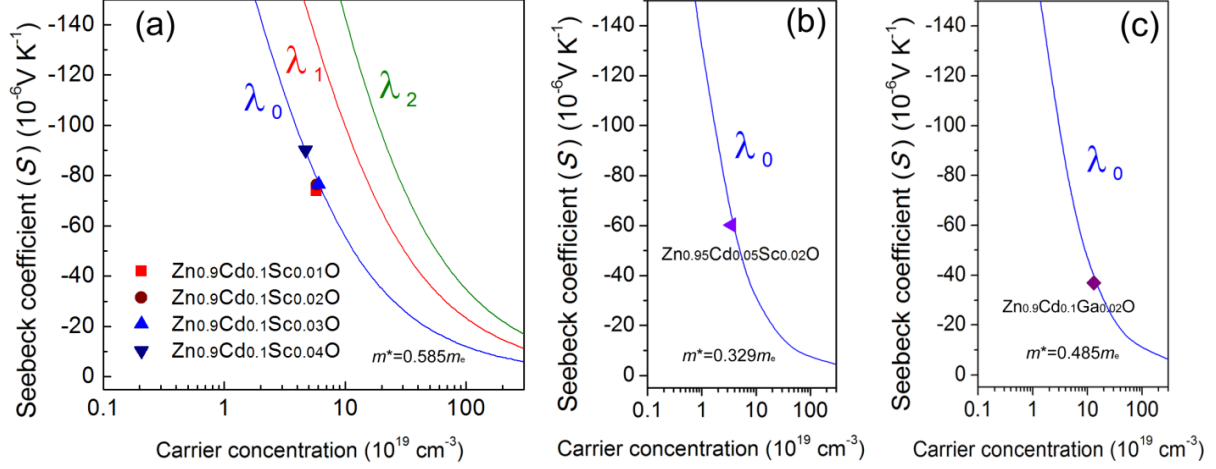


Fig. 6.13 Seebeck coefficient plotted as a function of the carrier concentration for (a) the $\text{Zn}_{0.9}\text{Cd}_{0.1}\text{Sc}_y\text{O}$ ($y = 0.01$ to 0.04) samples whose $m^* \sim 0.585 m_e$, (b) the $\text{Zn}_{0.95}\text{Cd}_{0.05}\text{Sc}_{0.02}\text{O}$ sample whose $m^* \sim 0.329 m_e$, and (c) the $\text{Zn}_{0.9}\text{Cd}_{0.1}\text{Ga}_{0.02}\text{O}$ sample whose $m^* \sim 0.485 m_e$. The solid colored lines are the calculated S values for $\lambda = 0, 1$, and 2 , denoting electron scattering by acoustic phonons, optical phonons, and ionized impurities respectively.

According to the measured n and estimated m^* values from Table 6.3, a simple parabolic band model [6] can be applied by employing the following equations:

$$F_\lambda(\xi) = \int_0^\infty \frac{x^\lambda dx}{1 + \exp(x - \xi)} \quad (6.1)$$

$$S = -\frac{k_B}{q} \left[\frac{(2 + \lambda)F_{\lambda+1}}{(1 + \lambda)F_\lambda} - \xi \right] \quad (6.2)$$

$$n = 4\pi \left(\frac{2m^*k_B T}{h^2} \right)^{3/2} F_{1/2} \quad (6.3)$$

where $F_\lambda(\xi)$ is the Fermi integral and ξ is the reduced electrochemical potential. λ is a scattering parameter and 0 is assumed for acoustic phonon scattering, 1 for optical phonons scattering, and 2 for ionized impurity scattering [6]. At room temperature, the calculated S as a function of carrier concentration is shown in Fig. 6.13. The three lines correspond to three different scattering mechanisms, acoustic, optical and ionized impurity phonon scattering. The S values for all the samples in this group corresponds very well with $\lambda=0$, indicating that the acoustic phonon scattering is the dominating scattering mechanism.

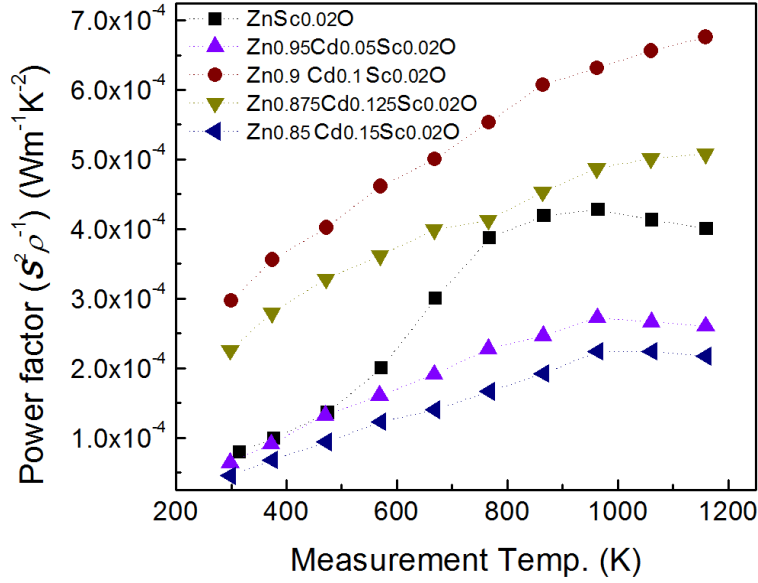


Fig. 6.14 Temperature dependence of power factor for $Zn_{1-x}Cd_xSc_{0.02}O$ ($x = 0$ to 0.15) samples.

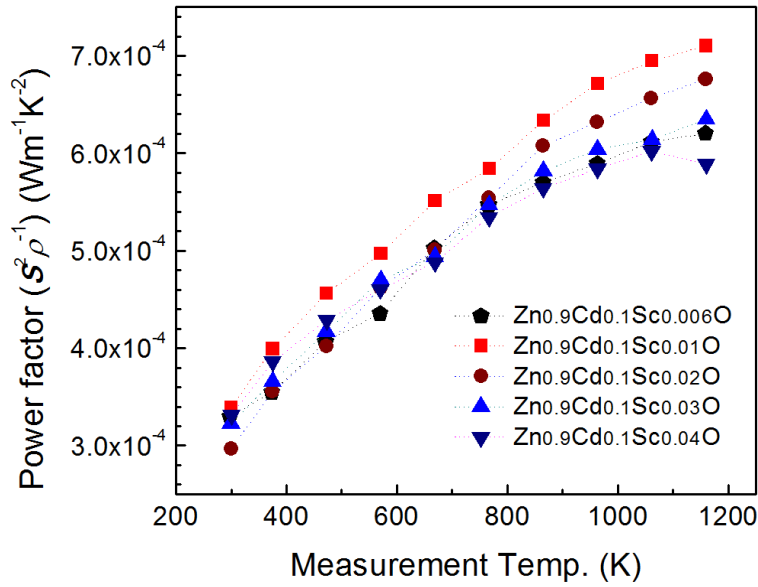


Fig. 6.15 Temperature dependence of power factor for $Zn_{0.9}Cd_{0.1}Sc_yO$ ($y = 0.006$ to 0.04) samples.

Fig. 6.14 shows the calculated power factor ($S^2\rho^{-1}$) for the $Zn_{1-x}Cd_xSc_{0.02}O$ ($x = 0$ to 0.15) samples. The overall $S^2\rho^{-1}$ values increased with increasing Cd concentration and reached highest for $Zn_{0.9}Cd_{0.1}Sc_{0.02}O$. The further increase of Cd concentrations resulted in the decrease of the $S^2\rho^{-1}$.

Fig. 6.15 shows the calculated power factor ($S^2\rho^{-1}$) for the $Zn_{0.9}Cd_{0.1}Sc_yO$ ($y = 0.006$ to 0.04) samples. The $Zn_{0.9}Cd_{0.1}Sc_{0.01}O$ sample has the highest power factor of $\sim 7.1 \times 10^{-4} \text{ Wm}^{-1} \text{K}^{-2}$ at 1173 K which is comparable to the Al doped ZnO[7,56]. The other samples in this group have lower $S^2\rho^{-1}$ values, but the differences are not as pronounced as varying the Cd concentrations as shown in Fig. 6.14.

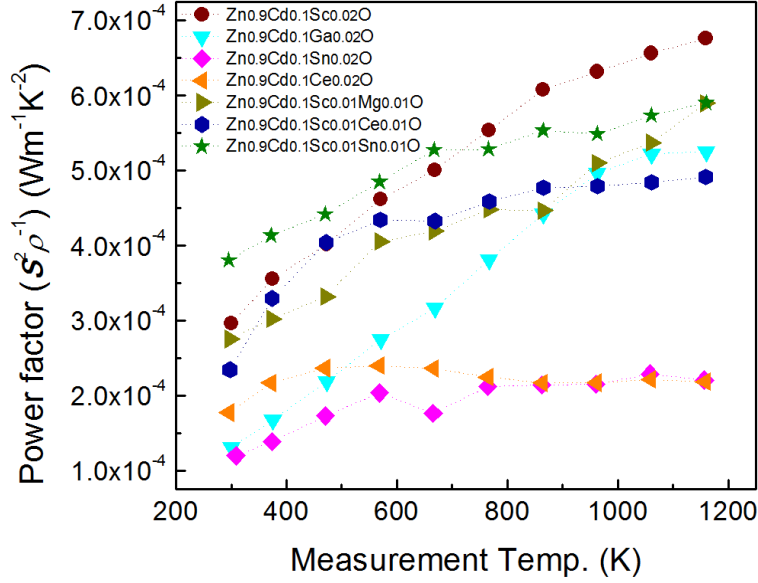


Fig. 6.16 Temperature dependence of power factor for $\text{Zn}_{0.9}\text{Cd}_{0.1}\text{A}_{0.02}\text{O}$ ($\text{A} = \text{Sc}, \text{Ga}, \text{Sn}, \text{Ce}$) and $\text{Zn}_{0.9}\text{Cd}_{0.1}\text{Sc}_{0.01}\text{B}_{0.02}\text{O}$ ($\text{B} = \text{Mg}, \text{Sn}, \text{Ce}$) samples.

Fig. 6.16 shows the calculated power factor ($S^2\rho^{-1}$) for the $\text{Zn}_{0.9}\text{Cd}_{0.1}\text{A}_{0.02}\text{O}$ ($\text{A} = \text{Sc}, \text{Ga}, \text{Sn}, \text{Ce}$) and the $\text{Zn}_{0.9}\text{Cd}_{0.1}\text{Sc}_{0.01}\text{B}_{0.02}\text{O}$ ($\text{B} = \text{Mg}, \text{Sn}, \text{Ce}$) samples. The $\text{Zn}_{0.9}\text{Cd}_{0.1}\text{Sn}_{0.02}\text{O}$ and the $\text{Zn}_{0.9}\text{Cd}_{0.1}\text{Ce}_{0.02}\text{O}$ samples show much lower $S^2\rho^{-1}$ than the others due to their low ρ . Despite the fact that the $\text{Zn}_{0.9}\text{Cd}_{0.1}\text{Ga}_{0.02}\text{O}$ sample has higher electrical conductivity, the $S^2\rho^{-1}$ of the $\text{Zn}_{0.9}\text{Cd}_{0.1}\text{Ga}_{0.02}\text{O}$ is not higher than the $\text{Zn}_{0.9}\text{Cd}_{0.1}\text{Sc}_{0.02}\text{O}$ sample. The multi-doped materials $\text{Zn}_{0.9}\text{Cd}_{0.1}\text{Sc}_{0.01}\text{B}_{0.02}\text{O}$ ($\text{B} = \text{Mg}, \text{Sn}, \text{Ce}$) showed slightly lower $S^2\rho^{-1}$ than that of the $\text{Zn}_{0.9}\text{Cd}_{0.1}\text{Sc}_{0.02}\text{O}$ sample.

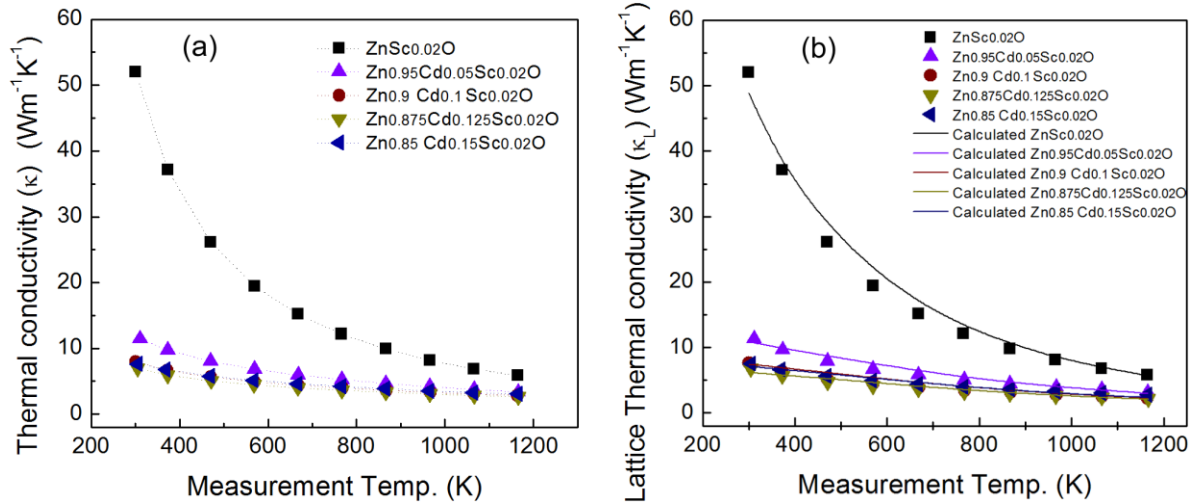


Fig. 6.17 (a) Temperature dependence of total thermal conductivity for $\text{Zn}_{1-x}\text{Cd}_x\text{Sc}_{0.02}\text{O}$ ($x = 0$ to 0.15) samples. (b) Temperature dependence of lattice thermal conductivity of the samples. The solid color lines are the calculated values using the Debye-Callaway model.

Fig. 6.17 (a) shows the thermal conductivity as a function of temperature for $\text{Zn}_{1-x}\text{Cd}_x\text{Sc}_{0.02}\text{O}$ ($x = 0$ to 0.15). The $\text{ZnSc}_{0.02}\text{O}$ sample has high thermal conductivity similar to that of pure ZnO and Al-doped ZnO [35]. As seen from this figure, the existence of Cd in ZnO is remarkably effective for the reduction of the thermal conductivity. The $\text{Zn}_{0.95}\text{Cd}_{0.05}\text{Sc}_{0.02}\text{O}$ sample show 7-fold smaller thermal conductivity than that of $\text{ZnSc}_{0.02}\text{O}$ sample. As the Cd concentration increased, the thermal conductivity continued to decrease to a minimum of $\sim 2.5 \text{ Wm}^{-1}\text{K}^{-1}$ at 1173K for the $\text{Zn}_{0.875}\text{Cd}_{0.125}\text{Sc}_{0.02}\text{O}$ sample. The further increase of Cd had a reverse trend for thermal conductivity, presumably due to the phase separation. These small κ values obtained by $\text{Zn}_{0.875}\text{Cd}_{0.125}\text{Sc}_{0.02}\text{O}$ sample without nanostructuring are comparable or even smaller to those previously reported for the Al-doped ZnO nanocomposites (κ values between 2 to $3.5 \text{ Wm}^{-1}\text{K}^{-1}$ at 1173 K) [7,52–54].

The lattice contribution κ_L to the total κ was estimated using a reduced Lorenz number of $1.8 \times 10^{-8} \text{ W}\Omega\text{K}^{-2}$. The extracted κ_L values are shown in Fig. 6.17 (b). The values of κ_L are somehow similar to the values of κ , indicating that the lattice component dominates the thermal conductivity for all the samples. The Debye-Callaway model [105–107,117] was used to calculate the lattice thermal conductivity as follows:

$$\kappa_L = \frac{k_B}{2\pi^2\nu} \left(\frac{k_B T}{\hbar}\right)^3 \left\{ \int_0^{\theta/T} \frac{\tau_c x^4 e^x}{(e^x - 1)^2} dx + \frac{\left[\int_0^{\theta/T} \frac{x^4 e^x}{\tau_N (e^x - 1)^2} dx \right]^2}{\int_0^{\theta/T} \frac{1}{\tau_N} \left(1 - \frac{\tau_C}{\tau_N}\right) \frac{\tau_c x^4 e^x}{(e^x - 1)^2} dx} \right\} \quad (6.4)$$

where k_B is Boltzmann constant, ν is the speed of sound, \hbar is reduced Planck's constant, x is the normalized frequency $\hbar\omega/k_B T$, T is the absolute temperature, θ is the Debye temperature. τ_c is the combine relaxation time using Matthiessen's rule as follows:

$$\tau_c^{-1} = \tau_{pd}^{-1} + \tau_N^{-1} + \tau_B^{-1} \quad (6.5)$$

where τ_c is composed of alloy point defect scattering τ_{pd} , normal phonon-phonon scattering τ_N , boundary scattering τ_B . The relaxation time for these scattering mechanisms is calculated from the following relations:

$$\tau_{pd}^{-1} = A\omega^4 = \alpha T^4 x^4 \quad (6.6)$$

$$\tau_N^{-1} = BT^3\omega^2 = \beta T^5 x^2 \quad (6.7)$$

$$\tau_B^{-1} = \nu/L \quad (6.8)$$

where A , B , α and β are scattering strength related parameters, ω is phonon frequency, L is the average grain size values. The values used for the calculations are listed in the following Table 6.4. The calculated values are shown as solid lines in Fig. 6.17 (b), agreeing well with the experimental data. The calculations indicated that the reduction of the thermal conductivity was mainly caused by the point defect scattering, indicating that the CdO addition forms oxide alloys with ZnO . The grain size has also an influence on the reduction of the thermal conductivity, but the influence is quite small compared with alloy scattering.

Table 6.4 Parameters used in Callaway calculations for $\text{Zn}_{1-x}\text{Cd}_x\text{Sc}_{0.02}\text{O}$ ($x = 0$ to 0.15).

| | $\text{ZnSc}_{0.02}\text{O}$ | $\text{Zn}_{0.95}\text{Cd}_{0.05}\text{Sc}_{0.02}\text{O}$ | $\text{Zn}_{0.9}\text{Cd}_{0.1}\text{Sc}_{0.02}\text{O}$ | $\text{Zn}_{0.875}\text{Cd}_{0.125}\text{Sc}_{0.02}\text{O}$ | $\text{Zn}_{0.85}\text{Cd}_{0.15}\text{Sc}_{0.02}\text{O}$ |
|-------------------------------------|------------------------------|--|--|--|--|
| $\alpha/\text{K}^{-4}\text{s}^{-1}$ | 230 | 1600 | 3200 | 3900 | 2900 |
| $\beta/\text{K}^{-5}\text{s}^{-1}$ | 0.015 | 0.015 | 0.015 | 0.015 | 0.015 |
| L/m | 1×10^{-5} | 3×10^{-6} | 4.5×10^{-6} | 4×10^{-6} | 3×10^{-6} |

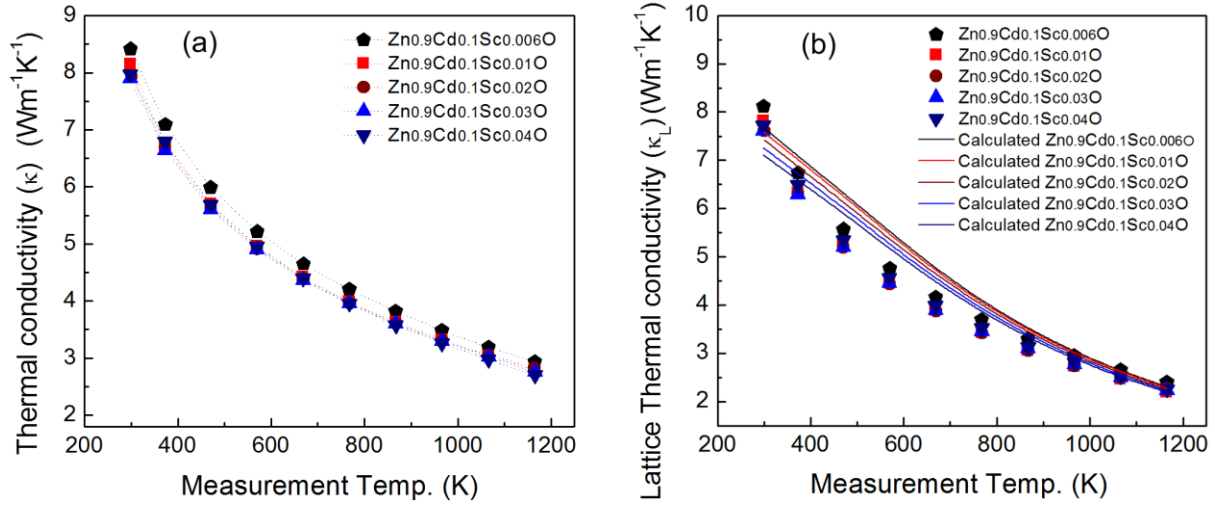


Fig. 6.18 Temperature dependence of the lattice thermal conductivity for $\text{Zn}_{0.9}\text{Cd}_{0.1}\text{Sc}_y\text{O}$ ($y = 0.006$ to 0.04) samples. (b) Temperature dependence of lattice thermal conductivity of the samples. The solid color lines are the calculated values using the Debye-Callaway model.

Fig. 6.18 (a) shows the thermal conductivity as a function of temperature for $\text{Zn}_{0.9}\text{Cd}_{0.1}\text{Sc}_y\text{O}$ ($y = 0.006$ to 0.04) samples. The variation of Sc concentration in this range has a small impact on the thermal conductivity. All the samples in the group have comparable thermal conductivities to that of the $\text{Zn}_{0.9}\text{Cd}_{0.1}\text{Sc}_{0.02}\text{O}$ sample. As the Sc concentration increased, the thermal conductivity slightly decreased and the lowest κ was obtained by the $\text{Zn}_{0.9}\text{Cd}_{0.1}\text{Sc}_{0.04}\text{O}$ sample.

The lattice contribution κ_L to the total κ was estimated and shown in Fig. 6.18 (b). The values of κ_L are still similar to the values of the total conductivity, κ . The calculated values are shown as solid lines in Fig. 6.18 (b). The values used for the calculations are listed in Table 6.5.

Table 6.5 Parameters used in Callaway calculations for $\text{Zn}_{0.9}\text{Cd}_{0.1}\text{Sc}_y\text{O}$ ($y = 0.006$ to 0.04) samples.

| | $\text{Zn}_{0.9}\text{Cd}_{0.1}\text{Sc}_{0.006}\text{O}$ | $\text{Zn}_{0.9}\text{Cd}_{0.1}\text{Sc}_{0.01}\text{O}$ | $\text{Zn}_{0.9}\text{Cd}_{0.1}\text{Sc}_{0.02}\text{O}$ | $\text{Zn}_{0.9}\text{Cd}_{0.1}\text{Sc}_{0.03}\text{O}$ | $\text{Zn}_{0.9}\text{Cd}_{0.1}\text{Sc}_{0.04}\text{O}$ |
|-------------------------------------|---|--|--|--|--|
| $\alpha/\text{K}^{-4}\text{s}^{-1}$ | 3050 | 3100 | 3200 | 3300 | 3400 |
| $\beta/\text{K}^{-5}\text{s}^{-1}$ | 0.015 | 0.015 | 0.015 | 0.015 | 0.015 |
| L/m | 5×10^{-6} | 5×10^{-6} | 4.5×10^{-6} | 4×10^{-6} | 3.5×10^{-6} |

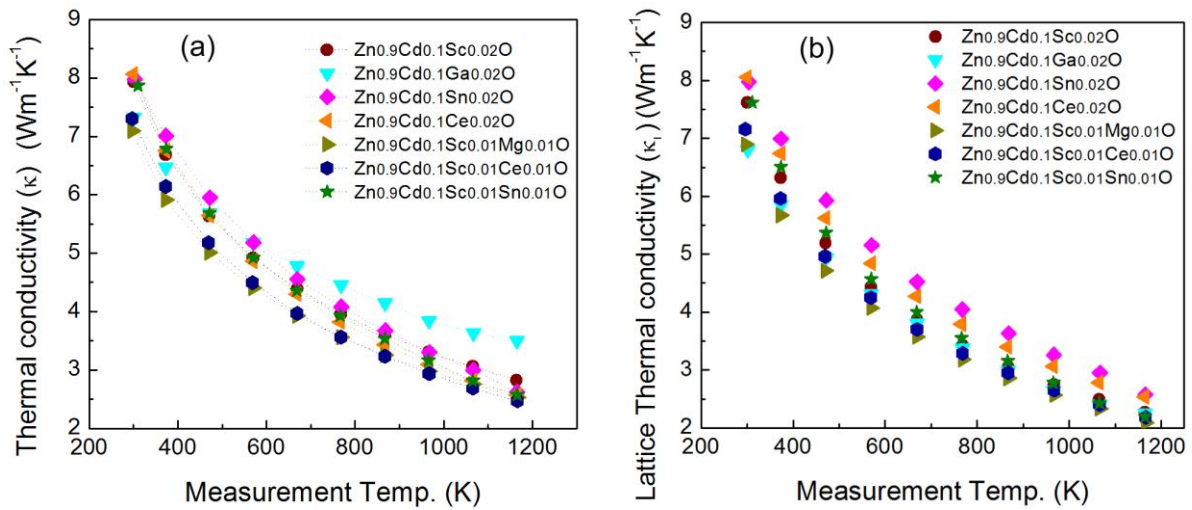


Fig. 6.19 (a) Temperature dependence of total thermal conductivity for $\text{Zn}_{0.9}\text{Cd}_{0.1}\text{A}_{0.02}\text{O}$ ($\text{A} = \text{Sc}, \text{Ga}, \text{Sn}, \text{Ce}$) and $\text{Zn}_{0.9}\text{Cd}_{0.1}\text{Sc}_{0.01}\text{B}_{0.02}\text{O}$ ($\text{B} = \text{Mg}, \text{Sn}, \text{Ce}$) samples. (b) Temperature dependence of lattice thermal conductivity of the samples.

Fig. 6.19 (a) shows the thermal conductivity as a function of temperature for the $\text{Zn}_{0.9}\text{Cd}_{0.1}\text{A}_{0.02}\text{O}$ ($\text{A} = \text{Sc}, \text{Ga}, \text{Sn}, \text{Ce}$) and the $\text{Zn}_{0.9}\text{Cd}_{0.1}\text{Sc}_{0.01}\text{B}_{0.02}\text{O}$ ($\text{B} = \text{Mg}, \text{Sn}, \text{Ce}$) samples. The $\text{Zn}_{0.9}\text{Cd}_{0.1}\text{Ga}_{0.02}\text{O}$ sample has higher thermal conductivity than other samples especially at high temperature. The multi-doped samples have lower thermal conductivity than the $\text{Zn}_{0.9}\text{Cd}_{0.1}\text{Sc}_{0.02}\text{O}$ sample. The κ_L values are shown in Fig. 6.19 (b). The κ_L for $\text{Zn}_{0.9}\text{Cd}_{0.1}\text{Ga}_{0.02}\text{O}$ sample is notably lower than its total κ , suggesting a contribution from electronic thermal conductivity. The multi-doped samples still have lower lattice thermal conductivity than the other $\text{Zn}_{0.9}\text{Cd}_{0.1}\text{A}_{0.02}\text{O}$ ($\text{A} = \text{Sc}, \text{Ga}, \text{Sn}, \text{Ce}$) samples.

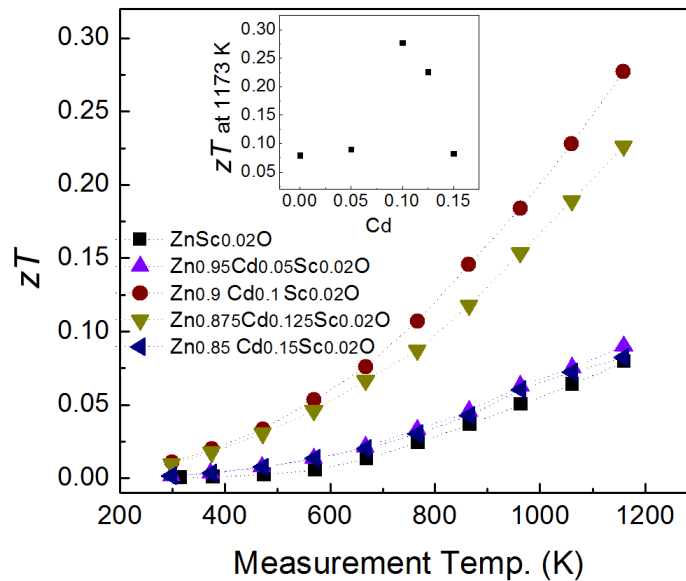


Fig. 6.20 Temperature dependence of figure-of-merit, zT , for $\text{Zn}_{1-x}\text{Cd}_x\text{Sc}_{0.02}\text{O}$ ($x = 0$ to 0.15) samples.

The zT values for $Zn_{1-x}Cd_xSc_{0.02}O$ ($x = 0$ to 0.15) samples are shown in Fig. 6.20. The $ZnSc_{0.02}O$ sample without Cd obtained very low zT even lower than our previous results for the Al doped ZnO[56]. However, as Cd concentration increased, the $Zn_{0.9}Cd_{0.1}Sc_{0.02}O$ sample showed the highest zT in this group. The inset in Fig 6.20 shows the tendency of zT values at 1173 K as Cd concentration changed from 0 to 0.15. The sample with Cd concentration higher than 0.1 generally suffered from deterioration of electrical transportation properties due to the phase separation thus resulted in lower zT .

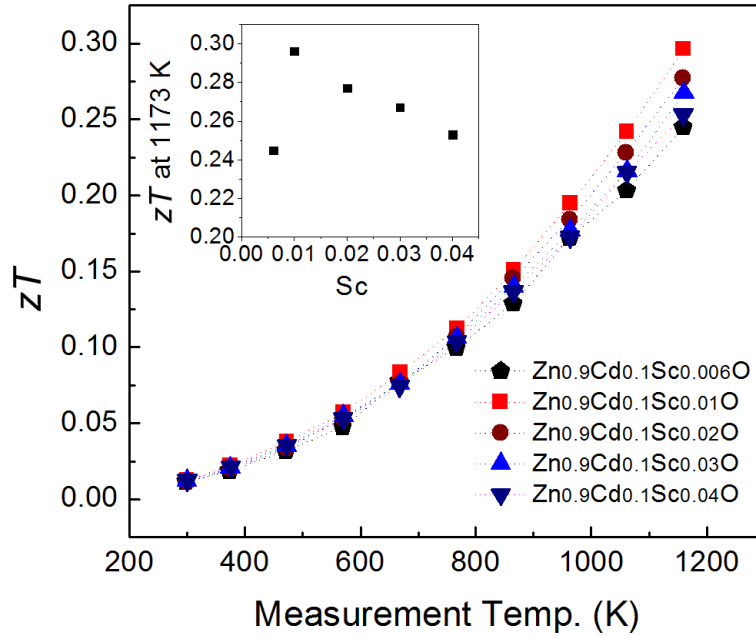


Fig. 6.21 Temperature dependence of figure-of-merit, zT , for $Zn_{0.9}Cd_{0.1}Sc_yO$ ($y = 0.006$ to 0.04) samples.

Figure 6.21 show the zT vs. temperature when keeping the amount of Cd constant at 0.1 for the $Zn_{0.9}Cd_{0.1}Sc_yO$ ($y = 0.006$ to 0.04) samples. The variation of Sc concentration in this range has relatively small impact on the zT values. All the samples in the group have a comparable zT values. Still, the $Zn_{0.9}Cd_{0.1}Sc_{0.01}O$ sample obtained the highest overall zT values and a zT value of 0.3 at 1173 K.

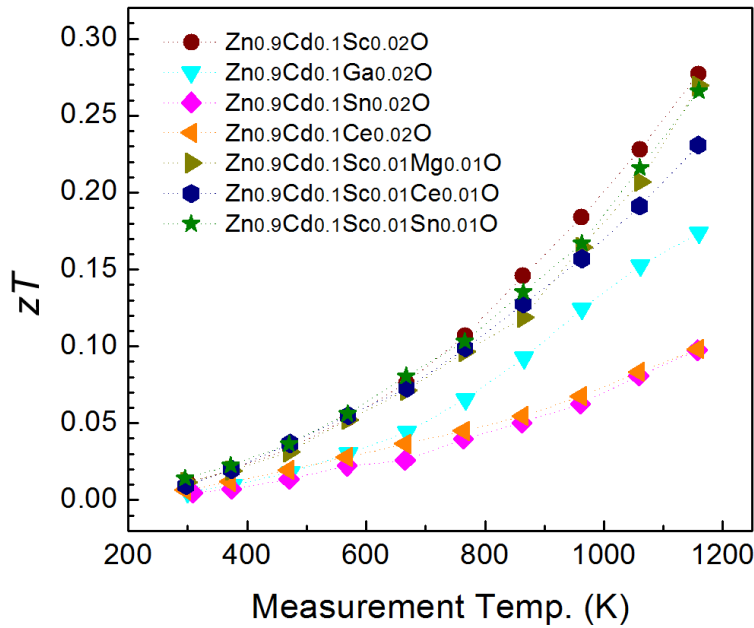


Fig. 6.22 Temperature dependence of figure-of-merit, zT , for $Zn_{0.9}Cd_{0.1}A_{0.02}O$ ($A = Sc, Ga, Sn, Ce$) and $Zn_{0.9}Cd_{0.1}Sc_{0.01}B_{0.02}O$ ($B = Mg, Sn, Ce$) samples.

The zT values for $Zn_{0.9}Cd_{0.1}A_{0.02}O$ ($A = Sc, Ga, Sn, Ce$) and $Zn_{0.9}Cd_{0.1}Sc_{0.01}B_{0.02}O$ ($B = Mg, Sn, Ce$) samples are shown in Fig. 6.22. The Sc doped samples showed superior zT values than the other samples in this group. The multi-doped samples didn't obtain higher zT than the $Zn_{0.9}Cd_{0.1}Sc_{0.02}O$ sample, meaning that other and better dopants and concentrations for this system are still needed to be explored in the future

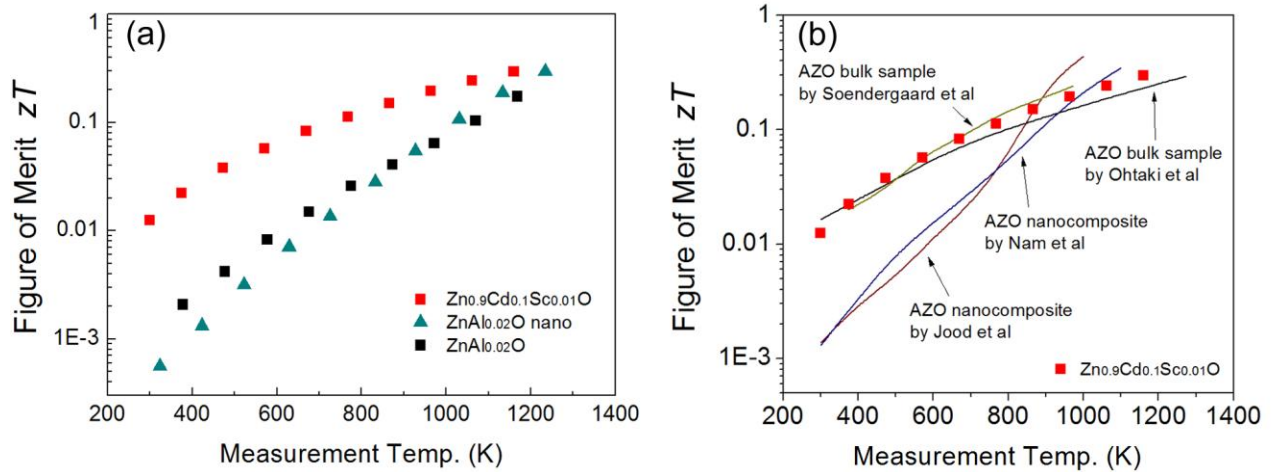


Fig. 6.23 Comparing the zT of $Zn_{0.9}Cd_{0.1}Sc_{0.01}O$ to (a) our previous results on Al doped ZnO[7,56]. (b) Al doped ZnO from literature results[10,35,52,53].

A comparison of zT values in the current work and our previous results on Al-doped ZnO is shown in Fig. 6.23 (a). The new developed $Zn_{0.9}Cd_{0.1}Sc_{0.01}O$ has far superior zT values than Al doped ZnO all over the temperature range in despite of the absence of nanostructuring. Its zT value at ~ 300 K is over 1 order of magnitude higher than the nanostructured Al-doped ZnO.

Comparison between the zT of the Al-doped ZnO reported in the literature and the $\text{Zn}_{0.9}\text{Cd}_{0.1}\text{Sc}_{0.01}\text{O}$ is shown in Figure 6.23 (b). As seen from this figure, the $\text{Zn}_{0.9}\text{Cd}_{0.1}\text{Sc}_{0.01}\text{O}$ has so far one of the highest zT values among the Al-doped ZnO materials. This suggests that this material is a possible good candidate for improving the overall conversion efficiencies in thermoelectric module.

6.3.3 Thermoelectric stability in air

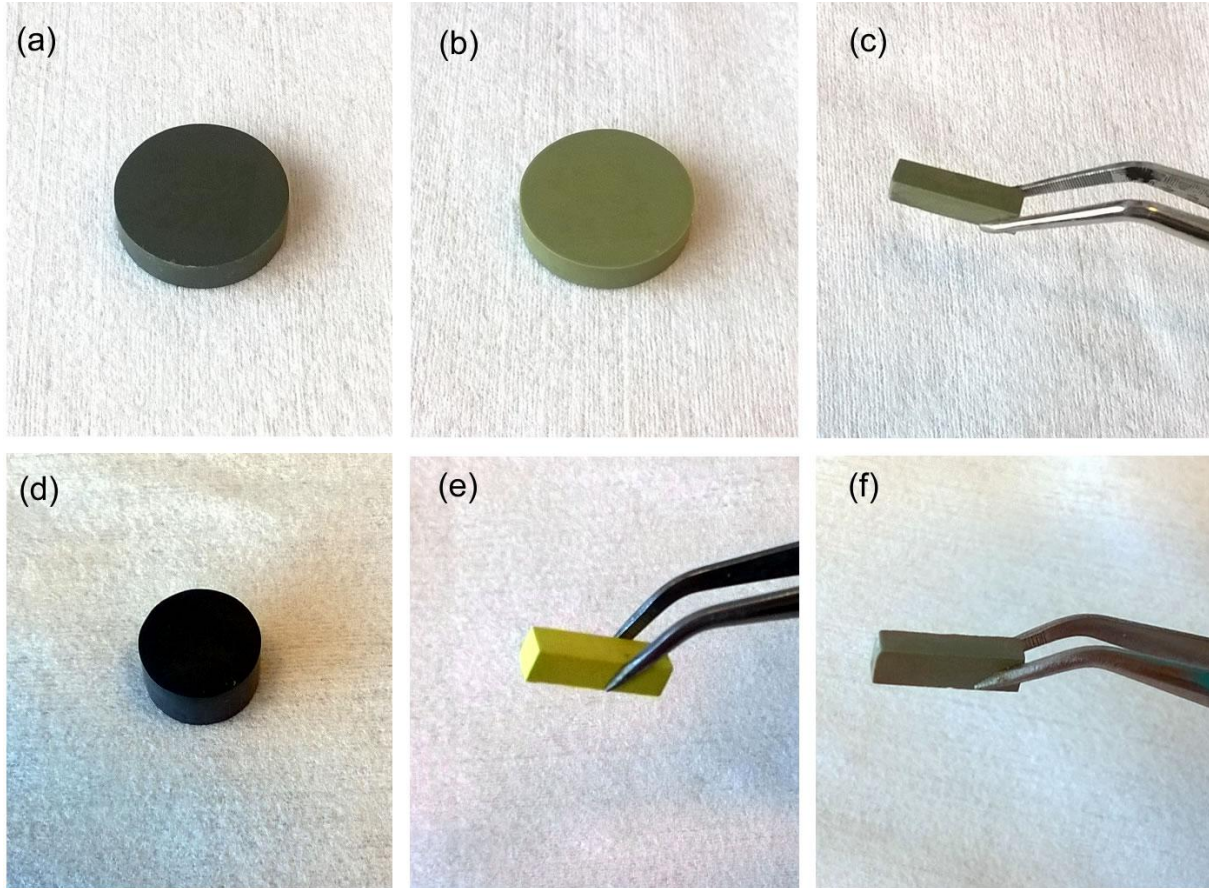


Fig. 6.24 Photographs of (a) a bulk pellet of $\text{Zn}_{0.9}\text{Cd}_{0.1}\text{Ga}_{0.02}\text{O}$ sintered in air, (b) a bulk pellet of $\text{Zn}_{0.9}\text{Cd}_{0.1}\text{Sc}_{0.02}\text{O}$ sintered in air, (c) a hexagonal segment cut from the pellet of $\text{Zn}_{0.9}\text{Cd}_{0.1}\text{Sc}_{0.02}\text{O}$, (d) a bulk pellet of $\text{Zn}_{0.98}\text{Al}_{0.02}\text{O}$ sintered by Spark Plasma Sintering in vacuum, (e) a hexagonal segment of $\text{ZnAl}_{0.02}\text{O}$ after annealing in air at 1073K for 72h, (f) a hexagonal segment of $\text{Zn}_{0.9}\text{Cd}_{0.1}\text{Sc}_{0.02}\text{O}$ after annealing in air at 1073K for 72h.

The new Sc doped ZnCdO materials has not only the superior zT values than the state-of-the-art Al-doped ZnO, but more importantly it has much better long-term stability in air at high temperatures, where the current state-of-the-art e.g. Al-doped ZnO is not suitable. The degradation of Al-doped ZnO is mainly due to the recovering of oxygen vacancies and can be simply observed by the changes of the samples color. Fig. 6.24 shows the photographs of the new materials of $\text{Zn}_{0.9}\text{Cd}_{0.1}\text{Ga}_{0.02}\text{O}$ and $\text{Zn}_{0.9}\text{Cd}_{0.1}\text{Sc}_{0.02}\text{O}$ sintered in air (see Fig. 6.25 (a) and (b)). On the other hand the $\text{Zn}_{0.98}\text{Al}_{0.02}\text{O}$ sample appeared dark colored after SPS in vacuum, but after

annealing in air at 1073 K for 72h, the segments turned light yellow, indicating a significant change in its electrical properties (see Fig. 6.25 (d) and (e)). In contrast, the $\text{Zn}_{0.9}\text{Cd}_{0.1}\text{Sc}_{0.02}\text{O}$ sample sintered in air remained its dark greenish color after annealing in air at 1073K for 72h (see Fig. 6.25 (c) and (f)).

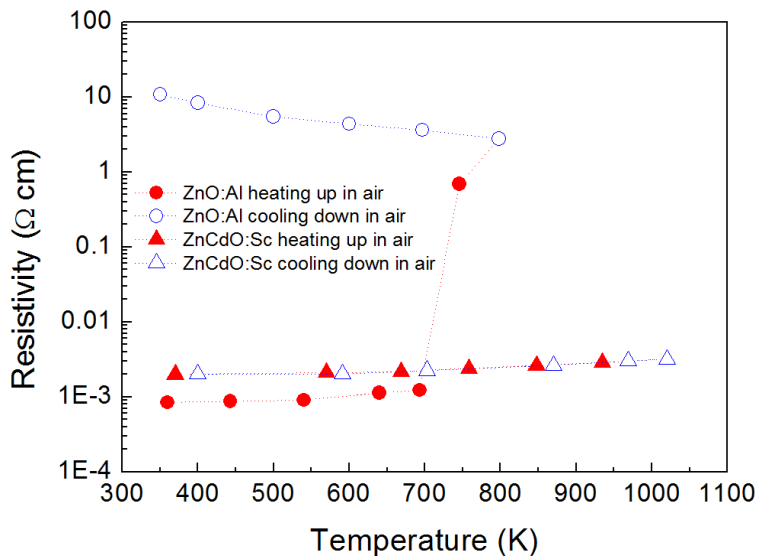


Fig. 6.25 Resistivity of $\text{Zn}_{0.9}\text{Cd}_{0.1}\text{Sc}_{0.02}\text{O}$ and $\text{ZnAl}_{0.02}\text{O}$ measured in air.

To testify the thermal stability of the new material, a measurement of the resistivity in air was performed for the $\text{Zn}_{0.9}\text{Cd}_{0.1}\text{Sc}_{0.02}\text{O}$ and the $\text{Zn}_{0.98}\text{Al}_{0.02}\text{O}$ samples. Fig. 6.25 shows the rather stable electrical resistivity of $\text{Zn}_{0.9}\text{Cd}_{0.1}\text{Sc}_{0.02}\text{O}$ sample compared with the unstable resistivity of $\text{Zn}_{0.98}\text{Al}_{0.02}\text{O}$ sample when cycled in air up to 1073 K. The heating up and cooling down sequence took about 24 hours in total.

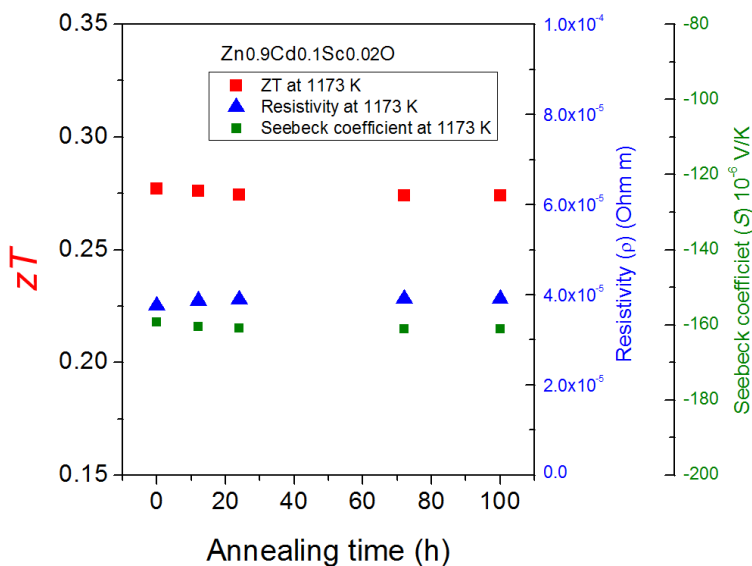


Fig. 6.26 Time dependence of zT values, resistivity and Seebeck coefficient at 1173 K for $\text{Zn}_{0.9}\text{Cd}_{0.1}\text{Sc}_{0.02}\text{O}$ sample after annealing in air at 1073 K.

The long-term stability for $\text{Zn}_{0.9}\text{Cd}_{0.1}\text{Sc}_{0.02}\text{O}$ sample was tested by annealing the sample in air at 1073 K for a certain period of time and mounts it in ZEM-3 to measure the electrical properties. The lattice thermal conductivity changes are neglected in this case due to the fact that the sample was sintered in 1673 K. The time dependence of zT values, resistivity and Seebeck coefficient at 1173 K was recorded as shown in Fig.6.26. The zT degradation was $\sim 2\%$ after 100 hours of annealing in air.

6.4 Conclusions

A systematic investigation was performed for the thermoelectric properties of a newly developed doped Zinc Cadmium Oxide materials ($\text{Zn}_{1-x}\text{Cd}_x\text{A}_y\text{O}$, A = Sc, Ga, Ce, Mg, Sn etc.). The Sc-doped ZnCdO with the composition $\text{Zn}_{0.9}\text{Cd}_{0.1}\text{Sc}_{0.01}\text{O}$ obtained the highest $zT \sim 0.3$ @1173 K, ~ 0.24 @1073 K, and a good average zT which is better than the nanostructured AZO materials. The superior zT values can be attributed to the alloying of CdO with ZnO and resulted in the significant reduction of lattice thermal conductivity. The electrical transport properties were maintained the same after alloying. Through careful selection of dopants and dopant concentrations, a large power factor of $\sim 7.1 \times 10^{-4} \text{ Wm}^{-1}\text{K}^{-1}$ was obtainable. Meanwhile, Sc-doped ZnCdO is robust in air at high temperatures up to 1073 K, and its thermoelectric performance maintains after multi heating and cooling cycles in air, while other n-type materials such as Al, Ga-doped ZnO or STO will experience rapid degradation on thermoelectric performances. Overall, the Sc-doped ZnCdO material is a new and promising n-type material with superior properties for high temperature thermoelectric applications.

Chapter 7 Conclusions and Outlooks

7.1 The doping mechanisms and thermoelectric properties of Al-doped ZnO

Al has a limited solubility in ZnO of a value below 1 at%, and the formation of the secondary phase ZnAl_2O_4 is chemically favored from room temperature to a temperature above 1673 K. By using different phases such as $\alpha\text{-Al}_2\text{O}_3$ and $\gamma\text{-Al}_2\text{O}_3$ as dopants for ZnO, the doping mechanism of Al into ZnO was investigated by examining the incorporation of Al into ZnO and the formation of ZnAl_2O_4 secondary phases.

The ZnAl_2O_4 formation rate is kinetically controlled by a two-way solid state diffusion between the ZnO and the Al_2O_3 . The formation of ZnAl_2O_4 is only caused by the diffusion of Zn to Al_2O_3 , while the Al substitution for Zn results from the diffusion of Al into ZnO. The disordered structure of $\gamma\text{-Al}_2\text{O}_3$ may lead to the disordered product layers of ZnAl_2O_4 . The Al and Zn ions can easier diffuse through the disordered product layer. It promotes both the formation of ZnAl_2O_4 and the substitutions of Al for Zn as donor impurities in ZnO.

At a given calcinations temperature, the addition of $\gamma\text{-Al}_2\text{O}_3$ resulted in a larger fraction of the ZnAl_2O_4 formation in the Al-doped ZnO samples, which also inhibited the grain growth and slightly reduced the lattice thermal conductivity. The higher diffusion rate of Al observed for the $\gamma\text{-Al}_2\text{O}_3$ resulted in a larger unit cell volume shrinkage and higher electrical conductivity as compared with the $\alpha\text{-Al}_2\text{O}_3$ -doped ZnO. As a consequence, $\gamma\text{-Al}_2\text{O}_3$ -doped ZnO exhibited a higher zT than the $\alpha\text{-Al}_2\text{O}_3$ -doped counterpart under the same preparation conditions with calcination temperatures lower than 1273 K.

7.2 SPS densification mechanisms and thermoelectric properties of Al, Ga-dually doped ZnO

The SPS densification for Al, Ga dually-doped ZnO was investigated. The simulation of self-Joule-heating effect of the particles indicated that, the pulsed current applied to the sample result in rather high temperature increase near the particles contacts which strongly promoted the sintering of the particles.

In this work, Al, Ga dually-doped ZnO was prepared by spark plasma sintering using different sintering profiles and resulted in different relative densities and phase equilibrium. A porous sample sintered at 1073K with low relative density ~89% showed the lowest zT value due to its poor electrical properties in spite of a low thermal conductivity. The dense samples on the other hand which is sintered above 1223K obtained much better zT values than the porous sample. The calculated results of solid-state-reaction completion rate suggested that the sintering temperature above 1223K would be preferable for the complete solid state reaction of the samples. It indicated that not only the relative density, but also the phase equilibrium were very important for realizing stable and decent thermoelectric properties.

7.3 Achieving Low Thermal Conductivity by Nanostructuring for Al-doped ZnO

Nanostructured Al-doped ZnO nanostructured bulk samples were fabricated using precursors with different morphologies and SPS densification. The effect of different microstructure features, such as grain boundaries and secondary phases, on the thermoelectric properties of Al-doped ZnO was investigated. The results showed that the grain boundaries were effective for scattering both phonons and electrons. The samples with anisotropic grain morphologies also exhibited anisotropic electrical and thermal transport properties.

By using the Debye-Callaway model in combination with the experimental observations, the influence of grain boundaries and nanoprecipitates on the heat transport was investigated. The scattering of phonon spectrum turned out to be selective to the microstructure features depending on the length scales. The grain boundaries selectively depress the phonon spectrum at the low frequency region, while the nanoprecipitates with length scale of a few nanometers selectively depress the phonon spectrum at the intermediate and high frequency region. Thus the grain boundaries had limited effect on reducing the thermal conductivity at high temperatures. The reduction could otherwise be achieved by using nanoprecipitates with length scale of a few nanometers. However, both the grain boundaries and nanoprecipitates had a negative effect on the electrical properties. They both decrease the electrical conductivity by decreasing the carrier mobility.

For a nanostructured Al-doped ZnO sample, the low thermal conductivity was successfully achieved by the combination of grain boundaries and nanoprecipitates. However, the zT values were very low at room temperature ($\sim 5.6 \times 10^{-4}$ at 300 K). As carrier mobility increased with increasing temperature, higher zT values than the bulk samples were achieved only at high temperatures.

7.4 Doped ZnCdO material as a promising substitution for conventional ZnO materials.

The ZnO based n-type thermoelectric materials had excellent electrical transport properties among other n-type oxide materials, but the extremely high lattice thermal conductivity and poor thermoelectric stability at high temperatures are the major issues that hindered its real use in applications. Nanostructuring could reduce the thermal conductivity quite effectively, yet the deteriorated electrical conductivity cannot be avoided. Furthermore, the thermoelectric properties are very sensitive to the sintering and measuring atmospheres making this composition difficult to use.

Doped ZnCdO material was developed in this work as a new n-type oxide thermoelectric material. The material is sintered in air in order to maintain the oxygen stoichiometry and avoid the stability issues. The successful alloying of CdO with ZnO at a molar ratio of 1:9 resulted in a significant reduction of thermal conductivity up to 7-fold at room temperature. By careful

selection of the dopants and dopant concentrations, a large power factor was obtainable. The optimized sample with the composition of $\text{Zn}_{0.9}\text{Cd}_{0.1}\text{Sc}_{0.01}\text{O}$ obtained the highest $zT \sim 0.3$ @1173 K and ~ 0.24 @1073K which are better values than the state-of-the-art n-type thermoelectric oxide materials. Meanwhile, Sc-doped ZnCdO is robust and stable in air at high temperatures, while other n-type materials such as Al, Ga-doped ZnO or STO still experience rapid degradation of their thermoelectric performances in air at high temperature. Overall, the Sc-doped ZnCdO material is a new and promising n-type material with superior properties for high temperature thermoelectric applications.

7.5 Outlook of the future work

ZnO based thermoelectric materials exhibited excellent electrical properties compared with other n-type oxide materials. However its highest zT of ~ 0.3 at 1173K is still far from enough for real applications. Further improving zT may require not only nanostructuring, but also other strategies like alloying and band structure engineering.

The new Sc-doped ZnCdO material is a product of oxide alloying strategy. It solves the problems of high thermal conductivity, low reliability, and deteriorated electrical conductivity by nanostructuring for conventional ZnO materials. However, the use of Cd is a risk for its toxicity issues. A risk assessment and a stricter high temperature long-term stability test should be performed. Meanwhile, the replacement of Cd for other elements should also be considered in the future.

Nevertheless, the knowledge obtained in the research for ZnO based oxide thermoelectric materials is also applicable to many other oxide or non-oxide systems. The constant exploring new materials as thermoelectric candidates is the key to better overall thermoelectric performances, and should never be put in a second place.

Appendix A

The sintering setup, thermophysical and electrical parameters used in the modeling are listed below:

$$d \text{ (sample diameter, m)} = 1.8 \times 10^{-2}$$

$$S_s \text{ (sample cross-sectional area, m}^2\text{)} = 2.54 \times 10^{-4}$$

$$S_d \text{ (sample cross-sectional area, m}^2\text{)} = 7.63 \times 10^{-4}$$

$$\rho_{s1} \text{ (ZnO electrical resistivity, } \Omega \text{ m)} = 5.08512 \times e^{(-T/81.92166)} + 0.000237$$

$$\rho_{s2} \text{ (Zn}_{0.96}\text{Al}_{0.02}\text{Ga}_{0.02}\text{O electrical resistivity, } \Omega \text{ m)} = 2.46 \times 10^{-5} - 4.29 \times 10^{-8}T + 1.05 \times 10^{-10}T^2 - 9.48 \times 10^{-14}T^3 + 3.35 \times 10^{-17}T^4$$

$$\rho_d \text{ (graphite electrical resistivity, } \Omega \text{ m)} = 21 - 3 \times 10^{-2}T + 2 \times 10^{-5}T^2 - 6.4 \times 10^{-9}T^3 + 7.8 \times 10^{-13}T^4$$

$$\Delta t \text{ (current duration, ms)} = 12 \times 3.3 = 39.6$$

$$C_{P,\text{graphite}} \text{ (specific heat capacity at constant pressure of graphite, J/g.K)} = 0.71$$

$$C_{P,\text{ZnO}} \text{ (specific heat capacity at constant pressure of ZnO, J/g.K)} = 0.6181$$

$$\rho_{m \text{ graphite}} \text{ (mass density of graphite, g/m}^3\text{)} = 2.1 \times 10^6$$

$$\rho_{m \text{ ZnO}} \text{ (mass density of ZnO, g/m}^3\text{)} = 5.61 \times 10^6$$

Appendix B

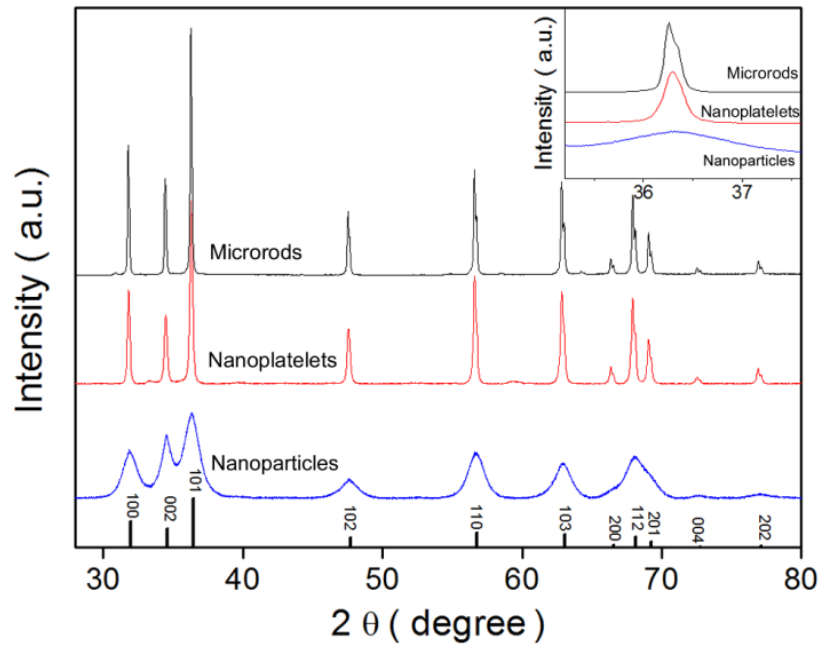


Figure S1. The powder X-ray diffraction pattern of the precursors with different morphologies.

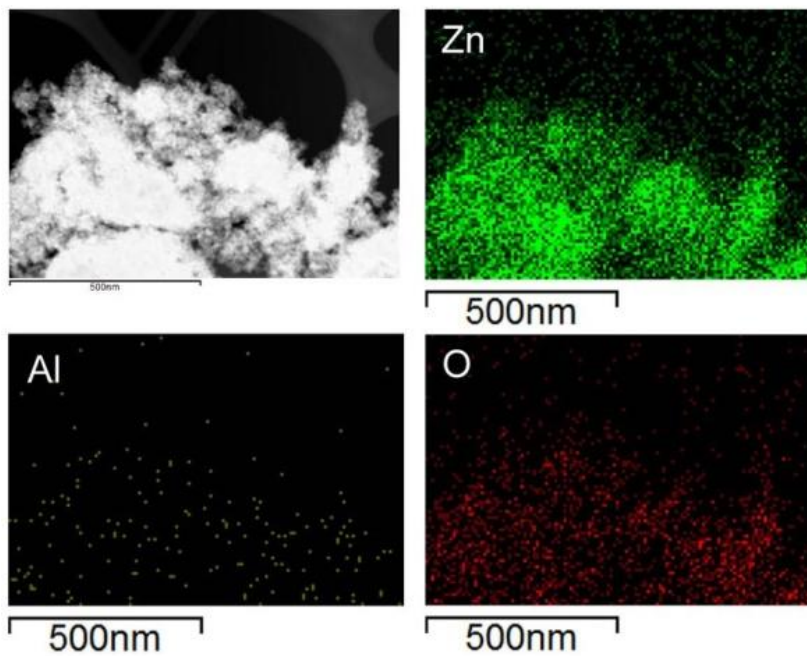


Figure S2. STEM-EDS mapping of the nanoparticles synthesized by forced-hydrolysis method.

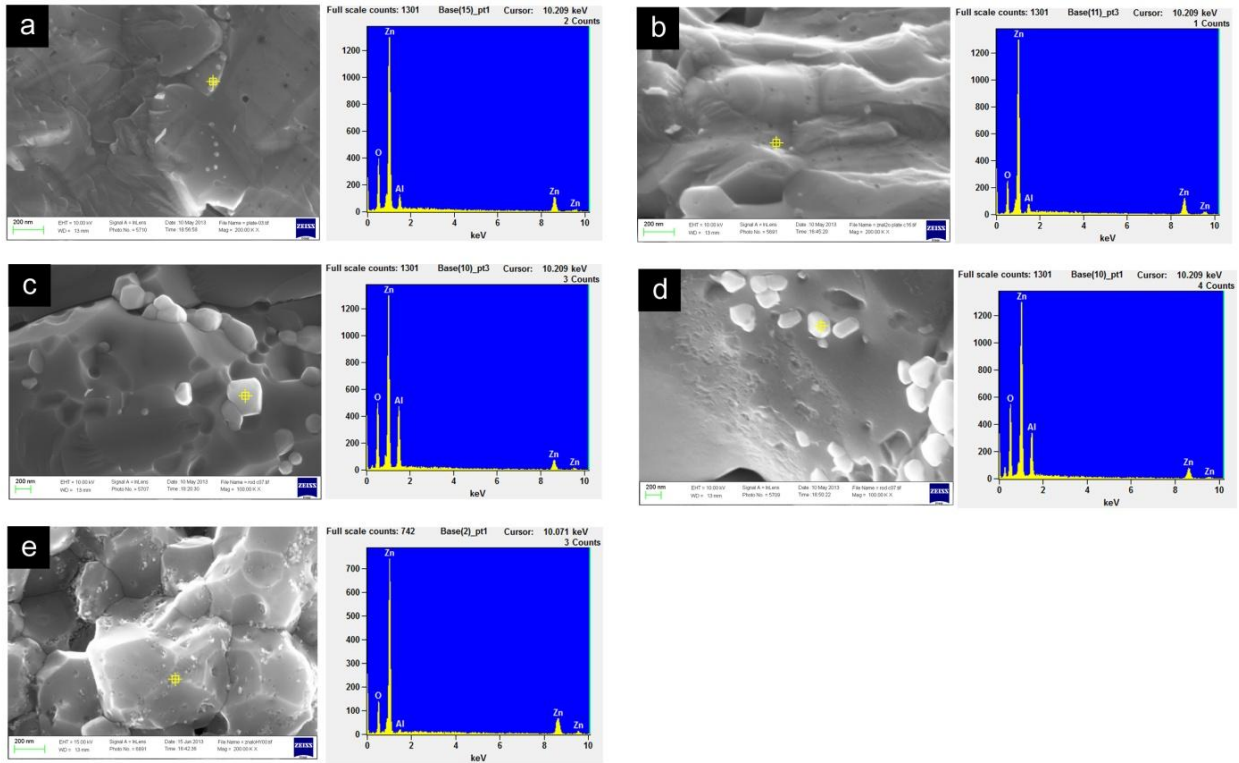


Figure S3. EDS point analysis of the secondary phases dispersed on the fractured surface of (a) Platelet($\perp p$) surface, (b) Platelet($\parallel p$) surface, (c) Rod($\perp p$) surface, (d) Rod($\parallel p$) surface, and (e) Nanoparticle.

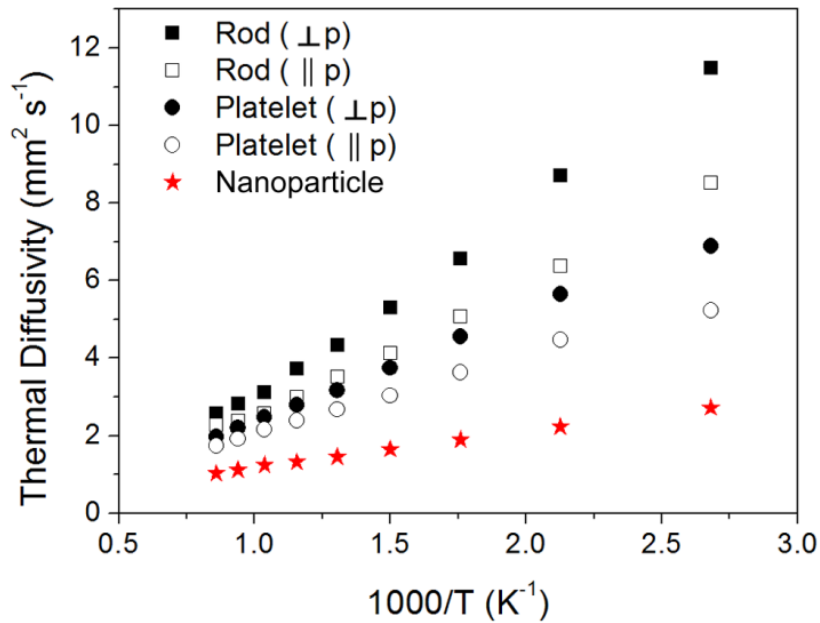


Figure S4. Temperature dependence of thermal diffusivity of the sintered samples measured by LFA.

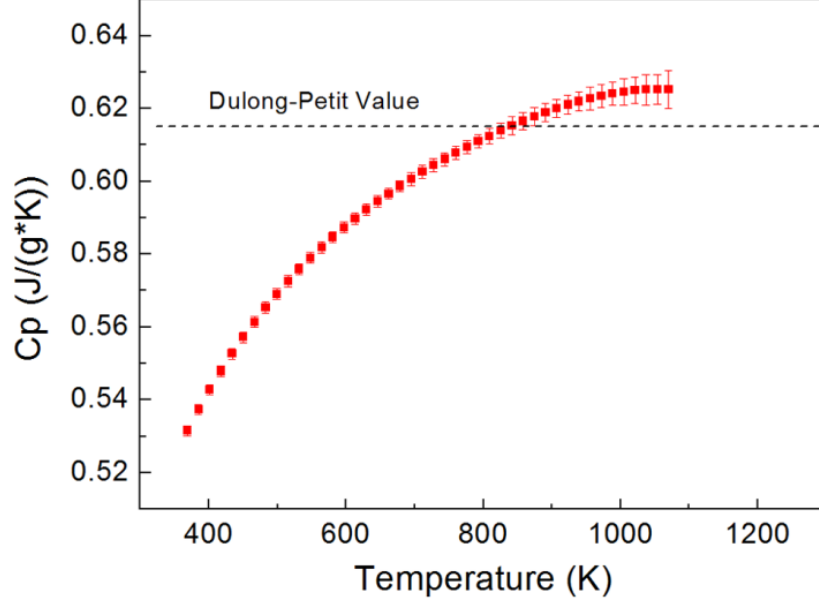


Figure S5. Temperature dependence of the specific heat at constant pressure measured by DSC.

Calculations of The lower limit of thermal conductivity κ_{\min}

The lower limit of thermal conductivity κ_{\min} for $\text{Zn}_{0.98}\text{Al}_{0.02}\text{O}$ was calculated by taking the high-temperature limit of the thermal conductivity calculated by Cahill et al[106] for amorphous material with an average volume per atom given by V .

$$\kappa_{\min} = \frac{1}{2} \left(\frac{\pi}{6} \right)^{\frac{1}{3}} k_B V^{-\frac{2}{3}} (2v_t + v_l) \quad (1)$$

where k_B is Boltzmann constant, v_t and v_l are transverse and longitudinal speed of sound. From the speed of sound measurements, v_t here equals $2750 \text{ m}\cdot\text{s}^{-1}$, and v_l equals $5940 \text{ m}\cdot\text{s}^{-1}$. Thus the κ_{\min} was calculated to be $1.22 \text{ W}\cdot\text{m}^{-1}\cdot\text{K}^{-1}$ as shown in Figure 8 in the main article.

Calculations of The lattice thermal conductivity κ_L

The lattice thermal conductivity is calculated using Debye-Callaway model [105,117] as

follows:

$$\kappa_L = \frac{k_B}{2\pi^2 v} \left(\frac{k_B T}{\hbar} \right)^3 \left\{ \int_0^{\theta/T} \frac{\tau_c x^4 e^x}{(e^x - 1)^2} dx + \frac{\left[\int_0^{\theta/T} \frac{\tau_c x^4 e^x}{\tau_N (e^x - 1)^2} dx \right]^2}{\int_0^{\theta/T} \frac{1}{\tau_N} \left(1 - \frac{\tau_c}{\tau_N} \right) \frac{\tau_c x^4 e^x}{(e^x - 1)^2} dx} \right\} \quad (2)$$

where k_B is Boltzmann constant, v is the speed of sound, \hbar is reduced Planck's constant, x is the normalized frequency $\hbar\omega/k_B T$, T is the absolute temperature, θ is the Debye temperature of $\text{Zn}_{0.98}\text{Al}_{0.02}\text{O}$. τ_c is the combine relaxation time using Matthiessen's rule as follows:

$$\tau_c^{-1} = \tau_{pd}^{-1} + \tau_N^{-1} + \tau_B^{-1} + \tau_D^{-1} \quad (3)$$

where τ_c is composed of point defect scattering τ_{pd} , normal phonon-phonon scattering τ_N , boundary scattering τ_B , and nano-particle scattering τ_D . The relaxation time for these scattering mechanisms is calculated from the following relations:

$$\tau_{pd}^{-1} = A\omega^4 = \alpha T^4 \chi^4 \quad (4)$$

$$\tau_N^{-1} = BT^3\omega^2 = \beta T^5 \chi^2 \quad (5)$$

$$\tau_B^{-1} = v/L \quad (6)$$

where A , B , α and β are scattering strength related parameters, ω is phonon frequency, L is the average grain size values. According to Majumdar's heat transfer theory[107,108], when the particle size is small enough, the scattering cross section obeys Rayleigh law, which varies as frequency to the fourth power. Thus the relaxation time for nanoparticle scattering, τ_D , should be calculated as:

$$\tau_{D(Rayleigh)}^{-1} = \eta v^{-3} (2\pi)^{-4} d^6 \omega^4 = (2\pi)^{-4} \eta v^{-3} d^6 k_B^4 T^4 \hbar^{-4} \chi^4 \quad (7)$$

where η is concentration (m^{-3}). d is the mean nano-particle size. As the size of nano-particle increases, the scattering cross section is near geometric and phonon frequency independent, which is $\sigma_{(\text{geometric})} \sim \pi(d/2)^2$. Thus the relaxation time for nanoparticle scattering, τ_D , should be calculated as:

$$\tau_{D(\text{geometric})}^{-1} = \eta v \pi(d/2)^2 \quad (8)$$

The values used for the calculations are listed in the following Table S1.

Table S1 An overview of the parameters used in Callaway calculations

| Calculation | #1 | #2 | #3 | #4 | #5 |
|---|----------------------|----------------------|--------------------|------------------------|----------------------|
| Sample | Rod (\perp p) | Rod (\parallel p) | Plate (\perp p) | Plate (\parallel p) | Nano |
| θ/K | 400 | 400 | 400 | 400 | 400 |
| v/ms^{-1} | 3097 | 3097 | 3097 | 3097 | 3097 |
| $\alpha/\text{K}^{-4}\text{s}^{-1}$ | 420 | 420 | 400 | 400 | 100 |
| $\beta/\text{K}^{-5}\text{s}^{-1}$ | 0.015 | 0.015 | 0.015 | 0.015 | 0.015 |
| L/m | 1×10^{-5} | 2×10^{-6} | 6×10^{-7} | 1.5×10^{-7} | 4×10^{-7} |
| $\eta_{(\text{geometric})}/\text{m}^{-3}$ | 1.2×10^{17} | 1.2×10^{17} | 1×10^{19} | 1×10^{19} | |
| $d_{(\text{geometric})}/\text{m}$ | 3×10^{-7} | 3×10^{-7} | 3×10^{-8} | 3×10^{-8} | |
| $\eta_{(\text{Rayleigh})}/\text{m}^{-3}$ | | | | | 1.4×10^{20} |
| $d_{(\text{Rayleigh})}/\text{m}$ | | | | | 1×10^{-8} |

References

- [1] Seebeck TJ. Magnetische polarisation der metalle und erze durch temperatur-differenz. *Abh K Akad Wiss* 1823;265.
- [2] Goupil C, Seifert W, Zabrocki K, Müller E, Snyder GJ. Thermodynamics of Thermoelectric Phenomena and Applications. *Entropy* 2011;13:1481–517.
- [3] Kittel C. Introduction to solid state physics. 2005.
- [4] Tritt TM. Thermoelectric Phenomena, Materials, and Applications. *Annu Rev Mater Res* 2011;41:433–48.
- [5] Snyder GJ, Toberer ES. Complex thermoelectric materials. *Nat Mater* 2008;7:105–14.
- [6] Rowe DM. CRC Handbook of Thermoelectrics. New York 1995;16:1251–6.
- [7] Han L, Van Nong N, Zhang W, Hung LT, Holgate T, Tashiro K, et al. Effects of morphology on the thermoelectric properties of Al-doped ZnO. *RSC Adv* 2014;4:12353.
- [8] Lan Y, Minnich AJ, Chen G, Ren Z. Enhancement of Thermoelectric Figure-of-Merit by a Bulk Nanostructuring Approach. *Adv Funct Mater* 2010;20:357–76.
- [9] Biswas K, He J, Blum ID, Wu C-I, Hogan TP, Seidman DN, et al. High-performance bulk thermoelectrics with all-scale hierarchical architectures. *Nature* 2012;489:414–8.
- [10] Jood P, Mehta RJ, Zhang Y, Peleckis G, Wang X, Siegel RW, et al. Al-doped zinc oxide nanocomposites with enhanced thermoelectric properties. *Nano Lett* 2011;11:4337–42.
- [11] Van Nong N, Pryds N, Linderöth S, Ohtaki M. Enhancement of the thermoelectric performance of p-type layered oxide $\text{Ca}_3\text{Co}_4\text{O}_{(9+\delta)}$ through heavy doping and metallic nanoinclusions. *Adv Mater* 2011;23:2484–90.
- [12] Zebarjadi M, Esfarjani K, Dresselhaus MS, Ren ZF, Chen G. Perspectives on thermoelectrics: from fundamentals to device applications. *Energy Environ Sci* 2012;5:5147.
- [13] Dresselhaus MS, Bell LE. Reflections on thermoelectrics. *Nat Nanotechnol* 2013;8:469–469.
- [14] Minnich AJ, Dresselhaus MS, Ren ZF, Chen G. Bulk nanostructured thermoelectric materials: current research and future prospects. *Energy Environ Sci* 2009;2:466.
- [15] Zebarjadi M, Esfarjani K, Dresselhaus MS, Ren ZF, Chen G. Perspectives on thermoelectrics: from fundamentals to device applications. *Energy Environ Sci* 2012;5:5147.

- [16] Dresselhaus MS, Chen G, Tang MY, Yang RG, Lee H, Wang DZ, et al. New directions for low-dimensional thermoelectric materials. *Adv Mater* 2007;19:1043–53.
- [17] Hicks L, Dresselhaus M. Thermoelectric figure of merit of a one-dimensional conductor. *Phys Rev B* 1993;47:16631–4.
- [18] Dresselhaus MS, Koga T, Sun X, Cronin SB, Wang K, Chen G. Low dimensional thermoelectrics. XVI ICT “97 Proc ICT”97 16th Int Conf Thermoelectr (Cat No97TH8291) 1997.
- [19] M. S. Dresselhaus, G. Dresselhaus,. THE PROMISE OF LOW-DIMENSIONAL THERMOELECTRIC MATERIALS. *Microscale Thermophys Eng* 1999;3:89–100.
- [20] Zhao L-D, Lo S-H, Zhang Y, Sun H, Tan G, Uher C, et al. Ultralow thermal conductivity and high thermoelectric figure of merit in SnSe crystals. *Nature* 2014;508:373–7.
- [21] Jeng M-S, Yang R, Song D, Chen G. Modeling the thermal conductivity and phonon transport in nanoparticle composites using Monte Carlo simulation. *J Heat Transf Asme* 2008;130:42410.
- [22] Poudel B, Hao Q, Ma Y, Lan Y, Minnich A, Yu B, et al. High-thermoelectric performance of nanostructured bismuth antimony telluride bulk alloys. *Science* 2008;320:634–8.
- [23] Wang XW, Lee H, Lan YC, Zhu GH, Joshi G, Wang DZ, et al. Enhanced thermoelectric figure of merit in nanostructured n-type silicon germanium bulk alloy. *Appl Phys Lett* 2008;93:193121.
- [24] Joshi G, Lee H, Lan Y, Wang X, Zhu G, Wang D, et al. Enhanced thermoelectric figure-of-merit in nanostructured p-type silicon germanium bulk alloys. *Nano Lett* 2008;8:4670–4.
- [25] Poudeu PFP, D’Angelo J, Downey AD, Short JL, Hogan TP, Kanatzidis MG. High thermoelectric figure of merit and nanostructuring in bulk p-type $\text{Na}_{1-x}\text{Pb}_x\text{Sb}_{1-y}\text{Te}_{1+y}$. *Angew Chem Int Ed Engl* 2006;45:3835–9.
- [26] Bubnova O, Khan ZU, Malti A, Braun S, Fahlman M, Berggren M, et al. Optimization of the thermoelectric figure of merit in the conducting polymer poly(3,4-ethylenedioxythiophene). *Nat Mater* 2011;10:429–33.
- [27] Koumoto K, Wang Y, Zhang R, Kosuga A, Funahashi R. Oxide Thermoelectric Materials: A Nanostructuring Approach. *Annu Rev Mater Res* 2010;40:363–94.
- [28] Wang Y, Sui Y, Li F, Xu L, Wang X, Su W, et al. Thermoelectrics in misfit-layered oxides $[(\text{Ca},\text{Ln})_2\text{CoO}_3]_{0.62}[\text{CoO}_2]$: From bulk to nano. *Nano Energy* 2012;1:456–65.

- [29] Liu Y, Zhao L, Liu Y, Lan J, Xu W, Li F, et al. Remarkable Enhancement in Thermoelectric Performance of BiCuSeO 2011;20112–5.
- [30] Lan J-L, Liu Y-C, Zhan B, Lin Y-H, Zhang B, Yuan X, et al. Enhanced thermoelectric properties of Pb-doped BiCuSeO ceramics. *Adv Mater* 2013;25:5086–90.
- [31] Ohta S, Nomura T, Ohta H, Koumoto K. High-temperature carrier transport and thermoelectric properties of heavily La- or Nb-doped SrTiO₃ single crystals. *J Appl Phys* 2005;97:034106.
- [32] Flahaut D, Mihara T, Funahashi R, Nabeshima N, Lee K, Ohta H, et al. Thermoelectrical properties of A-site substituted Ca_{1-x}Re_xMnO₃ system. *J Appl Phys* 2006;100:084911.
- [33] Kikuchi a., Okinaka N, Akiyama T. A large thermoelectric figure of merit of La-doped SrTiO₃ prepared by combustion synthesis with post-spark plasma sintering. *Scr Mater* 2010;63:407–10.
- [34] Bocher L, Aguirre MH, Logvinovich D, Shkabko A, Robert R, Trottmann M, et al. CaMn(1-x)Nb(x)O₃ (x < or = 0.08) perovskite-type phases as promising new high-temperature n-type thermoelectric materials. *Inorg Chem* 2008;47:8077–85.
- [35] Tsubota T, Ohtaki M, Eguchi K, Arai H. Thermoelectric properties of Al-doped ZnO as a promising oxide material for high-temperature thermoelectric conversion. *J Mater Chem* 1997;7:85–90.
- [36] Ito M, Nagira T, Furumoto D, Katsuyama S. Synthesis of Na_xCo₂O₄ thermoelectric oxides by the polymerized complex method 2003;48:403–8.
- [37] Könenkamp R, Word RC, Godinez M. Ultraviolet electroluminescence from ZnO/polymer heterojunction light-emitting diodes. *Nano Lett* 2005;5:2005–8.
- [38] Jeong M-C, Oh B-Y, Ham M-H, Myoung J-M. Electroluminescence from ZnO nanowires in n-ZnO film/ZnO nanowire array/p-GaN film heterojunction light-emitting diodes. *Appl Phys Lett* 2006;88:202105.
- [39] Lim J-H, Kang C-K, Kim K-K, Park I-K, Hwang D-K, Park S-J. UV Electroluminescence Emission from ZnO Light-Emitting Diodes Grown by High-Temperature Radiofrequency Sputtering. *Adv Mater* 2006;18:2720–4.
- [40] Zimmler M a, Voss T, Ronning C, Capasso F. Exciton-related electroluminescence from ZnO nanowire light-emitting diodes. *Appl Phys Lett* 2009;94:241120.
- [41] Bader SD, Parkin SSP. Spintronics. *Annu Rev Condens Matter Phys* 2010;1:71–88.

- [42] Carcia PF, McLean RS, Reilly MH, Nunes G. Transparent ZnO thin-film transistor fabricated by rf magnetron sputtering. *Appl Phys Lett* 2003;82:1117.
- [43] Fortunato EMC, Barquinha PMC, Pimentel ACMBG, Goncalves AMF, Marques AJS, Pereira LMN, et al. Fully transparent ZnO thin-film transistor produced at room temperature. *Adv Mater (Weinheim, Ger)* 2005;17:590–4.
- [44] Park S-M, Ikegami T, Ebihara K, Shin P-K. Structure and properties of transparent conductive doped ZnO films by pulsed laser deposition. *Appl Surf Sci* 2006;253:1522–7.
- [45] Sahu DR, Lin SY, Huang JL. Deposition of Ag-based Al-doped ZnO multilayer coatings for the transparent conductive electrodes by electron beam evaporation. *Sol Energy Mater Sol Cells* 2007;91:851–5.
- [46] Sahu DR, Huang JL. Development of ZnO-based transparent conductive coatings. *Sol Energy Mater Sol Cells* 2009;93:1923–7.
- [47] Agura H, Suzuki A, Matsushita T, Aoki T, Okuda M. Low resistivity transparent conducting Al-doped ZnO films prepared by pulsed laser deposition. *Thin Solid Films*, vol. 445, 2003, p. 263–7.
- [48] Lin W, Chen D, Zhang J, Lin Z, Huang J, Li W, et al. Hydrothermal Growth of ZnO Single Crystals with High Carrier Mobility. *Cryst Growth Des* 2009;9:4378–83.
- [49] Kim WM, Kim IH, Ko JH, Cheong B, Lee TS, Lee KS, et al. Density-of-state effective mass and non-parabolicity parameter of impurity doped ZnO thin films. *J Phys D Appl Phys* 2008;41:195409.
- [50] Ohtaki M, Tsubota T, Eguchi K, Arai H. High-temperature thermoelectric properties of $(\text{Zn}_{1-x}\text{Al}_x)\text{O}$. *J Appl Phys* 1996;79:1816.
- [51] Ohtaki M, Araki K, Yamamoto K. High Thermoelectric Performance of Dually Doped ZnO Ceramics. *J Electron Mater* 2009;38:1234–8.
- [52] Søndergaard M, Bøjesen ED, Borup KA, Christensen S, Christensen M, Iversen BB. Sintering and annealing effects on ZnO microstructure and thermoelectric properties – Supporting information n.d.
- [53] Nam WH, Lim YS, Choi S-M, Seo W-S, Lee JY. High-temperature charge transport and thermoelectric properties of a degenerately Al-doped ZnO nanocomposite. *J Mater Chem* 2012;22:14633.
- [54] Jood P, Mehta RJ, Zhang Y, Peleckis G, Wang X, Siegel RW, et al. Al-doped zinc oxide nanocomposites with enhanced thermoelectric properties. *Nano Lett* 2011;11:4337–42.

- [55] Vogel-Schäuble N, Dujardin R, Weidenkaff A, Aguirre MH. Influence of Thermal Aging Phenomena on Thermoelectric Properties of Al-Substituted ZnO. *J Electron Mater* 2011;41:1606–14.
- [56] Han L, Nong N Van, Hung LT, Holgate T, Pryds N, Ohtaki M, et al. The influence of α - and γ -Al₂O₃ phases on the thermoelectric properties of Al-doped ZnO. *J Alloys Compd* 2013;555:291–6.
- [57] Kinemuchi Y, Nakano H, Mikami M, Kobayashi K, Watari K, Hotta Y. Enhanced boundary-scattering of electrons and phonons in nanograined zinc oxide. *J Appl Phys* 2010;108:053721.
- [58] Bérardan D, Byl C, Dragoë N. Influence of the Preparation Conditions on the Thermoelectric Properties of Al-Doped ZnO. *J Am Ceram Soc* 2010;93:2352–8.
- [59] Vogel-Schäuble N, Romanyuk YE, Yoon S, Saji KJ, Populoh S, Pokrant S, et al. Thermoelectric properties of nanostructured Al-substituted ZnO thin films. *Thin Solid Films* 2012;520:6869–75.
- [60] Janotti A, Van de Walle CG. Fundamentals of zinc oxide as a semiconductor. *Reports Prog Phys* 2009;72:126501.
- [61] Janotti A, Van de Walle CG. Native point defects in ZnO. *Phys Rev B* 2007;76:165202.
- [62] Shen Z, Johnsson M, Zhao Z, Nygren M. Spark Plasma Sintering of Alumina. *J Am Ceram Soc* 2002;85:1921–7.
- [63] Kim KH, Shim SH, Shim KB, Niihara K, Hojo J. Microstructural and Thermoelectric Characteristics of Zinc Oxide-Based Thermoelectric Materials Fabricated Using a Spark Plasma Sintering Process. *J Am Ceram Soc* 2005;88:628–32.
- [64] Ma N, Li J-F, Zhang BP, Lin YH, Ren LR, Chen GF. Microstructure and thermoelectric properties of Zn_{1-x}Al_xO ceramics fabricated by spark plasma sintering. *J Phys Chem Solids* 2010;71:1344–9.
- [65] Bérardan D, Byl C, Dragoë N. Influence of the Preparation Conditions on the Thermoelectric Properties of Al-Doped ZnO. *J Am Ceram Soc* 2010;93:2352–8.
- [66] Jacob KT. Gibbs Free Energies of Formation of Zinc Aluminate (ZnAl₂O₄) and Zinc Chromite (ZnCr₂O₄). *Thermochim Acta* 1976;15:79–87.
- [67] Ohio T, Introduction I. Kinetics and Mechanism of the Reaction Between Zinc Oxide and Aluminum Oxide 1965.
- [68] Tsuchida BT, Furuichi R, Ishii T. Reactivity of η -, γ -, and α -Al₂O₃ for ZnAl₂O₄ formation 1976;184:175–84.

- [69] Serier H, Gaudon M, Ménétrier M. Al-doped ZnO powdered materials: Al solubility limit and IR absorption properties. *Solid State Sci* 2009;11:1192–7.
- [70] Shannon RD. Revised Effective Ionic Radii and Systematic Studies of Interatomic Distances in Halides and Chalcogenides. *Acta Cryst* 1976:751.
- [71] Moelans N, Blanpain B, Wollants P. Pinning effect of second-phase particles on grain growth in polycrystalline films studied by 3-D phase field simulations 2007;55:2173–82.
- [72] Cai KF, Müller E, Drašar C, Mroczek a. Preparation and thermoelectric properties of Al-doped ZnO ceramics. *Mater Sci Eng B* 2003;104:45–8.
- [73] Jiménez-González a. Optical and electrical characteristics of aluminum-doped ZnO thin films prepared by solgel technique. *J Cryst Growth* 1998;192:430–8.
- [74] Su M, Elsbernd CE, Mason T. Jonker “Pear” Analysis of Oxide Superconductors. *J Am Ceram Soc* 1990;73:415–9.
- [75] Tanaka Y, Ifuku T, Tsuchida K, Kato A. Thermoelectric properties of ZnO-based materials. *J Mater Sci Lett* 1997;16:155–7.
- [76] BRANSON DL. Kinetics and Mechanism of the Reaction Between Zinc Oxide and Aluminum Oxide. *J Am Ceram Soc* 1965;48:591–5.
- [77] Kinemuchi Y, Nakano H, Kaga H, Tanaka S, Uematsu K, Watari K. Microstructural Evidence of Hall Mobility Anisotropy in c-Axis Textured Al-Doped ZnO. *J Am Ceram Soc* 2011;94:2339–43.
- [78] Han L, Hung L, Nong N Van. The Influence of Spark Plasma Sintering Temperature on the Microstructure and Thermoelectric Properties of Al, Ga Dual-Doped ZnO. *J Electron ...* 2013.
- [79] Bell LE. Cooling, heating, generating power, and recovering waste heat with thermoelectric systems. *Science* 2008;321:1457–61.
- [80] Ma N, Li J, Zhang BP, Lin YH, Ren LR, Chen GF. Journal of Physics and Chemistry of Solids Microstructure and thermoelectric properties of Zn_{1-x}Al_xO ceramics fabricated by spark plasma sintering 2010;71:1344–9.
- [81] Song X, Liu X, Zhang J. Neck Formation and Self-Adjusting Mechanism of Neck Growth of Conducting Powders in Spark Plasma Sintering. *J Am Ceram Soc* 2006;89:494–500.
- [82] Liu X, Song X, Zhang J, Zhao S. Temperature distribution and neck formation of WC–Co combined particles during spark plasma sintering. *Mater Sci Eng A* 2008;488:1–7.
- [83] Goldsmid HJ. Thermoelectric Refrigeration. vol. 1. 1964.

- [84] Tritt TM. THERMOELECTRIC MATERIALS:Holey and Unholey Semiconductors. *Science* (80-) 1999;283:804–5.
- [85] Xie WJ, He J, Zhu S, Su XL, Wang SY, Holgate T, et al. Simultaneously optimizing the independent thermoelectric properties in (Ti,Zr,Hf)(Co,Ni)Sb alloy by in situ forming InSb nanoinclusions. *Acta Mater* 2010;58:4705–13.
- [86] Yan X, Joshi G, Liu W, Lan Y, Wang H, Lee S, et al. Enhanced thermoelectric figure of merit of p-type half-Heuslers. *Nano Lett* 2011;11:556–60.
- [87] Rogl G, Grytsiv A, Rogl P, Bauer E, Kerber MB, Zehetbauer M, et al. Multifilled nanocrystalline p-type didymium – Skutterudites with $ZT > 1.2$. *Intermetallics* 2010;18:2435–44.
- [88] Shi X, Yang J, Salvador JR, Chi M, Cho JY, Wang H, et al. Multiple-filled skutterudites: high thermoelectric figure of merit through separately optimizing electrical and thermal transports. *J Am Chem Soc* 2011;133:7837–46.
- [89] Ohtaki M, Araki K, Yamamoto K. High Thermoelectric Performance of Dually Doped ZnO Ceramics. *J Electron Mater* 2009;38:1234–8.
- [90] Pan ZW, Dai ZR, Wang ZL. Nanobelts of semiconducting oxides. *Science* 2001;291:1947–9.
- [91] Kong XY, Wang ZL. Spontaneous Polarization-Induced Nanohelices, Nanosprings, and Nanorings of Piezoelectric Nanobelts. *Nano Lett* 2003;3:1625–31.
- [92] Kong XY, Ding Y, Yang R, Wang ZL. Single-crystal nanorings formed by epitaxial self-coiling of polar nanobelts. *Science* 2004;303:1348–51.
- [93] Hughes WL, Wang ZL. Formation of piezoelectric single-crystal nanorings and nanobows. *J Am Chem Soc* 2004;126:6703–9.
- [94] Gao PX, Ding Y, Mai W, Hughes WL, Lao C, Wang ZL. Conversion of zinc oxide nanobelts into superlattice-structured nanohelices. *Science* 2005;309:1700–4.
- [95] Ohtaki M, Tsubota T, Eguchi K, Arai H. High-temperature thermoelectric properties of $(\text{Zn}_{1-x}\text{Al}_x)\text{O}$. *J Appl Phys* 1996;79:1816.
- [96] Baxter JB, Wu F, Aydil ES. Growth mechanism and characterization of zinc oxide hexagonal columns. *Appl Phys Lett* 2003;83:3797–9.
- [97] Jang ES, Won J-H, Hwang S-J, Choy J-H. Fine Tuning of the Face Orientation of ZnO Crystals to Optimize Their Photocatalytic Activity. *Adv Mater* 2006;18:3309–12.

- [98] Ohtaki M, Miyaishi S. Extremely Low Thermal Conductivity in Oxides with Cage-Like Crystal Structure. *J Electron Mater* 2013;42:1299–302.
- [99] Meulenkamp EA. Synthesis and Growth of ZnO Nanoparticles 1998;5647:5566–72.
- [100] Lu CJ, Qiao Y, Qi YJ, Chen XQ, Zhu JS. Large anisotropy of ferroelectric and dielectric properties for Bi_{3.15}Nd_{0.85}Ti₃O₁₂ thin films deposited on Pt/Ti/SiO₂/Si. *Appl Phys Lett* 2005;87:222901.
- [101] Liu W, Yan X, Chen G, Ren Z. Recent advances in thermoelectric nanocomposites. *Nano Energy* 2012;1:42–56.
- [102] Zhao LD, Zhang BP, Li JF, Zhang HL, Liu WS. Enhanced thermoelectric and mechanical properties in textured n-type Bi₂Te₃ prepared by spark plasma sintering. *Solid State Sci* 2008;10:651–8.
- [103] Yan X, Poudel B, Ma Y, Liu WS, Joshi G, Wang H, et al. Experimental studies on anisotropic thermoelectric properties and structures of n-type Bi₂Te_{2.7}Se_{0.3}. *Nano Lett* 2010;10:3373–8.
- [104] Ong KP, Singh DJ, Wu P. Analysis of the thermoelectric properties of n-type ZnO. *Phys Rev B* 2011;83.
- [105] Callaway J. Model for Lattice Thermal Conductivity at Low Temperatures. *Phys Rev* 1959;113:1046–51.
- [106] Cahill D, Watson S, Pohl R. Lower limit to the thermal conductivity of disordered crystals. *Phys Rev B* 1992;46:6131–40.
- [107] Majumdar A. Microscale Heat Conduction in Dielectric Thin Films. *J Heat Transfer* 1993;115:7.
- [108] Kim W, Majumdar A. Phonon scattering cross section of polydispersed spherical nanoparticles. *J Appl Phys* 2006;99:084306.
- [109] Wang N, Li H, Ba Y, Wang Y, Wan C, Fujinami K, et al. Effects of YSZ Additions on Thermoelectric Properties of Nb-Doped Strontium Titanate. *J Electron Mater* 2010;39:1777–81.
- [110] Ohta H, Kim S, Mune Y, Mizoguchi T, Nomura K, Ohta S, et al. Giant thermoelectric Seebeck coefficient of a two-dimensional electron gas in SrTiO₃. *Nat Mater* 2007;6:129–34.
- [111] Choi S-M, Lim C-H, Seo W-S. Thermoelectric Properties of the Ca_{1-x}R_xMnO₃ Perovskite System (R: Pr, Nd, Sm) for High-Temperature Applications. *J Electron Mater* 2010;40:551–6.

- [112] Minami T, Miyata T, Yamamoto T. Stability of transparent conducting oxide films for use at high temperatures. *J Vac Sci Technol A Vacuum, Surfaces, Film* 1999;17:1822.
- [113] Wang Y, Sui Y, Fan H, Wang X, Su Y, Su W, et al. High temperature thermoelectric response of electron-doped CaMnO. *Chem Mater* 2009;21:4653–60.
- [114] Koumoto K, Funahashi R, Guilmeau E, Miyazaki Y, Weidenkaff A, Wang Y, et al. Thermoelectric ceramics for energy harvesting. *J Am Ceram Soc* 2013;96:1–23.
- [115] Yang Y, Jin S, Medvedeva JE, Ireland JR, Metz AW, Ni J, et al. CdO as the archetypical transparent conducting oxide. Systematics of dopant ionic radius and electronic structure effects on charge transport and band structure. *J Am Chem Soc* 2005;127:8796–804.
- [116] Venkatachalapathy V, Galeckas A, Trunk M, Zhang T, Azarov A, Kuznetsov AY. Understanding phase separation in ZnCdO by a combination of structural and optical analysis. *Phys Rev B* 2011;83:125315.
- [117] Misho RH. Three-Phonon Scattering Relaxation Rate and Phonon Conductivity Application to MgsGe 1977;69:69–81.